

Effect of strain path and texture on microstructure in Fe–22 wt.% Mn–0.6 wt.% C TWIP steel

D. Raabe, I. Gutierrez-Urrutia



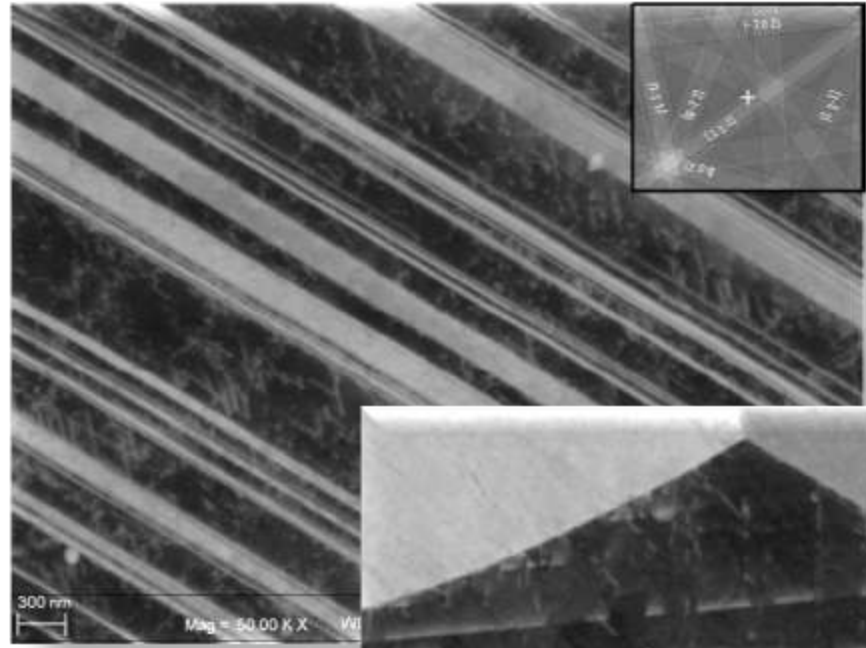
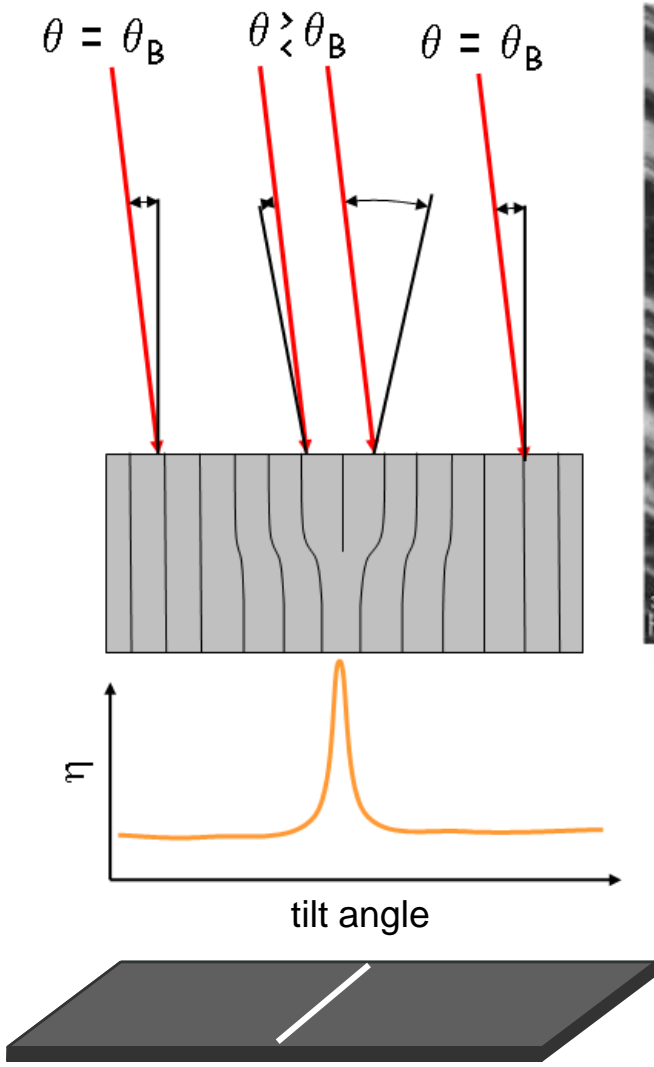
Max-Planck-Institut
für Eisenforschung GmbH
Düsseldorf, Germany

WWW.MPIE.DE
d.raabe@mpie.de

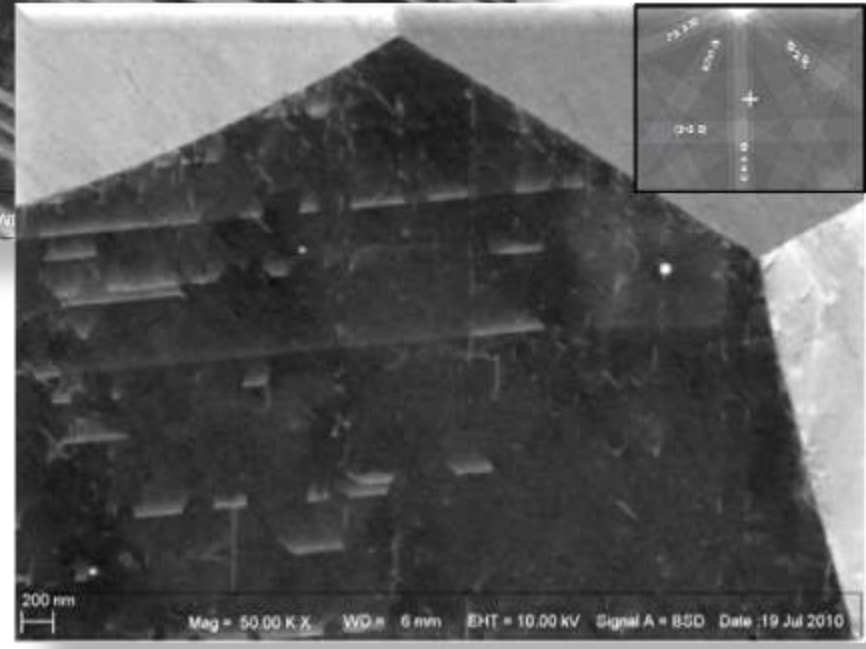


- **Electron channeling contrast imaging**
- **Twinning and texture**
- **Strain path effects**
- **Bauschinger effects**
- **Conclusions**

EBSD: Work hardening of TWIP steels, Fe-22Mn-0.6C (wt%)



ECCI



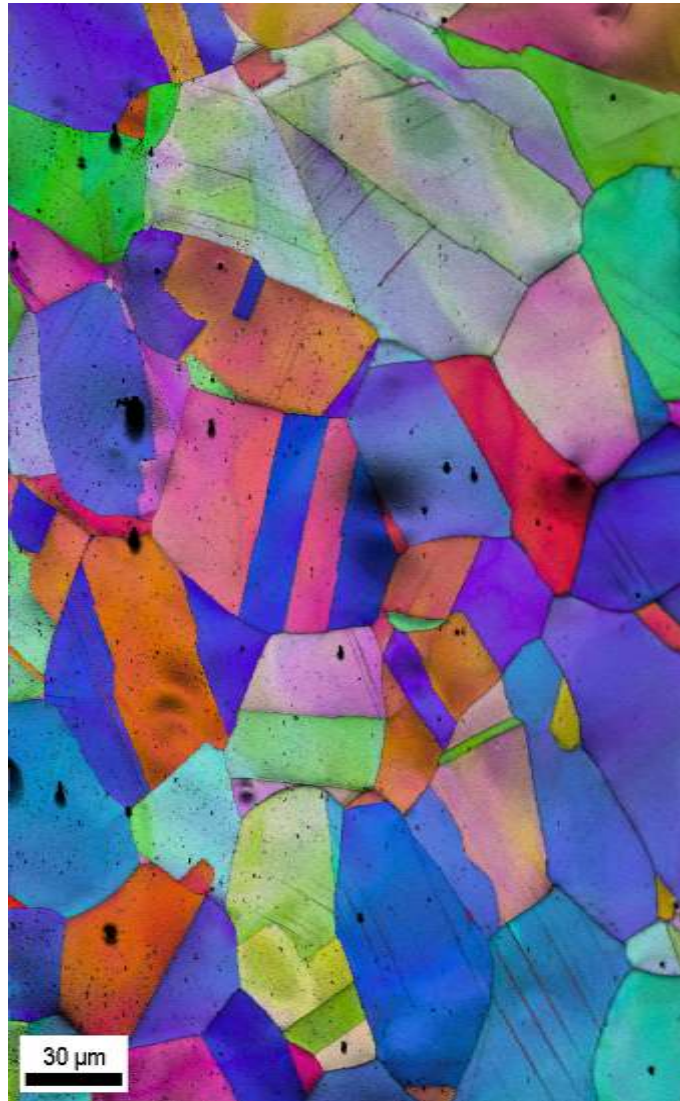
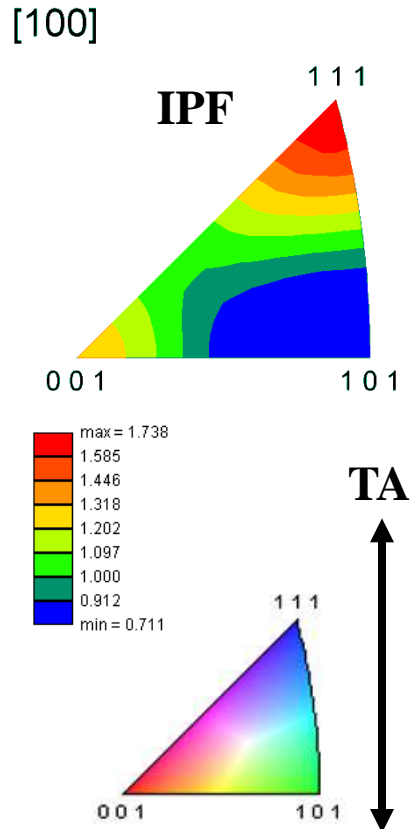
I. Gutierrez-Urrutia, S. Zaefferer, D. Raabe; Scripta Materialia 61 (2009), 737
 I. Gutierrez-Urrutia, S. Zaefferer, D. Raabe; Materials Science and Engineering A 527 (2010), 3552
 I. Gutierrez-Urrutia, D. Raabe Acta Materialia 59 (2011) 6449–6462



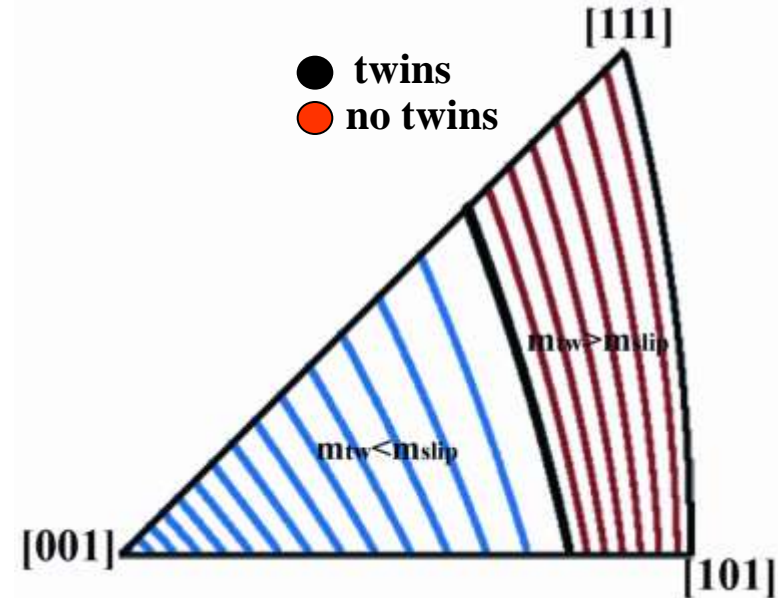
- **Electron channeling contrast imaging**
- **Twinning and texture**
- **Strain path effects**
- **Bauschinger effects**
- **Conclusions**

Influence of grain orientation on deformation twinning

Tensile test
 σ : 380 MPa
 ϵ : 0.1



Grain orientations



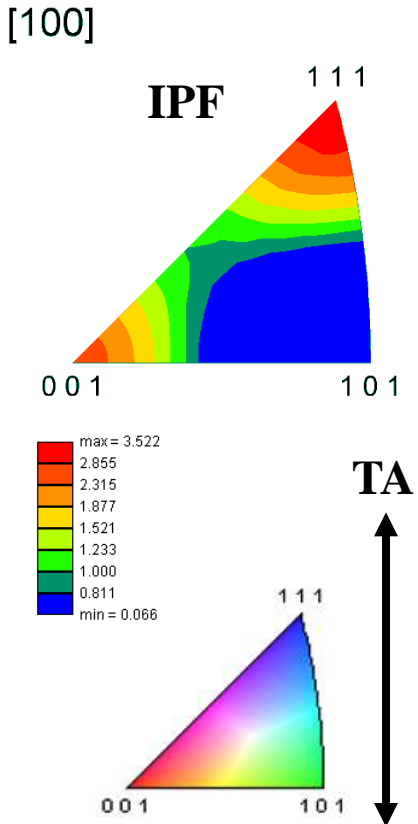
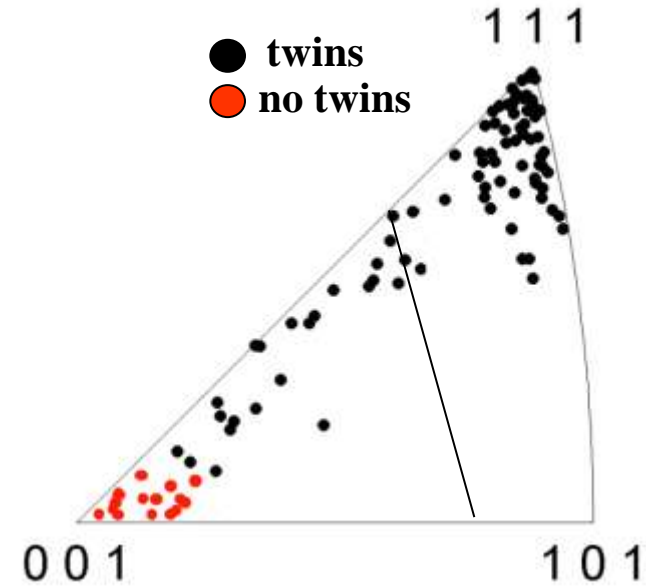
I. Gutierrez-Urrutia, S. Zaefferer, D. Raabe; Scripta Materialia 61 (2009), 737

I. Gutierrez-Urrutia, S. Zaefferer, D. Raabe; Materials Science and Engineering A 527 (2010), 3552

Tensile test
 σ : 950 MPa
 ϵ : 0.4



Grain orientations



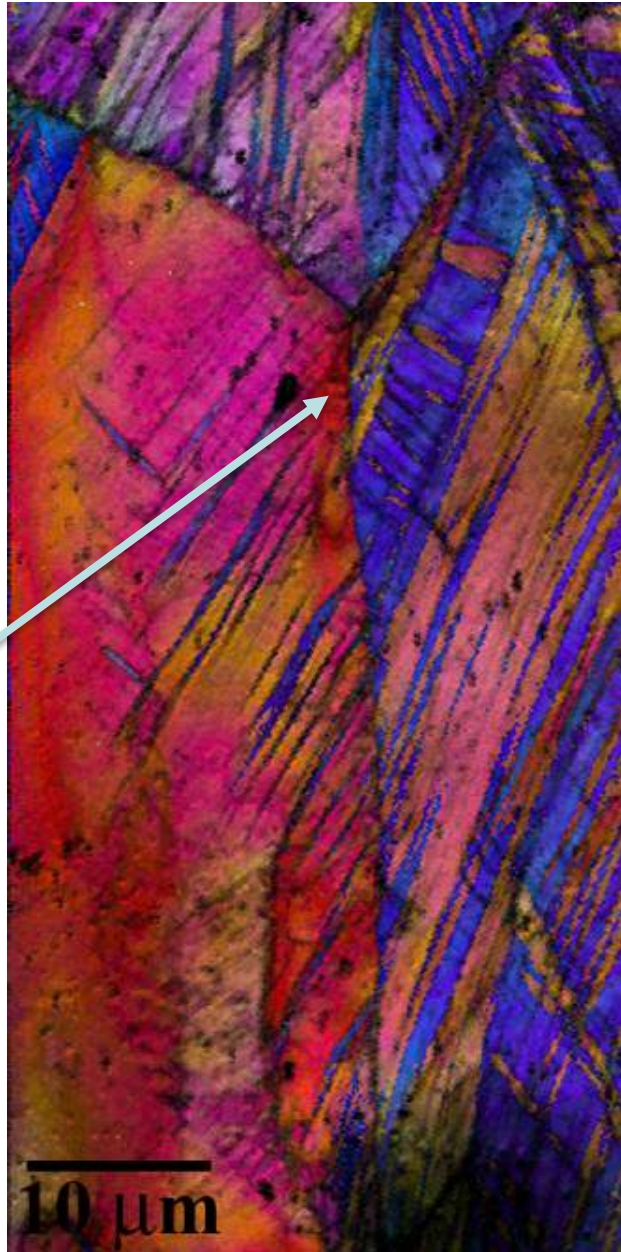
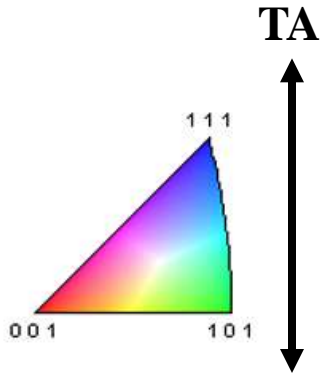
Influence of grain orientation on deformation twinning

Tensile test
 σ : 950 MPa
 ϵ : 0.4

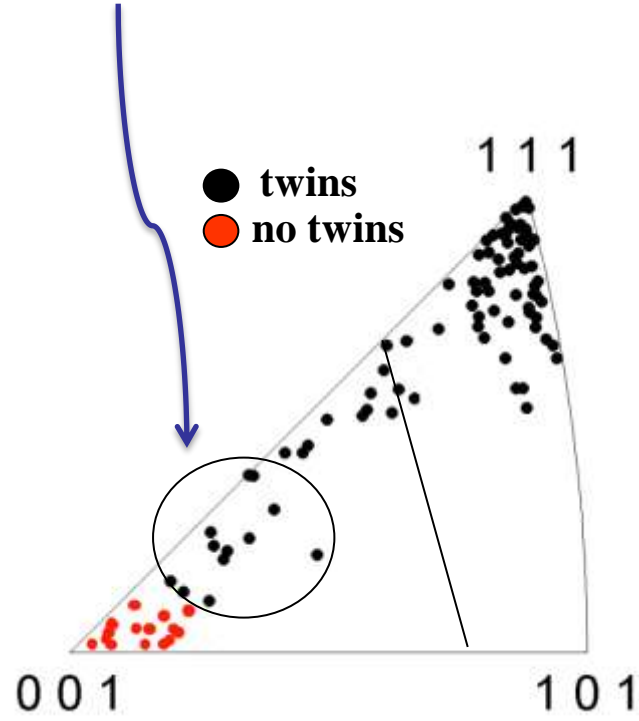
Local stress concentrations at GB

Micromechanical B.C. matter

twin transfer

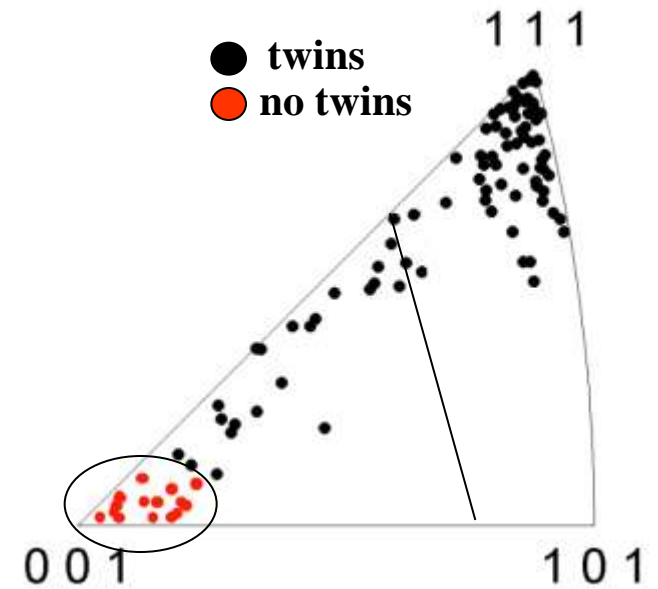
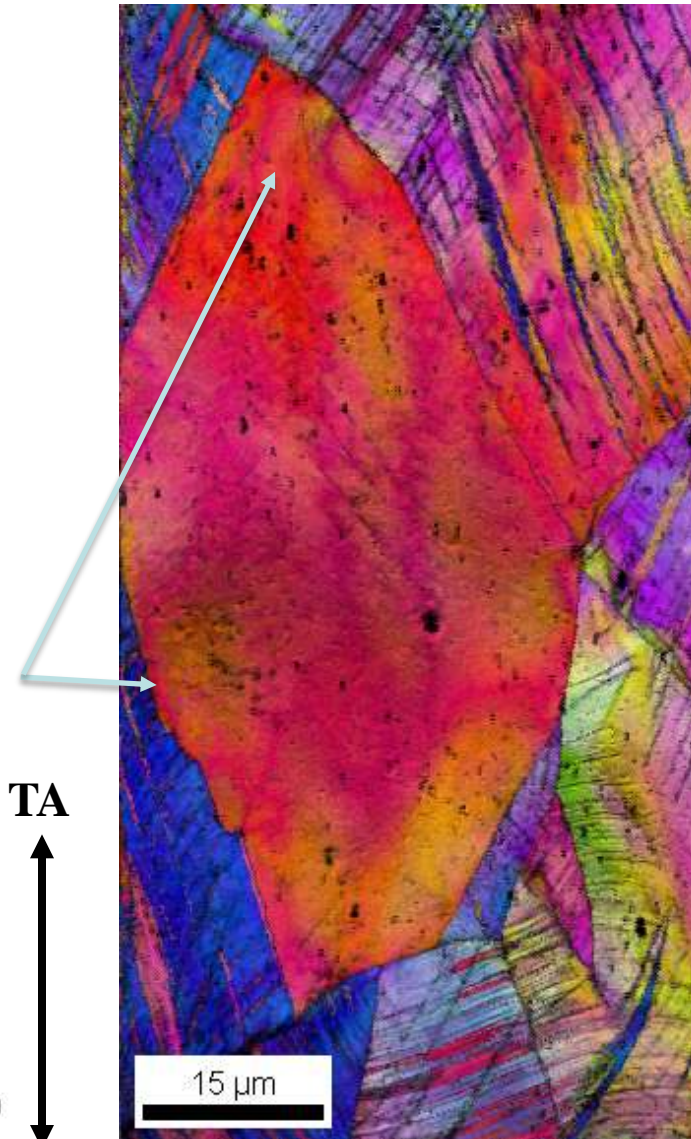
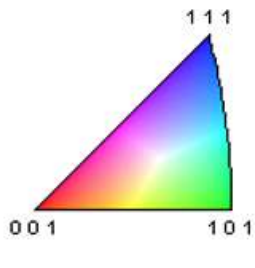


Why twinning in these orientations?



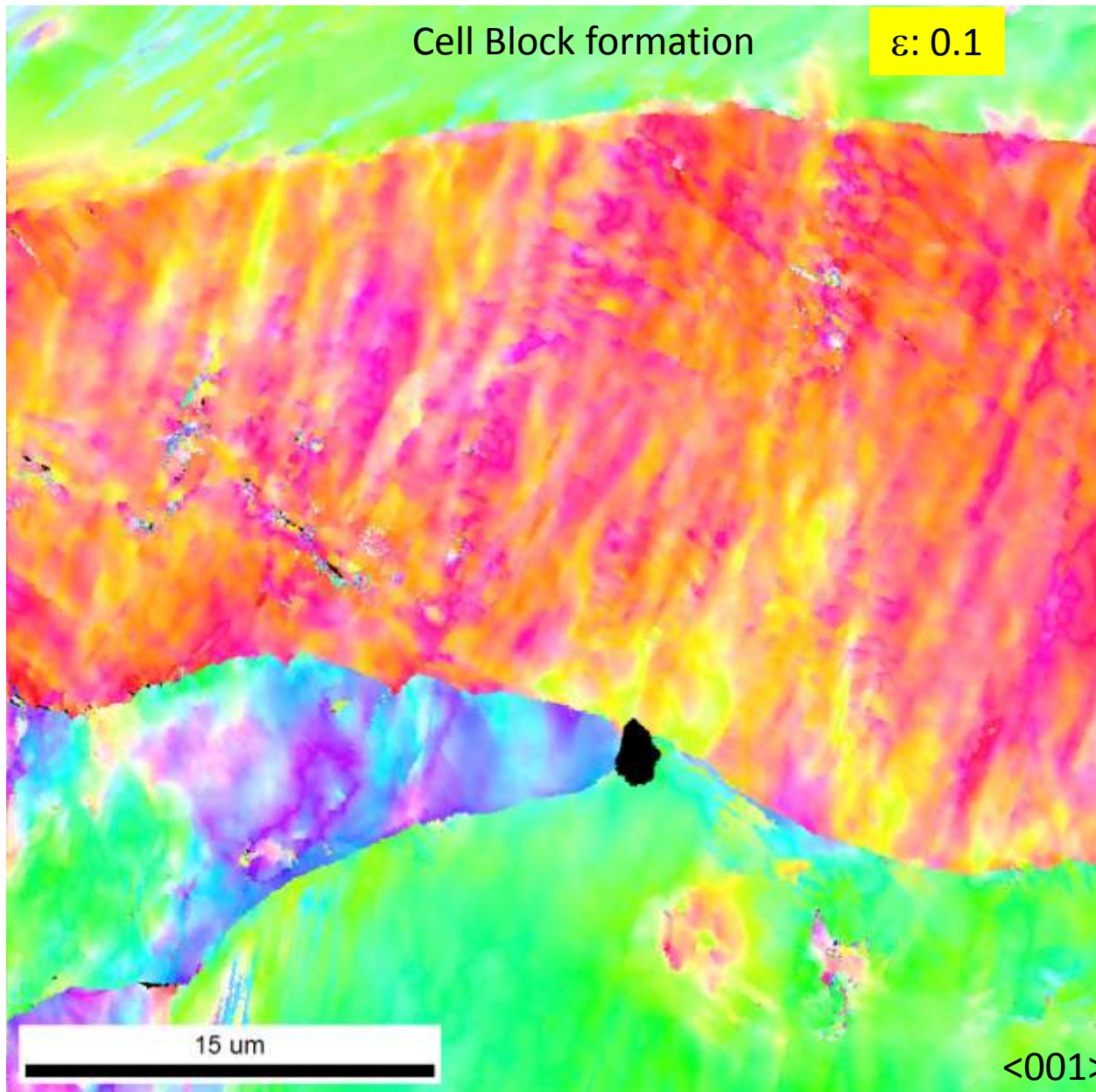
Tensile test
 σ : 950 MPa
 ϵ : 0.4

no twin transfer

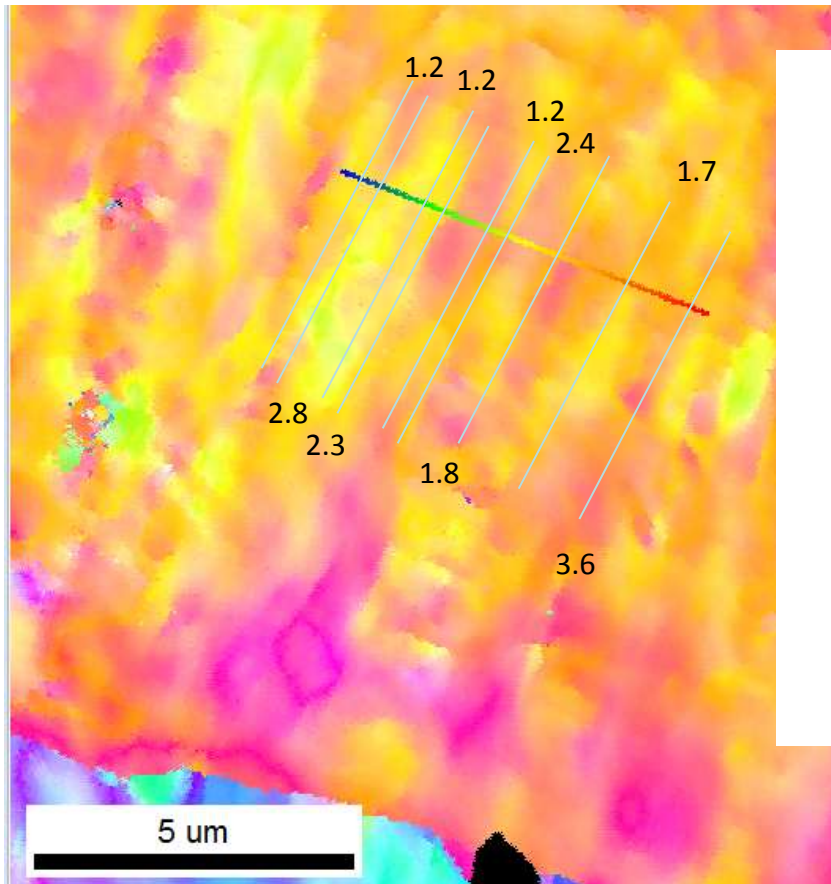
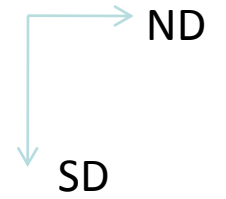




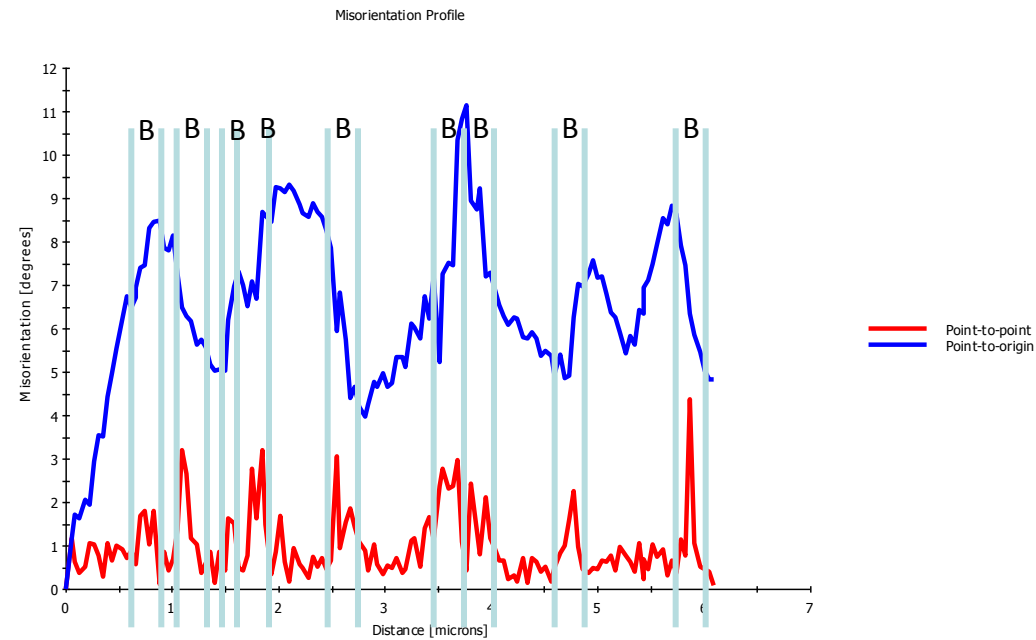
- **Electron channeling contrast imaging**
- **Twinning and texture**
- **Strain path effects**
- **Bauschinger effects**
- **Conclusions**



$\epsilon: 0.1$



Misorientation profile



EBSD does not detect
dislocation cells

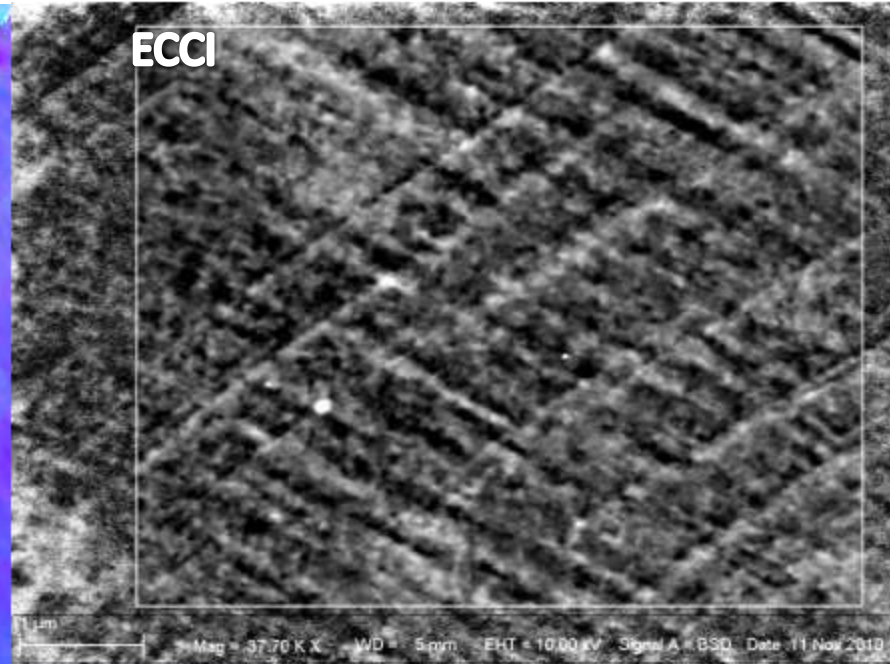
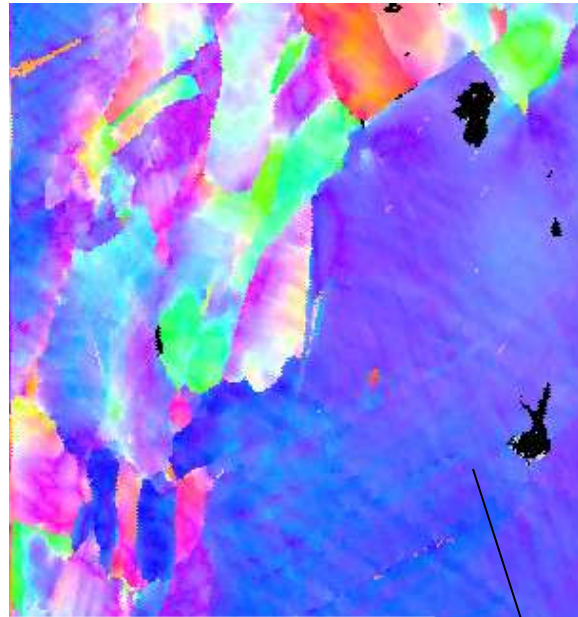
Shear : $\epsilon:0.3$

100 μm

ND
SD

D. R. Steinmetz, T. Jäpel, B. Wietbrock, P. Eisenlohr, I. Gutierrez-Urrutia, A. Saeed-Akbari, T. Hickel, F. Roters, D. Raabe: Acta Materialia 61 (2013) 494-510
Revealing the strain-hardening behavior of twinning-induced plasticity steels: Theory, simulations, experiments

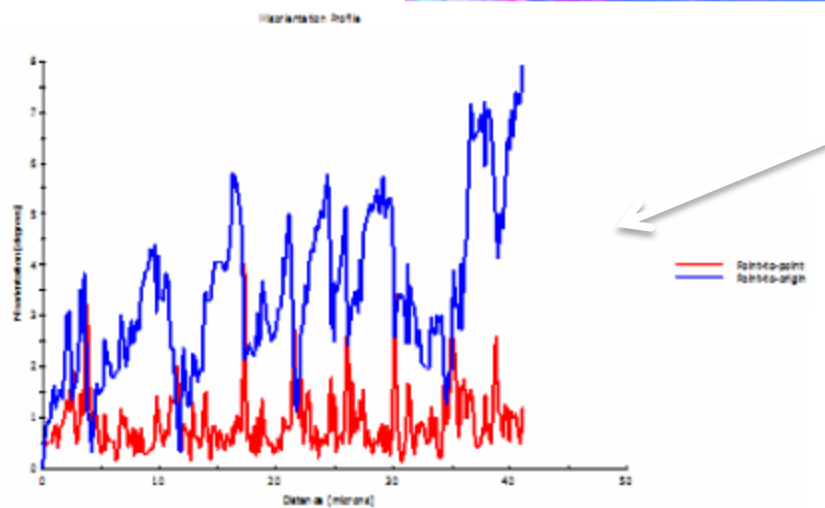
Shear : $\epsilon:0.3$



{111} traces of shear

Substructures with misorientation up to 2deg, hence, visible via EBSD

$\langle 111 \rangle //$ Shear direction



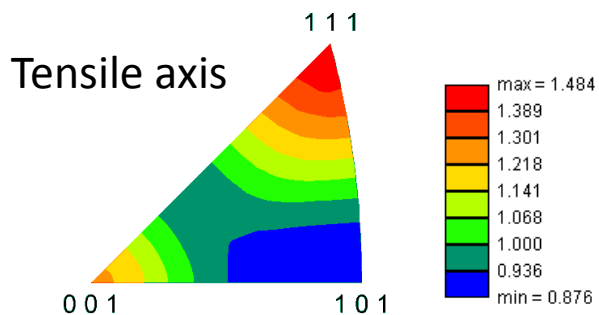
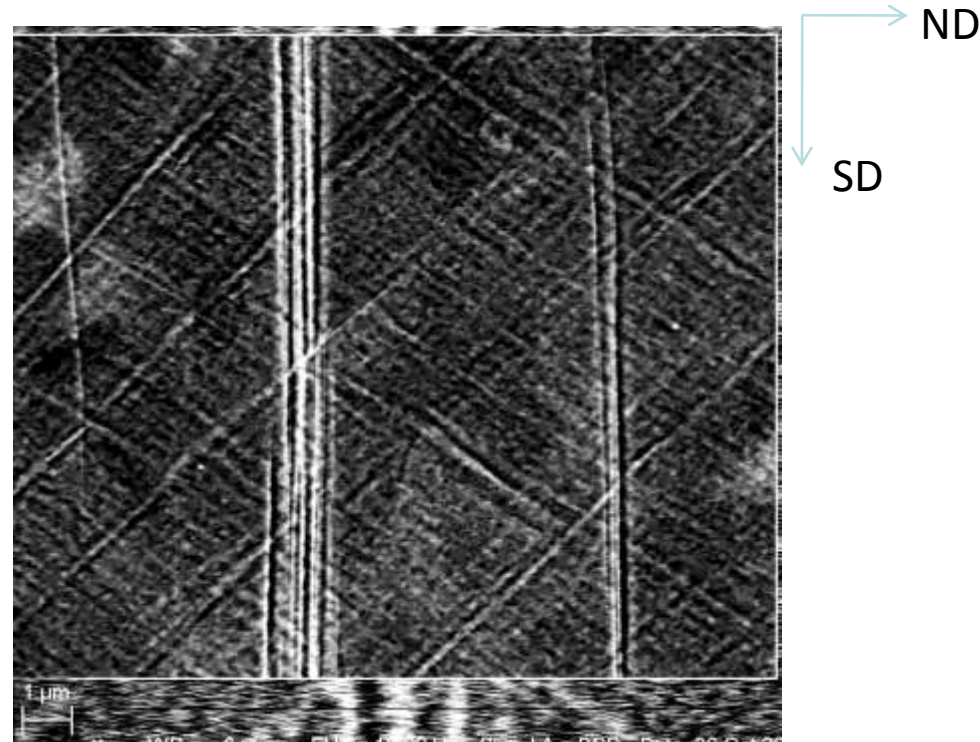
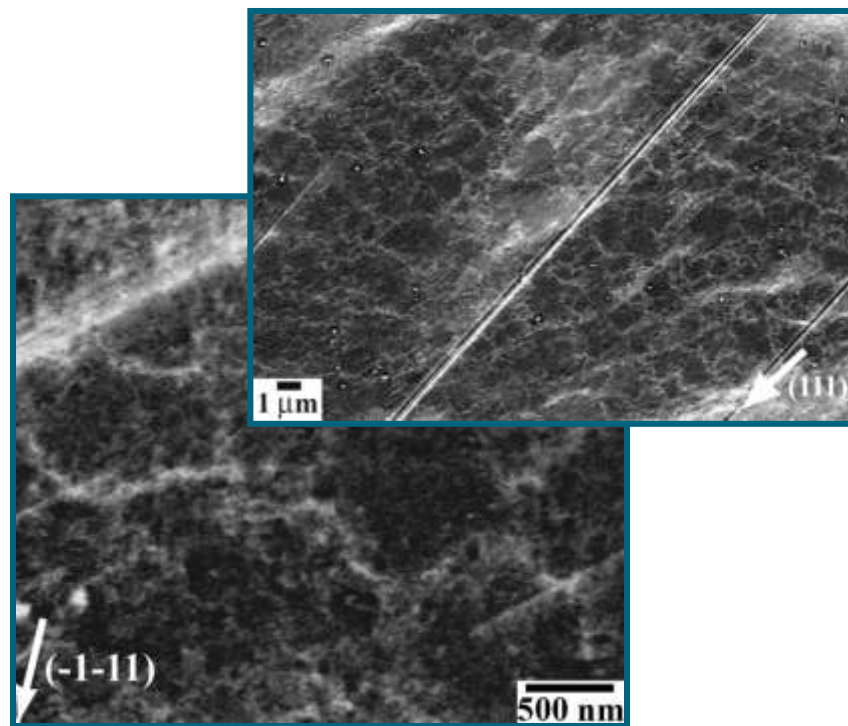
Misorientation profile

100 μm

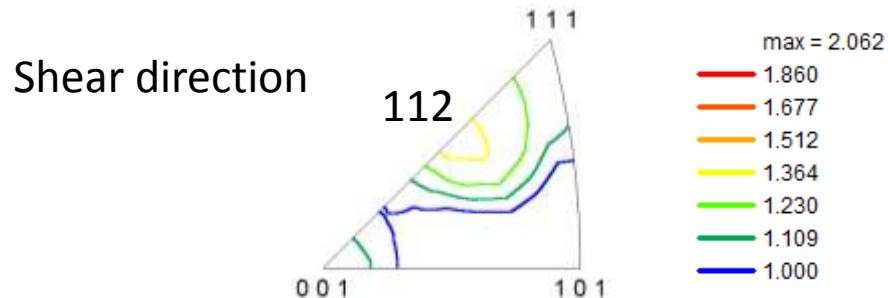


Tensile: dislocation cells

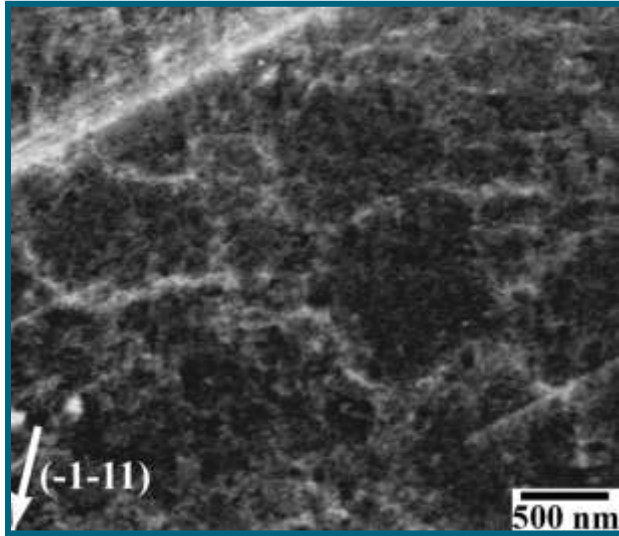
Shear: symmetric patterning, cell blocks, shear bands



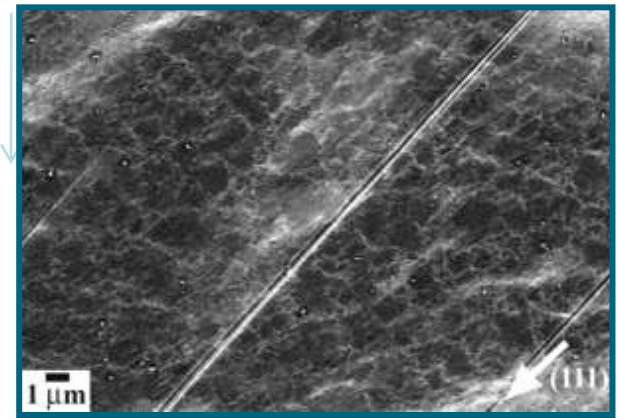
$\epsilon: 0.3$



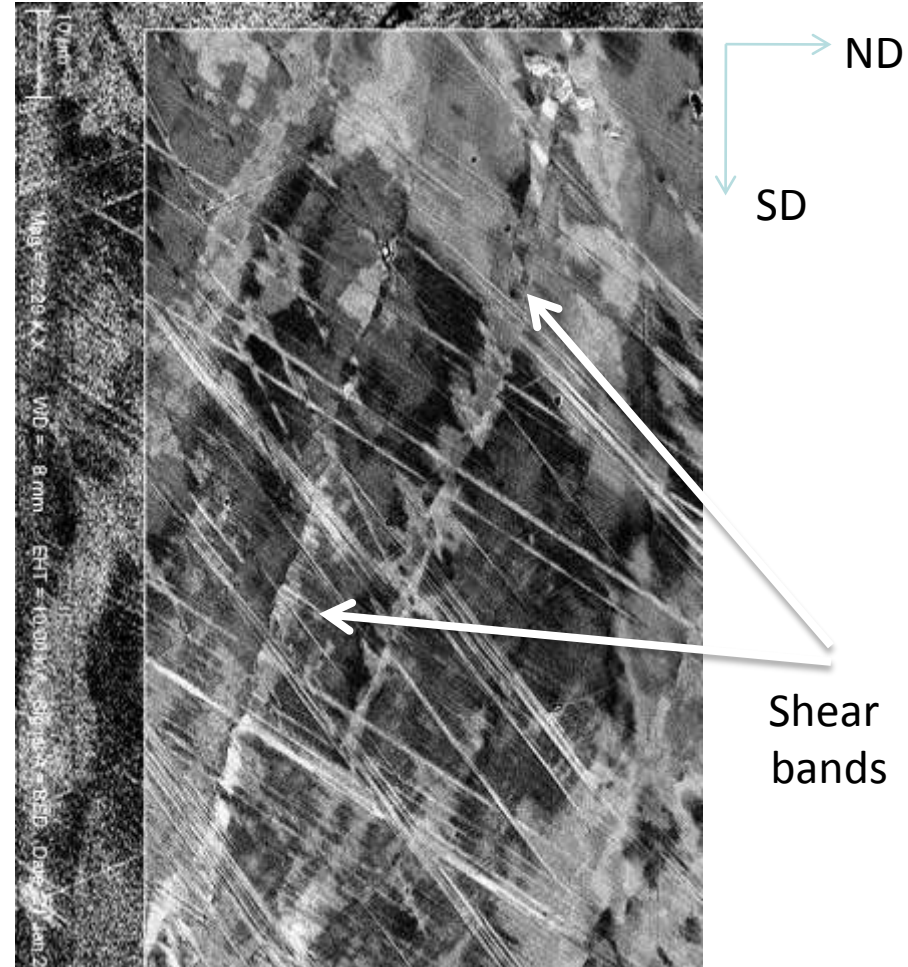
Tensile: dislocation cells



Tensile axis



Shear: symmetric patterning, cell blocks, shear bands



$\epsilon: 0.3$

I. Gutierrez-Urrutia, S. Zaefferer, D. Raabe; Scripta Materialia 61 (2009), 737

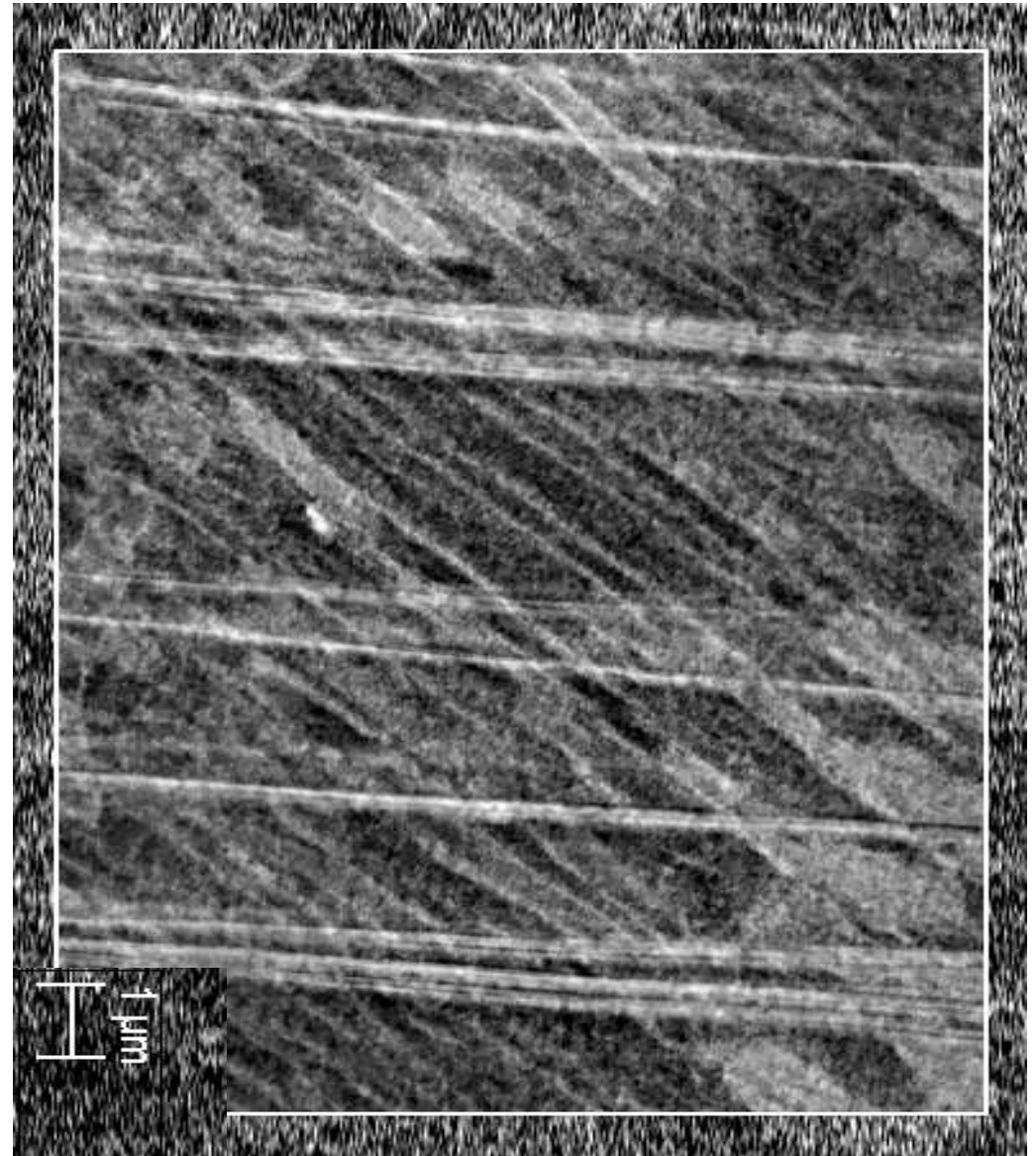
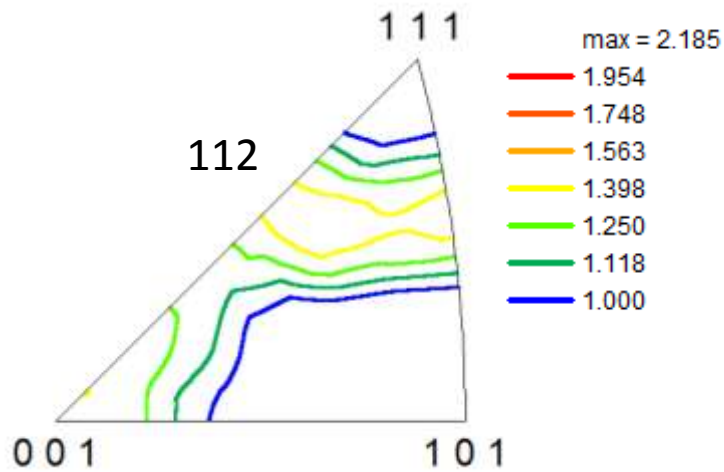
I. Gutierrez-Urrutia, S. Zaefferer, D. Raabe; Materials Science and Engineering A 527 (2010), 3552



- **Electron channeling contrast imaging**
- **Twinning and texture**
- **Strain path effects**
- **Bauschinger effects**
- **Conclusions**

$\varepsilon: 0.1 + (-0.03)$

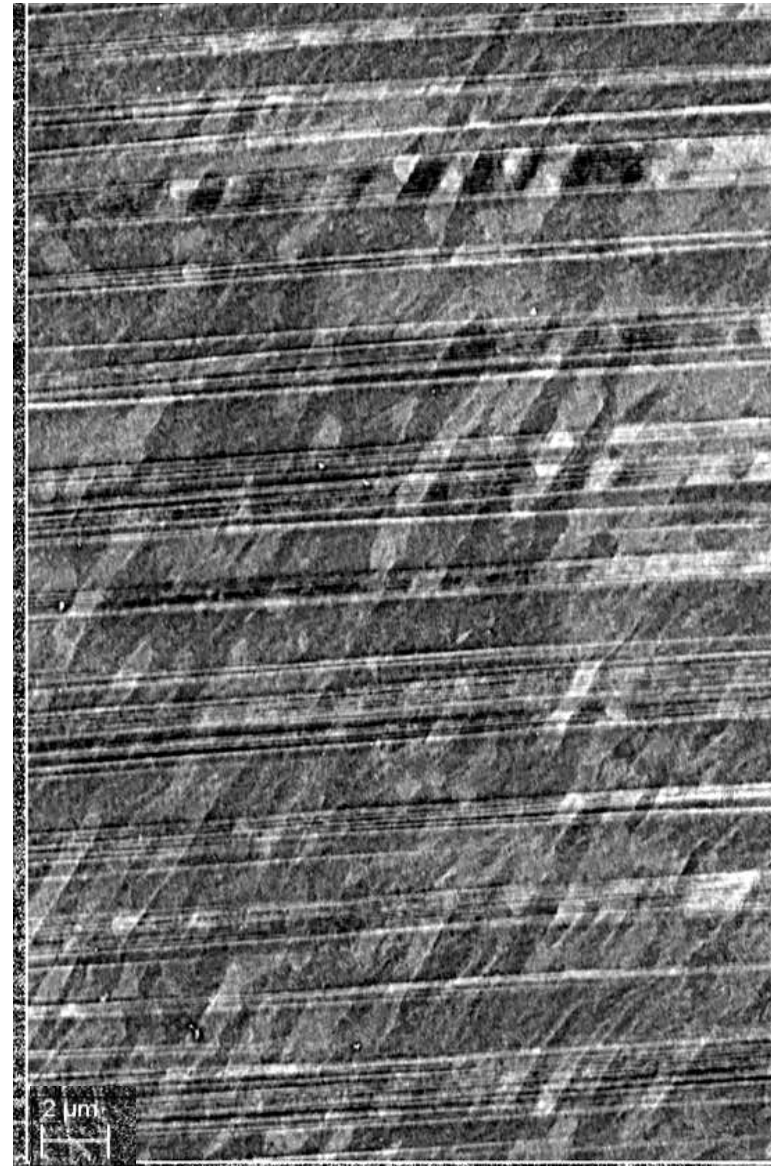
Cell block formation
is enhanced



$\varepsilon: 0.1 + (-0.03)$

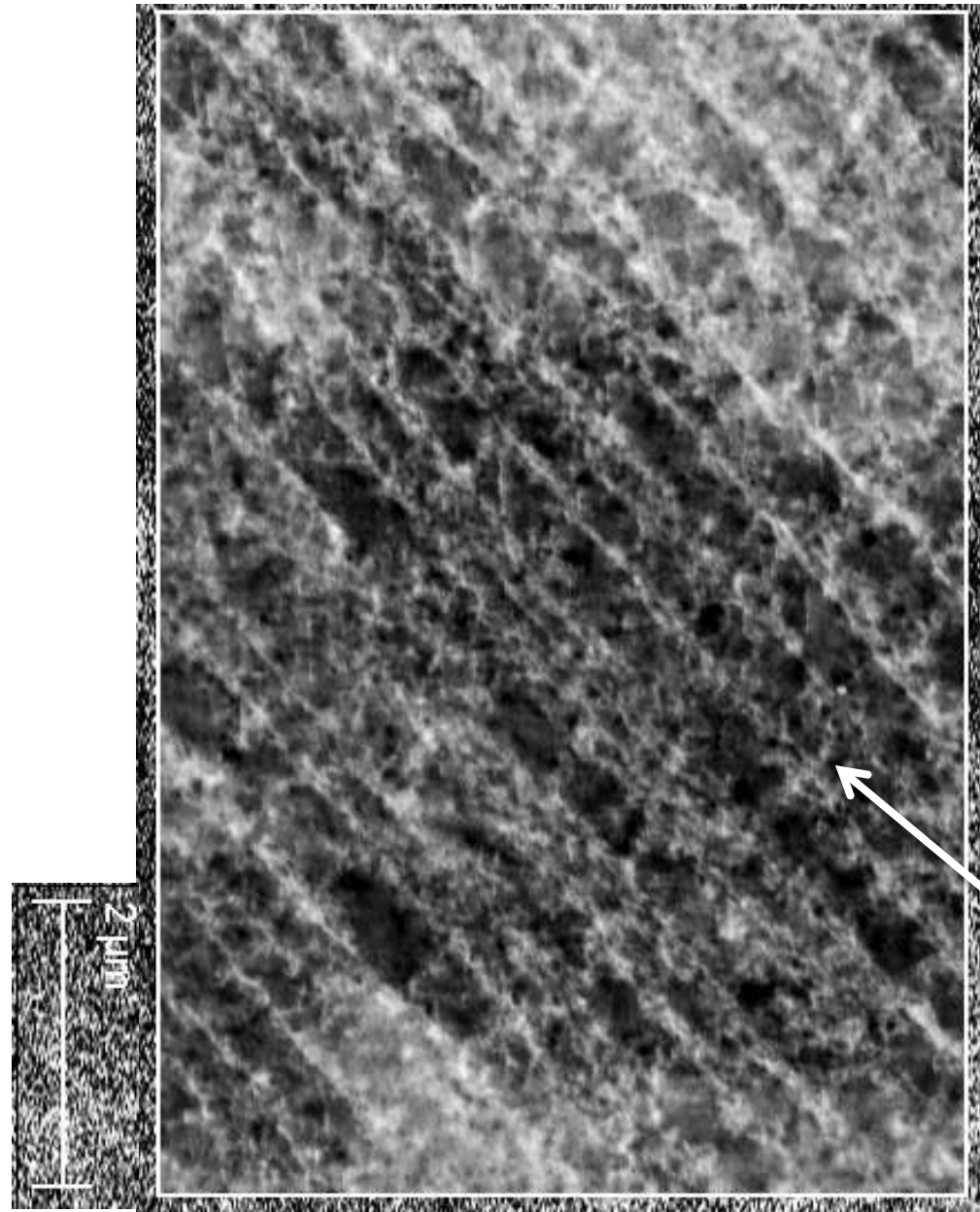
Cell block formation is enhanced (leading to pronounced subgrain structure)

Strain reversal leads to higher misoriented dislocation substructures



$\epsilon: 0.1 + (-0.03)$

ECCI image
(not TEM)



GN boundaries

{111} trace

stat. boundaries

We identify both GN
and incidental
boundaries!



- **Electron channeling contrast imaging**
- **Twinning and texture**
- **Strain path effects**
- **Bauschinger effects**
- **Conclusions**



Joint use of ECCI & EBSD

Unexpected deformation twinning

Dependence of dislocation substructure on strain path and orientation

$\langle 111 \rangle$ //deformation axis leads to planar dislocation substructures: DDWs structures in tension and Taylor lattice in shear

$\langle 001 \rangle$ //deformation axis leads to wavy dislocation substructures: cells in tension and cell block in shear

Strain reversal promotes cell block/subgrain formation with increased misorientation

Cell blocks formed by geometrically necessary boundaries along $\{111\}$ planes and incidental boundaries created by statistically stored dislocations are visible via ECCI. We can estimate boundary spacings and therefore, its contribution to work-hardening.

References for this presentation



Revealing the strain-hardening behavior of twinning-induced plasticity steels: Theory, simulations, experiments

David R. Steinmetz^{a,*}, Tom Jäpel^a, Burkhard Wietbrock^b, Philip Eisenlohr^a,
Ivan Gutierrez-Urrutia^a, Alireza Saeed-Akbari^c, Tilmann Hickel^a, Franz Roters^{a,*},
Dierk Raabe^{a,*}

^a Max-Planck-Institut für Eisenforschung GmbH, Max-Planck-Str. 1, 40237 Düsseldorf, Germany

^b Institute of Metal Forming, RWTH Aachen University, Intzestrasse 10, 52056 Aachen, Germany

^c Institute of Ferrous Metallurgy, RWTH Aachen University, Intzestrasse 1, 52056 Aachen, Germany

Received 25 August 2012; received in revised form 12 September 2012; accepted 17 September 2012

Available online 1 November 2012

Abstract

We present a multiscale dislocation density-based constitutive model for the strain-hardening behavior in twinning-induced plasticity (TWIP) steels. The approach is a physics-based strain rate- and temperature-sensitive model which reflects microstructural investigations of twins and dislocation structures in TWIP steels. One distinct advantage of the approach is that the model parameters, some of which are derived by ab initio predictions, are physics-based and known within an order of magnitude. This allows more complex microstructural information to be included in the model without losing the ability to identify reasonable initial values and bounds for all parameters. Dislocation cells, grain size and twin volume fraction evolution are included. Particular attention is placed on the mechanism by which new deformation twins are nucleated, and a new formulation for the critical twinning stress is presented. Various temperatures were included in the parameter optimization process. Dissipative heating is also considered. The use of physically justified parameters enables the identification of a universal parameter set for the example of an Fe–22Mn–0.6C TWIP steel.

© 2012 Acta Materialia Inc. Published by Elsevier Ltd. All rights reserved.

Keywords: Constitutive modeling; Strain hardening; Twinning; TWIP steels

1. Introduction

Mechanical twinning is an important deformation mechanism that interacts closely with dislocation glide to provide a complex strain-hardening behavior in low stacking fault energy (SFE) face-centered cubic (fcc) metals and alloys. There have been a number of proposed models to simulate the hardening behavior of low-SFE fcc metals that are either phenomenological or are physically-based but lack certain features, such as dislocation cells, and the ability to predict the influence of temperature and/or strain

rate on deformation behavior over a wide domain of parameters. A number of physically based models describing the strain-hardening response of low-SFE fcc metals exist [1–6] which are capable of describing several deformation stages as well as twin–slip, slip–slip and twin–twin interactions.

When looking beyond these approaches, we found that new experimental investigations have revealed additional important microstructural features, such as networks of dislocation cells and the connection between the existing dislocation substructure and mechanical twinning, ignored in previous models [7–9]. Also, recent ab initio predictions have provided us with reliable and physics-based parameter values and revealed important chemical and thermal trends in the SFE, elastic properties and heat capacity of these alloys [10–13].

* Corresponding authors.

E-mail addresses: d.steinmetz@mpie.de (D.R. Steinmetz), f.roters@mpie.de (F. Roters), d.raabe@mpie.de (D. Raabe).

Our new approach not only incorporates these recent findings but also introduces a multiscale plasticity modeling concept whereby *ab initio* derived quantities are linked with constitutive microstructure evolution equations that are based on internal variables. The main use of such a model is that it provides insight into the mechanisms active in producing the high strength and, more importantly, the concurrent high formability of these materials. It can also deliver initial input variables for a crystal plasticity model built upon the same principles, similar to previous models, such as those developed by Ma et al. [14,15].

The cause of the high strain hardening in low-SFE fcc alloys, particularly high-Mn steels, has been widely discussed [16–25]. Two schools of thought exist. The first states that the interstitial C atoms of C–Mn dipoles interact strongly with dislocations [19]. The bond to the substitutional Mn holds the interstitial atoms in place in the lattice, producing a dynamic strain aging effect. The second idea is that mechanical twins provide barriers to dislocation motion, increasing dislocation storage and thus decreasing their mean free path [25]. Dislocation reactions at twin boundaries have been proposed by Venables [26] and Friedel [27] to support the idea that twin boundaries can be treated as grain boundaries, and these observations were supported by transmission electron microscopy (TEM) images [25,28]. Presented TEM images which help explain the high strain hardening of Hadfield steels by showing the inhomogeneous activation of slip in the matrix and the twin [4].

In this article, we propose a new constitutive model based on the idea that twins produce kinematical barriers to dislocation motion. There are several new aspects to this model: (i) twin nucleation and growth are separated, and the nucleation rate of deformation twins is directly coupled to the microstructure in terms of internal state variables and is not governed by a fitting parameter other than the size of the twin nucleus; (ii) a critical stress for twinning is introduced which corresponds to Mahajan and Chin's nucleation model [29]; (iii) the SFE is temperature sensitive and obtained from thermodynamic calculations with *ab initio* derived interface energies; (iv) back-stresses are decoupled from the critical stress for twin growth by including them directly in the twin nucleation mechanism; (v) the sample temperature, and therefore the SFE, critical twinning stress and dislocation annihilation rates by climb, evolve with deformation owing to dissipative sample heating; and (vi) most importantly, correct true stress–true strain and hardening behavior are predicted over a range of 293–873 K using a single and physically well justified model parameter set. In addition, the first measurements of twin volume fraction based on electron channeling contrast imaging (ECCI), which has a resolution lying between electron backscatter diffraction (EBSD) and TEM, are also presented. Coupled with stress–strain curves taken from compression tests over a wide temperature range, they are used to validate the model.

From a conceptual perspective, the novelty of the approach lies in the fact that physically based model parameters are used, that a universal constitutive model parameter set for the Fe–22Mn–0.6C TWIP steel is derived and that the approach combines *ab initio* derived thermodynamic quantities with a microstructure evolution model to predict twin nucleation. The latter feature enables us to conduct a new calculation of the critical twinning stress, based on the twin nucleation mechanism proposed by Mahajan and Chin [29], and to link it to microstructure evolution and to *ab initio* derived parameters. This enables the user to incorporate first principles information in a seamless fashion into microstructure evolution models.

To be clear, this is an isotropic model of a polycrystalline sample which does not take grain orientation into account; however, one part of the twin nucleation mechanism does provide the ability to include the average effect of the inhomogeneous activation of twin systems under a given external stress in grains of differing orientations [30,31]. It was developed in conjunction with a corresponding crystal plasticity model based on the same internal structure, which will be discussed in a later paper.

The paper is structured as follows: first, existing models for low-SFE fcc metals that twin are reviewed, followed by a review of the literature on proposed mechanisms for twin nucleation. Next, our experimental procedure is briefly described, followed by a detailed explanation of our model. Lastly, our results and a discussion thereof are presented. A conclusion finishes the paper.

2. Existing models accounting for twinning in low-SFE fcc metals (in chronological order)

Rémy presented the first model to explain the deformation behavior of low-SFE fcc metals [32]. It is an isotropic approach with phenomenological elements. He notes that several twin nucleation models are, strictly speaking, growth models, but that Mahajan and Chin's model is a true twin nucleation model [29]. New twins are considered to be thin discs whose length and volume decrease with increasing twin volume fraction. It is mentioned that the number of new twin nuclei must be linked to the dislocation density if a particular dislocation reaction is responsible for creating the twin nucleus. In the model, however, it is actually linked to the matrix strain, it being claimed that the dislocation density is related to it. Rémy takes the matrix strain as equivalent to the applied strain. In order for twins to nucleate, a favorable stress condition must exist. By linking a critical stress to a critical strain, an implicit function of strain is developed for the volume fraction of twins [33]. The work hardening due to the existence of deformation twins is attributed to the coherent twin boundaries, which impede dislocation motion and prevent dislocations from entering the twins, except in the case of complicated dislocation reactions. A Hall–Petch-like phenomenon links the contribution of twins to the flow stress. Good results were obtained for a Co–33Ni alloy at 293 K and 473 K.

Kalidindi presented a model to simulate the strain-hardening behavior of low-SFE fcc metals and incorporated it into a crystal plasticity framework [21,34,35]. The model is based on a temperature-insensitive phenomenological approach. It incorporates twinning as an additional kinematic degree of freedom for shear to the single crystal yield surface similar to slip. It accounts for interactions between the slip and twinning by allowing both to influence hardening rates on the individual slip and twin systems. The model does not include the influence of slip on twin hardening, temperature dependence, twin nucleation and twin growth. As a first attempt, the same viscoplastic power law that was used to describe the slip rate was extended to describe the evolution of deformation twin volume fraction. Since it was shown that low-SFE fcc metals show anisotropic deformation behavior following different deformation paths [18], one of the goals of the model was to predict this anisotropic strain-hardening behavior in path-change experiments. The model was successfully used to predict textures, influenced by microscale shear banding [36,37], and basic stress–strain and hardening characteristics for both simple compression and simple shear deformation paths. The hardening behavior for several low-SFE fcc metals was predicted well. Kalidindi's model provided the kinematic foundations and supplied elements used in later models, such as a phenomenological description of the change in twin volume fraction and the hardening of the twin systems with increasing strain.

Karaman et al. suggested a model for Hadfield steels which uses a power law to describe the nonlinear viscous shear rate on each slip system in each crystal [4]. A hardening formulation was introduced which includes separate parameters for the spacing of grain boundaries and twin boundaries, as well as separate parameters to describe the strength of each type of boundary as a barrier to dislocation motion [30,31]. This means that grain boundaries and twin boundaries affect dislocation storage differently. The constitutive model is incorporated into a crystal plasticity framework using a viscoplastic self-consistent approach. Twin volume fraction evolution is implemented using the predominant twin reorientation scheme [38], whereby a dynamic threshold twin volume fraction induces a self-adjusting behavior which ensures that the reoriented twin volume fraction corresponds to that of the real twin volume fraction. A yield strength of 110 MPa for slip and a critical stress of 115 MPa for twin nucleation were set by the authors as constants. The model successfully predicts no further twinning inside twinned regions, with regions both in twins and between twin lamellae deforming primarily by slip; slip between the twin lamellae, however, plays a more dominant role in accommodating the plastic deformation. Three different average grain sizes were modeled: 100 μm , 300 μm and 1.0 mm. The model correctly predicts the stress–strain response for coarse-grained (300 μm and 1.0 mm average grain size) Hadfield manganese steel, showing good agreement with experimental stress–strain curves measured at room temperature. However, the

random texture in the 100 μm polycrystal materials produced predominantly slip and the simulation did not capture the upward curvature of the stress–strain curve. The twin reorientation scheme allowed for accurate predictions of hardening behavior and texture evolution in single and polycrystals.

Bouaziz and Guelton introduced a physics-based model which accounts for the interaction between twinning and dislocation motion by incorporating the characteristic spacing of twins into the dislocation storage [3]. The dislocation density and twin volume fraction are the microstructural state variables. The evolution of dislocation density is a combination of dislocation multiplication and annihilation which includes the mean free path (MFP), while the evolution of twin volume fraction is a function of the existing twin volume fraction, strain and a model parameter dependent on the SFE.

Allain et al. extended Bouaziz and Guelton's model to use the Franciosi interaction matrix to include slip–slip interactions [39,1]. The MFP of dislocations and the evolution of dislocation density are calculated in a similar manner to the Bouaziz and Guelton model, with the exception that a symmetrical slip–twin interaction matrix is used to model cross-hardening from non-coplanar slip and twin systems. They were also the first to include temperature dependence in the viscoplastic shear rate formulation in a constitutive model of low-SFE fcc metals that twin. Following Rémy, a more sophisticated description of the evolution of twin volume fraction which considers the volume of a newly formed twin is presented [32]. The critical stress for twinning has three components: back-stress due to the extension of a stacking fault, self-stress due to dislocation curvature and stress due to dislocation pile-ups. In conjunction with the applied stress, a twin nucleation rate for each twinning system is calculated. Good agreement between constitutive model simulations and experiments are seen at room temperature and 673 K regarding the stress–strain response; the dislocation MFP, which is the average distance a dislocation travels before becoming stored; and the number of grains which had one or two twin systems activated.

Cherkaoui presented a crystal plasticity model for deformation behavior of low-SFE fcc metals [40]. Twins are treated as expanding ellipsoidal inclusions using an extended energy balance from Eshelby, and slip and twinning both have individual flow rules. The purpose of the model was to exploit the competition between slip and twinning, and showed promising results when compared to experimental data from literature.

Bouaziz et al. introduced the Bauschinger effect (BE) to explain the effect of grain and twin boundaries on the hardening mechanisms in TWIP steels [41]. It built on Bouaziz's and Allain's previous models [3,39,1]. A back-stress due to the kinematical hardening produced from the BE was added to the flow stress. It included a factor for the number of dislocation loops piled-up at a boundary, whose evolution with strain was given. Only one fitted model parameter

was introduced to account for this extra stress component, namely, the maximum number of dislocation loops at a boundary. The Kocks–Estrin (KE) dislocation density evolution equation was updated to include the BE, and a new empirical equation for the evolution of twin volume fraction was presented. The grain size effect and back-stress simulations matched experiments well, and it was shown that the critical strain for onset of twinning increases with grain size, but the stress at the critical strain was always 550 MPa. Mingxin et al. used this same model to show the maximum number of dislocation loops at a boundary is a linear function of the carbon content [42].

The constitutive model introduced by Shiekhelsouk et al. [5] is built from the grain level up [5]. A polycrystal is taken as the representative volume element, and grain orientations are assigned. The constitutive model was incorporated into a self-consistent crystal plasticity framework. The single-crystal viscoplastic strain rate for slip is the sum of the product of the Schmid tensor and the slip rate on each system, while that for twinning is the sum of the product of the Schmid tensor for twinning systems, the characteristic twinning shear and the instantaneous rate of twinning. Twinning is not allowed in twinned regions, and no twin reorientation scheme was employed. Both temperature and rate dependence are incorporated into the slip rate. The plastic spin tensor is used to calculate lattice rotations based on crystallographic slip. These rotations are the primary contributor to texture evolution due to the small volume fraction of twins. The shear stress is directly linked to the total forest dislocation density. Activated twin systems that are non-coplanar to the active slip system, grain size and dislocation density are included in the calculation of the MFP by a harmonic mean. A power-law-type evolution law was used to model twin kinetics. The temperature dependence of the critical shear stress for twinning is represented by the temperature dependence of the SFE [43]. The increasing resistance to twinning is exhibited through twin–twin interactions [44], which are represented here by hardening equations first proposed by Kalidindi [21]. Slip parameters were fitted against experimental data at 673 K, where no twinning should exist. Twin parameters were fitted at 298 K. There was a good correlation between the experimental and simulated stress–strain curves for the two temperatures. In the one hardening curve shown, the hardening increases slightly after its initial precipitous decline, but fails to capture the hump characteristic of high-Mn TWIP steels. Good correlation was observed between the fraction of grains showing zero, one or two active twin systems, as well as with the dislocation mean free path due to twinning.

Kim et al. introduced a constitutive model for Al-TWIP steel which included the effect of dynamic strain aging (DSA) [45]. It uses a modified KE model of coupled mobile and forest dislocations whose evolution contributes to hardening by the constriction of their MFP by twins. The twin volume fraction evolves according to the phenomenological law first proposed by Bouaziz et al. [41]. An additive

term for DSA is included in the flow stress calculation. Twinned and untwinned grains are treated separately, and the rule of mixtures is used to combine the two. The model parameters were fitted to experimental observations of dislocation density by TEM and the fraction of twinned grains by EBSD, providing good results for a single room-temperature tensile flow curve. It was concluded that the contribution of DSA to the overall flow stress is minor.

Dancette et al. presented a crystal plasticity model for texture development and hardening in TWIP steels [6]. One purpose of the paper was to compare three different scale transition schemes from the grain scale to the macroscale: a multisite model, a Taylor-type model and crystal plasticity finite element modeling (CPFEM). The hardening is governed twofold: by the restriction of the MFP of dislocations calculated by a harmonic mean, including grain size, dislocation density and the twin volume fraction (through Fullman's analysis); and by dynamic recovery through the Kocks–Mecking–Estrin model. Dancette et al. [6] use Kalidindi's framework [34] for deformation by twinning in the parent grain; no mention of twin volume fraction evolution is made, leading to the assumption that it is the same as Kalidindi's. The model matches the stress–strain and hardening behavior of unstrained and prestrained samples in tensile tests at room temperature. Twin volume fraction data were obtained from EBSD scans, making assumptions to account for the large difficulty in indexing the nanotwin lamellae with the EBSD technique. This allowed direct comparison of active twin systems, grain average orientation and twin orientation for a large number of individual grains. Simulation of texture evolution, lattice orientation of the twins and twin volume fraction evolution for non-prestrained tensile test samples at room temperature match experimental data quite well. Considering the scale transition schemes, the multisite model was determined to be a good, computationally sparing approach (compared to CPFEM) for up to moderate strains (30%), while CPFEM was best at large deformations. At the grain level, the multisite model and CPFEM were better than the isostrain (Taylor) or isostress approaches.

Barbier et al. [2] presented a crystal plasticity model, based on Shiekhelsouk et al.'s model [5], in which a representative volume element of 3000 grains was considered. Two homogenization schemes were tested, the Taylor approximation and the translated field model. Anisotropic dislocation slip and twinning were considered using a Kocks–Mecking dislocation density evolution model coupled with a harmonic calculation of dislocation MFP which included grain size, dislocation density and twin interfaces. The evolution of the critical twinning stress was calculated according to Kalidindi's phenomenological hardening law. The evolution of the twin volume fraction accounted for the evolving critical twinning stress, but it uses a phenomenological reference twinning rate. The main purpose of this paper was to investigate and predict texture evolution over multiple strain paths (transverse direction tension, rolling

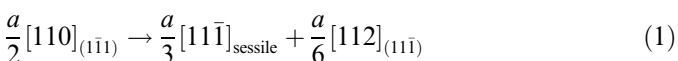
direction tension and rolling direction simple shear). The model results matched experimental results well for all three loading paths, and showed that the simple shear test rotates grains so that they are in an unfavorable orientation for the activation of multiple twinning systems. Because an active twin system non-coplanar to the primary active system inhibits further twin growth, the overall twin volume fraction was higher for simple shear than for both tension tests, where many grains were rotated into favorable orientations to activate a second twin system. The texture, however, was controlled primarily by crystallographic slip.

3. Earlier proposed twin nucleation mechanisms in fcc metals

3.1. The pole mechanism for twin nucleation

Cottrell and Bilby proposed the first mechanism to describe the nucleation and growth of mechanical twins [46]. Their theory focused on the shear produced by partial dislocations moving in the twinning plane, knowingly ignoring the often necessary localized rearrangements of neighboring atoms.

The Cottrell–Bilby mechanism considers three dislocations, b_1 , b_2 , and b_3 , meeting at a node, where b_1 and b_2 do not lie in the slip plane of b_3 . Each revolution of b_3 about the dislocation node, where b_1 and b_2 lead out of the slip plane, produces a simple shear on the slip plane if the Burgers vectors of b_1 and b_2 also lie in the slip plane. However, if they have a component normal to the slip plane whose magnitude is equal to the plane spacing, one revolution of the slip dislocation about the pole will cause a displacement from the origin of one atomic layer. The pole dislocation must be sufficiently anchored that it is immobile under the stress moving the sweeping dislocation. The climb of the dislocation around a helical surface formed due to the perpendicular component of the Burgers vector is the core idea of the pole mechanism. In the fcc lattice, if sufficient energy is available from external sources, the dissociation of a perfect dislocation whose dislocation line lies in one of the (111) planes into a Shockley partial dislocation and a Frank sessile dislocation can occur, e.g.



The perfect dislocation and the Frank dislocation both have Burgers vectors equal to one (111) spacing, rendering them suitable pole dislocations. Because both the Frank sessile and the Shockley partial dislocation reside in the (111) plane, the Shockley partial will meet the Frank sessile as it sweeps around the pole dislocation. Only one revolution can occur, resulting in a monolayer stacking fault. In addition to the Frank sessile acting as a barrier, another revolution of the sweeping dislocation on the (111) plane would result in an illegitimate stacking sequence where nearest neighbors are not close-packed.

To solve this problem, Venables suggested a modified pole mechanism [47]. Analogous to Cottrell and Bilby, a

prismatic dislocation dissociates into a Frank sessile and a Shockley partial, creating a stacking fault. After one revolution about the pole, they recombine to form the original perfect dislocation, leaving behind a stacking fault layer. The perfect dislocation is free to glide prismatically to the neighboring close-packed plane, where the dissociation can again occur and the process can repeat itself. Repeated operation of the source on consecutive close-packed planes produces a twin. Venables [47] used experimental data of Blewitt et al. [48] in consideration of the source dislocations of such a mechanism. Glide sources – those perfect dislocations and their corresponding partial dislocations which exist in the slip plane – were shown to require either compressive, rather than tensile, stresses in order to extend the stacking fault or prohibitively high applied shear stresses and short source lengths. Those dislocation reactions which calculations indicate to be most favorable for twinning are not observed experimentally. Glide sources were thus ruled to be highly unlikely to nucleate twins. The three perfect prismatic dislocations that are not in the primary slip plane are considered as twin sources. According to experiments, one is deemed unimportant because the shear stress acting on the Shockley partial is never high. Only one of the two remaining dissociations will lead to an expansion of the intrinsic fault. Therefore, the same type of dissociation seen in Eq. (1) is important for twinning on the primary twin plane. It was reasoned that the most probable way for the prismatic $a/2[110]$ dislocation to acquire an extended jog on the primary twin plane is by repeated intersection with a Frank–Read source on the primary slip plane.

The Shockley partial dislocations rotating in opposite directions around the poles will meet one atomic plane apart and will not be able to pass one another. Seeger [49] suggested that passage would be possible if the twinning partial acquires enough kinetic energy. However, Venables argued that it is not necessary for the passing stress to be overcome by kinetic or applied energy if repeated activation of the twin source occurs. Unit jogs along the prismatic dislocation in the slip plane one level above the stacking fault are expected to have a lower energy than multiple jogs if the pole dislocation's nature is not entirely of a screw character. In addition, the twin source can dissociate easiest when it is on the atomic plane above the stacking fault. For this reason, unit jogs are preferably formed, and the dislocation dissociation takes place, reactivating the twin source. Another monolayer stacking fault emerges. Partials of opposite sign annihilate where the two monolayer stacking faults meet, resulting in a bilayer fault with partial dislocations at each end.

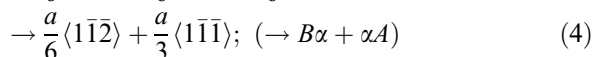
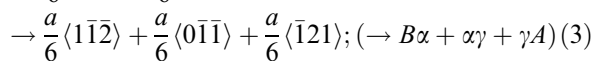
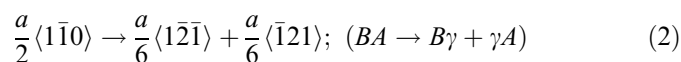
The pole mechanism can be questioned because of the very high static passing stress required for the first revolution about the pole. For the most conservative case of two partial screw dislocations passing one another separated by a single (111) interatomic spacing, the passing stress for Fe–22Mn–0.6C TWIP steel is 3.6 GPa. It is possible that dislocation inertia helps in overcoming this, but to our knowledge this has not yet been clarified.

3.2. Alternative mechanisms for twin nucleation

Cohen and Weertman proposed a twin nucleation model consisting of a specific dissociation of perfect dislocations due to dislocation pile-ups at Cottrell–Lomer locks which is normally not energetically favorable [50,51]. Due to the pile-up stress, Shockley partial dislocations are forced together and the perfect dislocations are able to split into sessile Frank partial dislocations of the $a/3[111]$ type and glissile Shockley partial dislocations of the $a/6[11\bar{2}]$ type. This is the same reaction that Venables proposed as the basis of his modified pole mechanism, though he gave no reason as to why this particular reaction should take place [47]. This reaction should not normally occur, however, because the dislocation energy remains constant. In contrast, a dissociation into two Shockley partials lowers the overall energy of the dislocation. Cohen and Weertman justify the dissociation by claiming that the appropriate stress factor is generated at dislocation pile-ups.

The Shockley partial is formed in the conjugate slip plane and glides away from the sessile Frank partial, forming an intrinsic stacking fault. Many Cottrell–Lomer locks are created on parallel planes in a slip band which become the source of multiple stacking faults. In order for a twin to form, these stacking faults must be on directly adjacent atomic planes. Twins produced in this manner would be imperfect, exhibiting a series of matrix and twin lamellae, since not every twin plane in a large volume would have a stacking fault.

Fujita and Mori proposed a stair-rod cross-slip mechanism similar to that of Cohen and Weertman [52]. Perfect dislocations on the conjugate slip plane interact with groups of dislocation dipoles on the primary slip plane (instead of dislocation pile-ups in the case of Cohen and Weertman [50,51]), which provide strong barriers to dislocation motion. Here a stair-rod cross-slip process is initiated whereby a sessile Frank partial dislocation on a (111) plane and a glissile Shockley partial dislocation on the primary slip plane are produced according to the following type of reaction:



The dislocation reactions according to the convention of Thompson's tetrahedron are shown in parentheses.

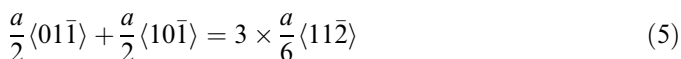
Miura et al. [53] proposed a twin nucleation model based on dislocation pile-up at a Lomer dislocation at the junction of the primary plane and a cross-slip plane. Two Shockley partial dislocations and a Frank sessile dislocation are created in the dislocation reaction. These subsequently create a double-layer stacking fault which serves as the twin nucleus. The model is referred to in the literature as the MTN (Miura–Takamura–Narita) model. As

the temperature increases, the stress concentration created by the pile-up is relieved by cross-slip and twinning does not occur. The orientation dependence of twinning is also considered.

Karaman et al. [4] extended the MTN model by providing an experimentally supported calculation of the critical twinning stress which was dependent on orientation, solid solution hardening, and applied stress. The original model did not include the latter two effects. An effective SFE which was dependent on the applied stress and orientation was given that could vary up to 50%. Combining these calculations with single crystal experiments, correct predictions for twinning could be made in three loading directions. The orientation dependence of the SFE also allowed for an explanation of the strong tension–compression asymmetry observed in Hadfield steels.

3.3. Three-layer stacking fault

The twin nucleus used in our model was first proposed by Mahajan and Chin [29]. It is a mechanism in which two perfect dislocations split into fault pairs and react on the primary slip plane to produce three Shockley partial dislocations on adjacent planes. The partial dislocations in each stacking fault are separated by the balance of attractive forces due to the stacking fault and the repulsive forces due to the partial dislocations. The force necessary to bring the inside partial dislocations of the two stacking faults to within a distance of 10 Å, which represents an extreme case, requires a stress concentration to be achieved by a dislocation pile-up. Due to the repulsive force between the two partial dislocations, atoms in the core of one can rearrange so that it can glide on the adjacent slip plane. If a third fault pair approaches one side of this double stacking fault arrangement, the two partials constituting the boundary of the double-layer fault can combine and move to the next adjacent layer and slip away, creating a three-layer stacking fault. The Shockley partials on one side of the fault form an interface whose Burgers vectors sum to zero, making the interface immobile under the applied stress. This leaves the Shockley partials on the opposite side of the stacking fault free to move away from the interface. The twin nuclei are formed by the reaction of perfect dislocations on two coplanar slip systems in the following reaction:



A schematic of the twin nucleus is shown in Fig. 1. The twins would then form when these three-layer stacking faults inside a slip band on adjacent slip planes grow into one another.

Mahajan and Chin [29], Kibey et al. [54,55] and Bracke et al. [56] showed evidence of this type of twin nucleation mechanism in fcc materials, while Karaman et al. [4] and Idrissi et al. [57] claimed that the MTN model fits with their observations. There thus appears at the moment to be no

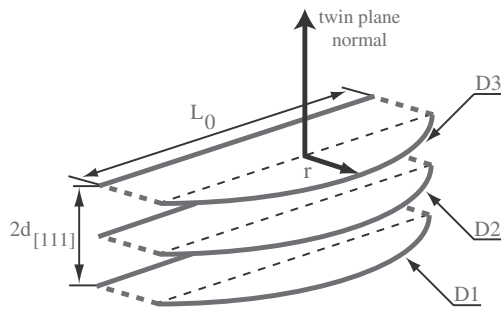


Fig. 1. The twin nucleus proposed by Mahajan and Chin and used in this model. $d_{[111]}$ is the interplanar spacing in the $\langle 111 \rangle$ direction, L_0 is the length of the sessile partial dislocations forming the twin nucleus and r is the distance the mobile partial dislocations have bowed out. $D1$, $D2$ and $D3$ are the mobile Shockley partial dislocations which bow out to form the twin.

consensus in the literature. It may also be possible that different twin nucleation mechanisms are active under different circumstances. An overview of twinning is given in the seminal paper by Christian and Mahajan [33].

4. Experimental procedure

4.1. Materials

An overview about the effects of chemical composition, strain rate and temperature that covers the stress–strain curves used within this project is given by Wietbrock et al. [58]. That paper focuses on isothermal compression tests of three ternary high-manganese steels, with 22 and 28 mass percent manganese and 0.3 and 0.6 mass percent carbon; however, only the Fe–22Mn–0.6C material was used for the present paper.

4.2. Compression tests

The isothermal compression tests were conducted on a computer-controlled 1200 kN servo-hydraulic testing system manufactured by Servotest Ltd. The tests were conducted between room temperature ($RT = 293$ K) and 873 K. For all temperatures except RT, each specimen was heated up for 3 min before upsetting at the respective forming temperature inside the furnace which is integrated into the testing machine. The compression was performed nearly isothermally in a single hit to a maximum true strain of 0.7 at a constant strain rate of 0.1 s^{-1} . The friction was reduced by filling the lubrication slots with polytetrafluoroethylene. Each specimen was quenched in water immediately after compression.

4.3. Fitting procedure used for identifying a universal model parameter set

A characteristic feature of our approach is the physics-based nature of the model parameters, some of which are derived from ab initio predictions. This means that we

know the order of magnitude of almost all the model parameters to be adjusted. Upper and lower bounds were hence included in the optimization function, making sure the solution is physically viable. As a fitting procedure to adjust the parameters within these bounds, an automated curve-fit process was used because many of the model parameters have strong non-linear influences on one another. In the program Matlab (The MathWorks, Inc.), the optimization function `fmincon()` from the Optimization Toolbox was used. This function finds the minimum of a constrained multivariate non-linear function. In addition, a custom-written particle swarm optimization function was also tested. This proved to be more robust at searching the entire parameter space, but took longer than the gradient-based method to converge upon a solution. The sum of the squared deviation between simulated and experimental data (stress–strain or hardening–strain) served as the target function, and the fitted model parameters were the variable inputs.

4.4. Microscopy

ECCI [59,60,30,61] was used for microstructural investigations. In this scanning electron microscope (SEM) technique, the grain orientations of a standard SEM sample are measured using EBSD, then individual grains are rotated into the Bragg condition, providing backscattered electron contrast near features which distort the lattice, such as dislocations [59,61]. An accelerating voltage of 10 kV was used. The resolution of ECCI is not as good as that of TEM, but the increased observable area (wide field of view) and the ease of sample preparation are major advantages [7]. ECCI was used for microstructural observations to decide which state variables should be included in the model and also for the measurement of the twin volume fraction [9].

There have been few reports on the twin volume fraction of high-Mn steels due to the morphology of the twins. Many are between 10 and 30 nm thick, making them nearly invisible to conventional EBSD. TEM is able to resolve the twins, but has a limited observable area, preventing the collection of reliable statistics. The twins often form in bundles, however, and the image quality of the EBSD patterns decreases near these twin bundles. A few authors have used the backscatter Kikuchi pattern image quality as a metric to measure the twin volume fraction [6,62,63], though quantitative information about the twin thicknesses could not be obtained.

5. Structure of the new constitutive model

Investigations of Fe–22Mn–0.6C (wt.%) using many experimental techniques, including ECCI, TEM and EBSD, have shed light on the important aspects of the microstructure of this complex class of material [7,8,62]. These are namely grain size, mechanical twins and dislocation cells. Fig. 2 presents ECCI images clearly showing

grains exhibiting dislocation cells, as well as zero, one and two active twin systems. Our approach assumes that a combination of the three-internal-variables model (3IVM) [64] with mechanical twins would describe these essential microstructural features. The important features that we have chosen to include in this model involve mobile dislocations in the dislocation cell interior, mobile dislocations inside dislocation cell walls, dislocation dipoles in the dislocation cell walls and mechanical twins. The important internal state variables are then those respective dislocation

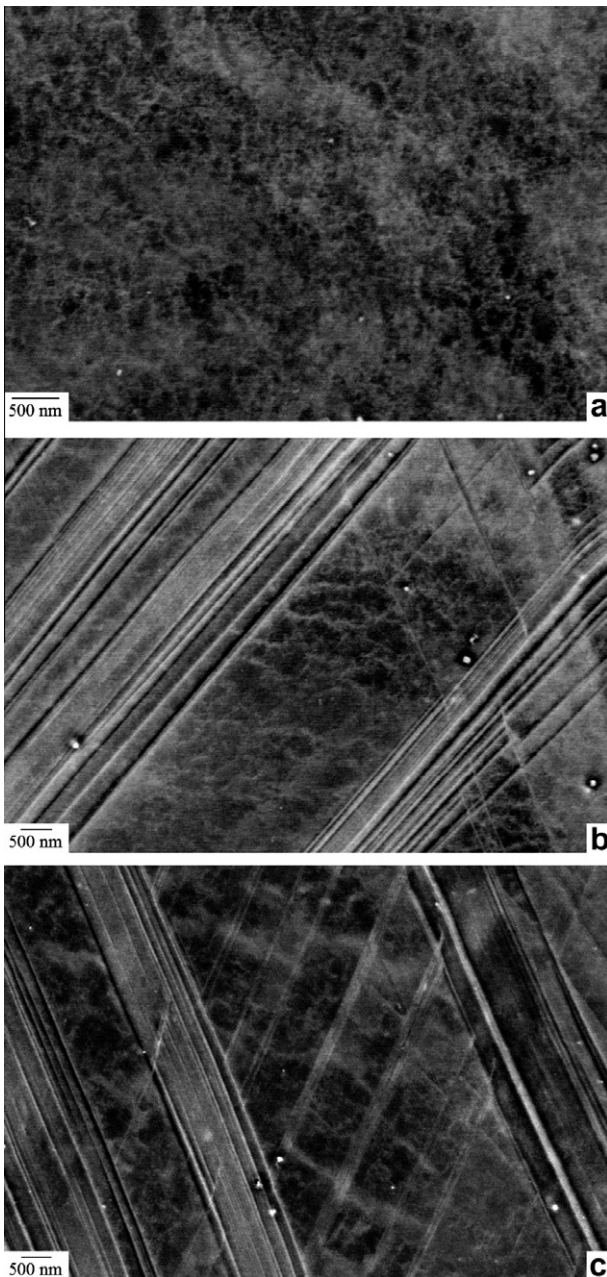


Fig. 2. ECCI images taken in an SEM of Fe–22Mn–0.6C TWIP steel at various stages of deformation: (a) dislocation cells, (b) dislocation cells with one activated twin system and (c) dislocation cells with two activated twin systems.

Table 1
Slip constants.

	Description	Value
G	Shear modulus	52.5 GPa
b	Burgers vector	2.56×10^{-10} m
$\dot{\epsilon}$	Strain rate	0.1 s^{-1}
ν	Poisson ratio	0.33
M	Taylor factor	3.06
D_0	Self-diffusion coefficient for iron	$4.0 \times 10^{-5} \text{ m}^2 \text{ s}^{-1}$
n	Number of active slip systems	3
d	Grain size	50 μm

densities and the volume fraction of mechanical twins: ρ_c , ρ_w , ρ_d , f_{tw} .

5.1. Evolution of dislocation densities

The evolution of the dislocation densities is given by the following equations:

$$\dot{\rho}_c = \frac{\dot{\epsilon}M}{b} \left(\frac{1}{i_c} \sqrt{\rho_c} - \frac{2d_d}{n} \rho_c \right) \quad (6)$$

$$\dot{\rho}_w = \frac{\dot{\epsilon}M}{b} \left(\frac{1}{i_w} \sqrt{\rho_w} - \frac{2d_d}{n} \rho_w \right) \quad (7)$$

$$\dot{\rho}_d = 2 \frac{\dot{\epsilon}M}{bn} \left\{ (d_d - d_a) \left[\rho_w + \rho_c \left(\frac{f_c}{f_w} \right) \right] - d_a \rho_d \right\} - \frac{2\rho_d v_{\text{climb}}}{d_d - d_a} \quad (8)$$

where $\dot{\epsilon} = 0.1 \text{ s}^{-1}$ is the externally imposed strain rate, $b = 2.56 \text{ \AA}$ is the Burgers vector, $M = 3.06$ is the Taylor factor, $n = 3$ is a constant for the number of active slip systems, $f_c + f_w = 1$ are the volume fractions of the dislocation cell interiors and the dislocation cell walls, set to 0.9 and 0.1, respectively [64], i_c , i_w are parameters quantifying the average number of dislocation spacings that a dislocation moves before becoming sessile and d_a is the minimum stable dipole distance before spontaneous annihilation occurs. The symbols are also defined in Tables 1–3. The dislocation climb velocity is given by:

$$v_{\text{climb}} = \frac{D_0}{kT} \frac{G\Omega}{\pi(1-\nu)d_d} \exp\left(\frac{-Q_c}{kT}\right) \quad (9)$$

Here, $D_0 = 4.0 \times 10^{-5} \text{ m}^2 \text{ s}^{-1}$ is the self-diffusion coefficient for fcc Fe, ν is the Poisson ratio, G is the shear modulus, Ω is the activation volume for climb, and Q_c is the sum of the vacancy formation and migration energies. The variables k and T are the Boltzmann constant and the absolute temperature. d_d , the maximum glide plane distance two dislocations can have to form a dipole, is calculated by:

$$d_d = \frac{Gb}{8\pi(1-\nu)\tau_{\text{eff},w}} \quad (10)$$

The derivation of the evolution equations and evolution of the dislocation densities is described in detail in an earlier paper by Roters et al. [64].

Table 2
Optimized slip parameters.

Description	Value	
d_a	Minimum stable dipole separation	1.93b
Q_s	Activation energy for slip	4.17 eV
Q_c	Activation energy for climb	2.33 eV
Ω	Activation volume for climb	1.53b ³
τ_0	Solid solution contribution	72.9 MPa
α	Passing coefficient for shear	0.1
q	Top of the obstacle profile	1
p	Tail of the obstacle profile	1
$i_{c,w}$	Average dislocation spacings a dislocation travels	5.43

Table 3
Optimized twinning parameters.

Description	Value	
i_{tw}	Average twin spacings a dislocation travels	5.52
L_0	Width of twin embryo	260 nm
s	Transition profile width exponent	13.96
V	Activation volume for cross-slip	b ³

The glide resistance is calculated from the following equation [65]:

$$\hat{\tau} = \tau_0 + \alpha Gb\sqrt{\rho} \quad (11)$$

Separate glide resistances are calculated for the cell interior and the cell wall due to the individual dislocation densities. The variable α is the passing coefficient for shear, G is the shear modulus, b is the magnitude of the Burgers vector, ρ is the dislocation density and τ_0 is the athermal solid solution strength component of the glide resistance.

The strain rate is expressed as:

$$\dot{\epsilon} = \frac{\dot{\gamma}}{M} = \frac{Av_0b\rho}{M} \exp\left(-\frac{\Delta G}{kT}\right) \quad (12)$$

where $\dot{\gamma}$ is the shear rate, Λ is the mean free path, v_0 is the Debye frequency, ρ is the mobile dislocation density and ΔG is the activation energy for slip. A modified glide resistance profile is used with the equation given by Kocks, et al. [66]. The activation energy is therefore taken as:

$$\Delta G = Q_s \left[1 - \left(\frac{\tau_{\text{eff}}}{\hat{\tau}} \right)^p \right]^q \quad (13)$$

The variables p and q are model parameters which are defined by the obstacle profile, τ_{eff} is the resolved shear stress and Q_s is the activation energy for slip. The combination of Eqs. (11)–(13) produces a strain rate given by:

$$\dot{\epsilon} = \frac{Av_0b\rho}{M} \exp\left(-\frac{Q_s}{kT} \left[1 - \left(\frac{\tau_{\text{eff},x}}{\tau_0 + \alpha Gb\sqrt{\rho_x}} \right)^p \right]^q \right) \quad (14)$$

where x represents c or w . The resolved shear stress is calculated individually for the cell interior ($\tau_{\text{eff},c}$) and the cell walls ($\tau_{\text{eff},w}$), and is combined through a mixing law to form an averaged resolved shear stress to be used later in Eq. (30) to calculate the probability of twin nucleation:

$$\sigma_{\text{ext}} = M\tau_{\text{RSS}} = M(f_c\tau_{\text{eff},c} + f_w\tau_{\text{eff},w}) \quad (15)$$

f_c and f_w are user-defined constants which represent the volume fraction of the dislocation cell interior and dislocation cell walls, summing to one. In this case they were set to 0.9 and 0.1, respectively.

5.2. Evolution of the mean free path

In a typical Kocks–Mecking-type of constitutive model [65], in which dislocation densities are the primary state variable for describing the hardening behavior, the ratio between the increment in slipped area and the increment in (deposited) dislocation length is the decisive measure resulting in strain hardening:

$$d\rho = \frac{d\gamma}{b\Lambda} \quad (16)$$

The parameter Λ is the MFP. In reality, numerous phenomena contribute to the MFP and its change upon straining, including, but not limited to, grain size, existing forest dislocation density and, in materials that twin, the spacing of the mechanical twins.

The symbols i_c , i_w are model parameters which quantify the average number of dislocation spacings that a dislocation moves before becoming sessile. It is the analog to the reciprocal of the fitting parameter k found in similar models, but has a more tangible physical meaning here. We follow several authors [1,3,39,67] and choose to use a harmonic mean to calculate the MFP in the model presented here. There is no universal MFP in this model, but rather one in the cell interior and one in the cell wall:

$$\frac{1}{\Lambda_c} = \frac{\sqrt{\rho_c}}{i_c} + \frac{1}{d} + \frac{1}{i_{tw}t} \quad (17)$$

$$\frac{1}{\Lambda_w} = \frac{\sqrt{\rho_w}}{i_w} + \frac{1}{d} + \frac{1}{i_{tw}t} \quad (18)$$

The symbol Λ_c represents the MFP of single mobile dislocations inside dislocation cells, Λ_w is the MFP of single mobile dislocations inside dislocation cell walls, d is the grain size and t is the MFP due to twins being present. The number of twin spacings that it travels before becoming sessile in the case of twinning is i_{tw} . If dislocations travel coplanar to twins, they could travel more than one average twin spacing.

The twinning MFP evolves according to Fullman's stereological relationship [68]:

$$\frac{1}{t} = \frac{1}{2e} \frac{f_{tw}}{(1 - f_{tw})} \quad (19)$$

where f_{tw} is the twin volume fraction and e is the average twin width, or the average width of a twin bundle if they exist. A discussion of the evolution of f_{tw} follows and is presented in final form in Eq. (33).

5.3. Physical description of twin nucleation

As explained above, the twin embryo proposed by Mahajan and Chin [29] is used in our model to describe

deformation twin nucleation. A schematic of the twin embryo can be seen in Fig. 1. Three stacking faults are on adjacent parallel (111) planes. The straight back lines represent sessile Shockley partial dislocations, while the bowed out front lines represent mobile Shockley partial dislocations. The critical event for the growth of the nucleus into a twin is the bow out of the three partial dislocations between the pinning points separated by L_0 . Twin growth is determined by the overall energy of the system. This has three contributions:

$$Q_{\text{work}} = -3b_s \tau_{\text{rss}} A(r, L_0) \quad (20)$$

$$Q_{\text{sf}} = \gamma_{\text{sf}} A(r, L_0) \quad (21)$$

$$Q_{\text{line}} = \frac{9}{2} G b_s B(r, L_0) \quad (22)$$

where Q_{work} is the energy supplied by the applied shear stress τ_{rss} , Q_{sf} is the energy required to extend the stacking fault and Q_{line} is the energy required to extend the dislocation line. The symbol γ_{sf} represents the SFE, b_s is the Burgers vector of the Shockley partial, $A(r, L_0)$ is the area function and $B(r, L_0)$ is the dislocation line length.

The total energy of the system is then:

$$Q_{\text{total}} = Q_{\text{work}} + Q_{\text{sf}} + Q_{\text{line}} \quad (23)$$

For high applied stresses, the energy is constantly decreasing, but for a particular stress level a saddle point is found at $2r = L_0$, as shown in Fig. 3. The saddle point is very sharp in stress, creating a steep increase in the activation barrier for small decreases of the stress, resulting in an essentially athermal barrier stress. At this point, the mobile partial dislocations will have formed a semicircle between the two pinning points. The stress at this configuration is defined as the critical twinning stress for twin formation and is given by:

$$\tau_c = \frac{\gamma_{\text{sf}}}{3b_s} + \frac{3Gb_s}{L_0} \quad (24)$$

The SFE plays a large role in defining the critical twinning stress. Due to its strong temperature dependence, SFEs calculated thermodynamically by the method of Saeed-Akbari et al. [69] and corrected by ab initio calculations were used. More specifically, the SFEs were calculated by the sum of the molar surface density along the {111} planes and the γ/ε interfacial energy. The interfacial energy was obtained by ab initio calculations, leading to a more correct estimation of the SFEs. With this approach, the temperature-dependent SFE was updated for each deformation increment to correspond to the actual predicted sample temperature, which increased due to dissipative heating. While a suitable model has been selected to describe the twin nucleus that provides credible values of the necessary applied stress to initiate twinning, no purely physical model exists that can explain the frequency with which this event occurs, and hence the increase in twin population as a function of strain. Rémy [32] and Allain et al. [1] suggest it should be tied to dislocation density, and do so by stating that mobile dislocation activity is necessary for strain and

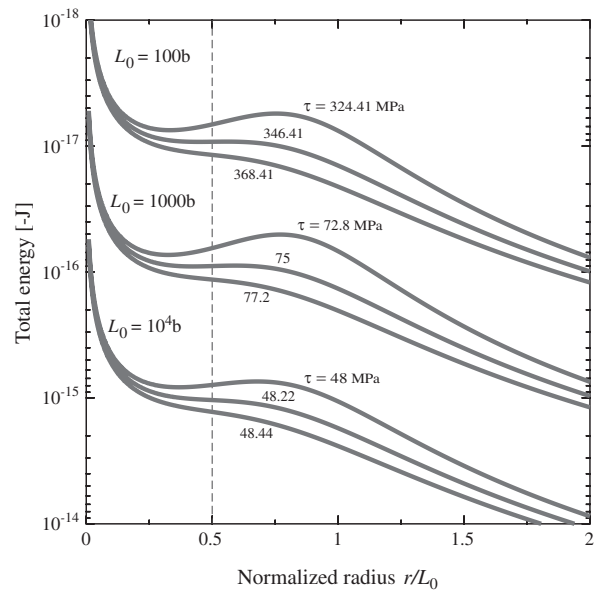


Fig. 3. Total energy (Q_{total}) of the twin nucleus. The numbers above each of the curves represent the applied shear stress. L_0 is the length of the sessile partial dislocations forming the twin nucleus and r is the distance the mobile partial dislocations have bowed out. An r/L_0 ratio of 0.5 is the critical ratio needed to be overcome in order for the twin to fully form. Less applied shear stress is required to form a twin as the size of the twin nucleus grows.

that the nucleation rate is an empirical function of strain. Allain et al. [39] link it directly to dislocation density, but an empirical constant of unknown value is included as a prefactor.

Here, we calculate the total number of potential twin nuclei based on the dislocation reaction which creates the nucleus. The number of active slip systems is a user-set parameter in the model. If the number of active systems is set to three, the probability that all three randomly chosen slip systems will all be non-coplanar is $54/110$. Hence, the probability for having two active slip systems which are coplanar, fulfilling a necessary criterion for the formation of the twin nucleus, is $1 - 54/110 = 56/110$. Dislocations can only form the twin nucleus in the given model when their interaction is repulsive, i.e. 50% of the time, so an extra factor of $1/2$ is included. The product of the statistical chance of forming a twin nucleus, the change in dislocation density due to dislocation multiplication accommodating the externally imposed strain rate and the reciprocal of the length of partial dislocations in one twin nucleus, $2/(3L_0)$, gives the number density of potential twin nuclei per unit time:

$$\dot{\theta} = \frac{56}{110} \frac{\dot{\varepsilon} M}{2} \frac{2}{3L_0} \rho = \frac{28}{165} \frac{\dot{\varepsilon} M}{L_0} [\rho_c f_c + (\rho_w + \rho_d) f_w] \quad (25)$$

The storage, or lifespan, of the twin nuclei is not taken into account because it is assumed that additional dislocation motion will destroy the nuclei created in the previous time step if they do not initially grow into twins.

In Mahajan and Chin's nucleation model, one bounding partial dislocation from each of two extended stacking faults on the same slip plane must come within a critical distance of one another, set as $x_c = 10 \text{ \AA}$ for the extreme case. The equilibrium separation of Shockley partials in fcc metals is calculated by [70]:

$$x_0 = \frac{Gb}{\gamma_{sf}} \frac{b}{24\pi} \frac{2+\nu}{1-\nu} \quad (26)$$

The repulsive force between the two partial dislocations is given by [29]:

$$F_r = \frac{Gb^2}{2\pi(x_0 + x_c)} + \frac{Gb^2 \cos(\pi/3)}{2\pi x_0} \quad (27)$$

Therefore, the stress needed to bring the two partials to within the critical distance to form the twin nucleus, x_c , without help from an external applied shear stress is:

$$\tau_r = F_r/b \quad (28)$$

In order for this stress to develop, a dislocation pile-up must occur to create a stress concentration. As the dislocations pile up, the partials could be forced to recombine into the full dislocation. If the dislocation is of a screw character, it could then cross-slip to another plane and alleviate some of the stress concentration caused by the dislocation pile-up. The probability that a cross-slip event will not occur, which would instead allow a sufficient number of dislocations to pile up and form the stress concentration necessary to form the twin nucleus, is given by:

$$p_{ncs} = 1 - \exp\left[-\frac{V}{kT}(\tau_r - \tau_{rss})\right] \quad (29)$$

where V is the cross-slip activation volume.

The probability that the triple layer stacking fault bows out to form a twin is:

$$p_{tw} = \exp\left[-\left(\frac{\tau_c}{\tau_{rss}}\right)^s\right] \quad (30)$$

where p_{tw} is the probability that the nucleation event occurs, τ_{rss} is the resolved shear stress, τ_c is shown in Eq. (24) and s is a fitted model parameter determining the sharpness of the transition from the non-twinning to twinning stress domain. It can be used to represent the effect that texture has on determining which grains twin.

The total twin nucleation rate is calculated by multiplying the total number density of potential twin nuclei per unit time by the probability that a sufficient stress concentration for the formation of the nucleus exists by the probability that one of those nuclei grows into a twin:

$$\dot{N} = \dot{\theta} p_{ncs} p_{tw} \quad (31)$$

As energy is always gained during twin growth, it is assumed that twins grow instantaneously until they encounter an obstacle, such as a grain boundary or a twin on a non-coplanar twin system. A new twin is considered to be disc-shaped, where the radial dimension is based on the twinning MFP. The twin volume is given by:

$$V_{tw} = \frac{\pi}{4} e t^2 \quad (32)$$

where t is the average twin spacing from Eq. (19) and e is the average twin width. It is a constant provided from experimental observations and is set to 30 nm. The twin volume fraction evolution is calculated by the product of the nucleation rate and the volume that a new twin occupies, and can occur only in the untwinned volume:

$$\dot{f}_{tw} = (1 - f_{tw}) \dot{N} V_{tw} \quad (33)$$

5.4. Temperature evolution

Until now, constitutive models of fcc metals have not considered temperature evolution, i.e. dissipative heating, during deformation. Experiments conducted by Chen et al. [71] suggest that the temperature of an Fe–18Mn–0.6C TWIP steel can rise by more than 110 K from the starting temperature when carrying out a test beginning at room temperature. In contrast to this observation, Xiong et al. [72] reported a maximum temperature increase of 55 K for a TWIP steel deformed at a high rate of 2400 s⁻¹.

This discrepancy in the experimentally observed dissipative temperature changes is not surprising, owing to the difficulty in controlling the boundary conditions during such infrared measurements. Typical error sources in such experiments are the reflection, surface and calibration conditions. Also, differences in the experimental set-up (e.g. sample dimensions and size; strain rate) as well as the heat capacity, localization behavior and heat conduction conditions through the grips can explain deviations among the experimental results [73].

We take this discrepancy in the reported experimental heating values as a motivation for including plastic dissipation in our current model. The goal is twofold: first, we aim at predicting dissipative heating in order to evaluate corresponding experiments. Secondly, because of the temperature dependence of the SFE, cross-slip and dislocation climb rates, this effect can no longer be ignored when predicting the mechanical behavior of such materials.

The change in temperature comes from work put into the sample minus the heat that is conducted away through the die:

$$\frac{dT}{dt} = \frac{\sigma_{ext} \dot{\epsilon}}{\rho_{Fe} C_p} f_D - \frac{2\alpha}{\rho_{Fe} C_p h} (T - T_0) \quad (34)$$

f_D is the dissipation coefficient, ρ_{Fe} is the density of iron, C_p is the ab initio-calculated temperature-dependent heat capacity for iron, α is the heat transfer coefficient, h is the height of the specimen (assuming a constant heat flux), T is the temperature and T_0 is the temperature of the die, which is considered to be a constant and is equal to the starting temperature of the test. Heat dissipation by air is not considered because the transfer of heat through air is much smaller than that through the die.

6. Results

In Fig. 3, the total twin nucleus energy Q_{total} is plotted against the normalized radius r/L_0 , where r is the distance representing how much the mobile Shockley partial dislocation has bowed out and L_0 represents the source length of the twin embryo (Fig. 1). The small numbers along each curve represent different values of applied shear stress. Each group of lines represents a different source length one order of magnitude apart. The size of the original nucleus is determined by L_0 .

After optimization, it was possible to fit the experimental data over a wide range of temperatures with a single parameter set. Table 1 presents the constants used in the model, Table 2 the optimized slip parameters and Table 3 the optimized twin parameters.

Fig. 4 shows the flow curves for seven temperatures; Fig. 5 shows the hardening curves corresponding to the stress–strain curves in Fig. 4.

The flow curves fit to the experimental data well for all temperatures. Upon inspection of the hardening curves, it is seen that the trends for each temperature are followed, and that reasonable agreement between simulation and experiment exists. Due to the significantly more difficult issue of correctly predicting hardening behavior, these fits are considered to be quite good and represent a step forward in the constitutive modeling of fcc materials with low SFE over a broad temperature range.

Because twin interfaces play such a large role in the hardening of TWIP steels, it was necessary to determine their volume fraction as accurately as possible. Quantifying deformation twins in high-Mn TWIP steels has been tried using several different methods, including EBSD [63,6] and EBSD in combination with X-ray diffraction (XRD) [62]. The twins themselves are often between 10 and

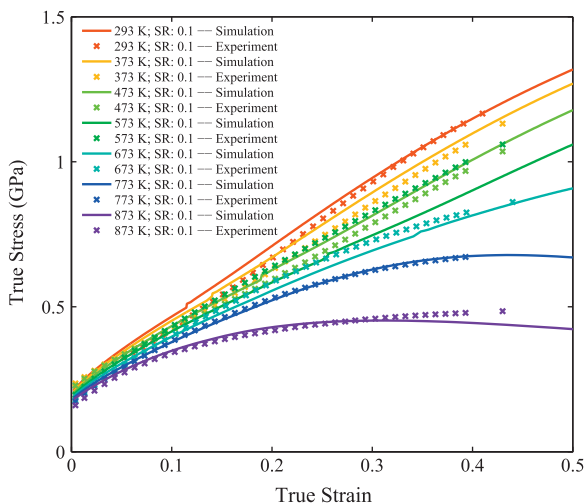


Fig. 4. True stress–true strain compression curves for Fe–22Mn–0.6C TWIP steel at seven different temperatures. One coherent parameter set was used for the whole temperature range. SR in the legend stands for “strain rate”.

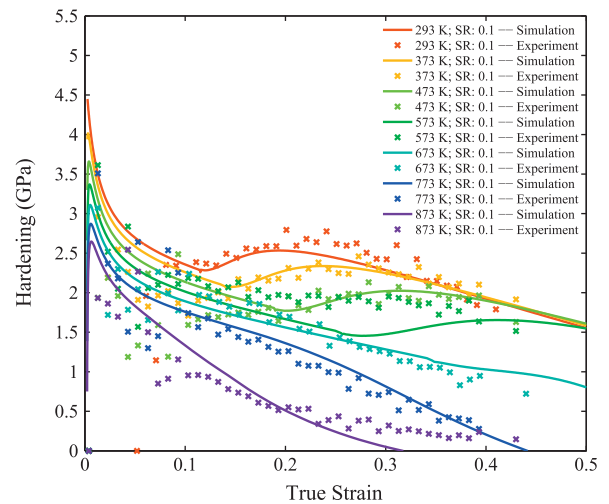


Fig. 5. Hardening curves corresponding to the true stress–true strain curves in Fig. 4 for Fe–22Mn–0.6C TWIP steel at seven different temperatures. One coherent parameter set was used for the whole temperature range.

30 nm thick, making individual twins nearly invisible to EBSD. They can be observed by TEM, but the viewable area is not as large as for other techniques and does not lead to good statistics. The challenge in XRD is to determine what exactly is a twin. It must be used in conjunction with EBSD to distinguish twins from grains in the same texture fiber. We decided to use ECCI [7,8,61,59,60], as outlined in Section 4.4.

Even if the observable area is significantly larger, it is still not an easy task to quantify the twin volume fraction: grains are heterogeneous, twins can start near the boundaries but stop in the middle of the grain, and the morphology looks quite different at high resolution and at the grain scale. The twins often form into twin bundles, which are visible at lower magnifications. High-magnification ECCI images were used to determine the average twin thickness, while ECCI images of entire grains were used to observe twin bundles and determine the twin volume fraction. The distances between twin bundles play a larger role in restricting the mean free path of dislocations than do the very small distances between individual twins in a bundle. Fifteen grains were investigated from each sample, five from each of three orientation groups: $\langle 111 \rangle$, $\langle 101 \rangle$ and $\langle 001 \rangle$. The twins were marked by hand with custom software in both the grain-level and high-resolution images. Grain boundaries were marked the same way, and the ratio of the twin bundle area to the grain area represents the twin volume fraction for each grain investigated. A numerical average of all grains represents the total twin volume fraction for the sample.

The twin volume fraction determined by ECCI is presented in Fig. 6, together with the twin volume fraction predicted by the simulation for three flow curves. The higher strain rate (10 s^{-1} as opposed to 0.1 s^{-1}) exhibits a marginally higher twin volume fraction in both the simulation and

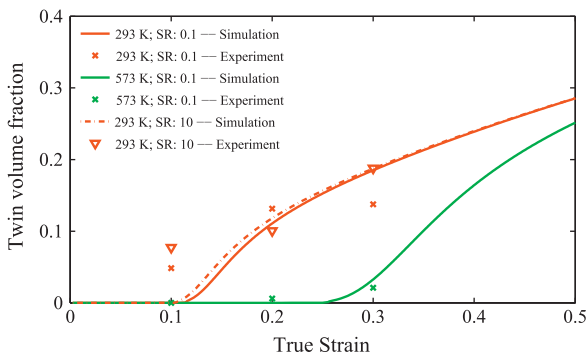


Fig. 6. Twin volume fraction obtained from the model and compared to experiments conducted by SEM-based ECCI.

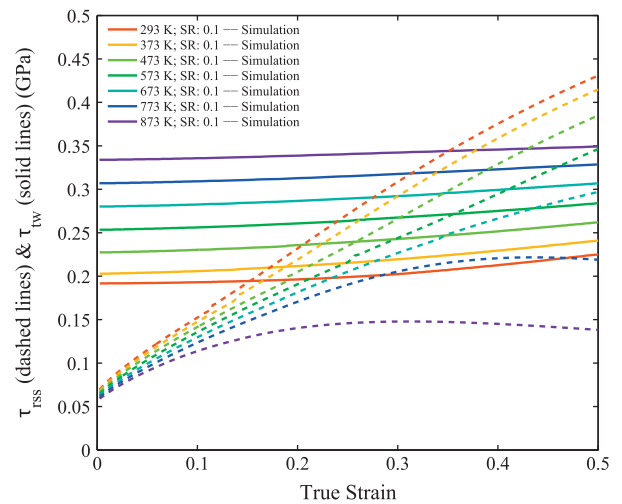


Fig. 8. Effective shear stress (dashed lines) and critical twinning stress (solid lines).

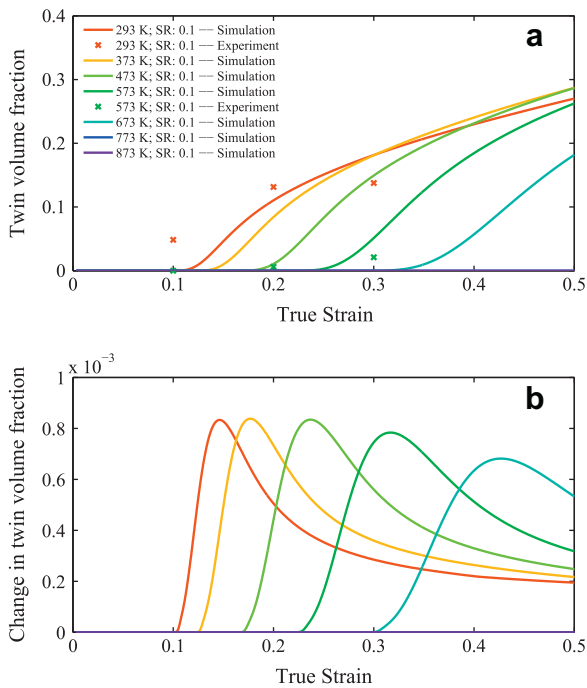


Fig. 7. Twin volume fraction (a) and the change in twin volume fraction (b) for seven temperatures. SR is the strain rate.

the experiments, but the difference was not significant. Temperature had the greatest effect on the twin volume fraction, with low levels of twinning observed at 573 K and levels between 5% and 20% at RT. A comparison of the predicted twin volume fraction for seven temperatures as well as the experimentally determined twin volume fraction for 293 K and 573 K is shown in Fig. 7a; the change in twin volume fraction is shown in Fig. 7b.

The resolved shear stress is shown compared to the critical stress for twinning in Fig. 8. Both sets of lines are simulated. It is clear that, with increasing temperature and SFE, the critical stress for twinning increases during deformation. The increases in temperature, SFE and critical twinning stress are directly compared in Fig. 9.

7. Discussion

The goal of this work was to develop a better understanding of the excellent strain-hardening behavior of high Mn-steels with medium to low SFE on the basis of the interaction of deformation twins and dislocations. More specifically, we are interested in the transition from conventional dislocation–dislocation-dominated hardening at low strains to the additional strain-hardening reserve due to dislocation–twin interaction observed at higher strains of TWIP steels. For this purpose, we developed here a physics-based model to ensure the use of realistic internal variables (dislocations, twins), their individual evolution equations, including twin nucleation, and their respective interactions. A further important aspect in our approach is the use of parameter ranges with physically justified upper and lower bounds.

Within this framework, we aim to reproduce and, hence, explain the origin of the secondary hardening increase of TWIP steels by using a single coherent input parameter set to appropriately predict its temperature and strain-rate dependence. The model can predict stress–strain and hardening behavior accurately. Because the hardening curve is a derivative, it is much more sensitive to mechanism changes than the flow curve. Additionally, good predictability of hardening behavior enables the delivery of information about the onset of necking using the Considère criterion. The strain-hardening rate is shown in Fig. 10, and it captures the sharp increase in hardening activity typical for this steel which has been shown in literature. Shiekhelsouk et al. [5] were not able to capture the decreasing behavior of the strain-hardening rate after the second increase, but Dancette [6] was able to do that for a simulation at room temperature. Here we were able to reproduce this trend for all temperatures. Each set of experimental data can be fitted almost perfectly with its own set of input parameters. In large-scale isothermal forming simulations, this

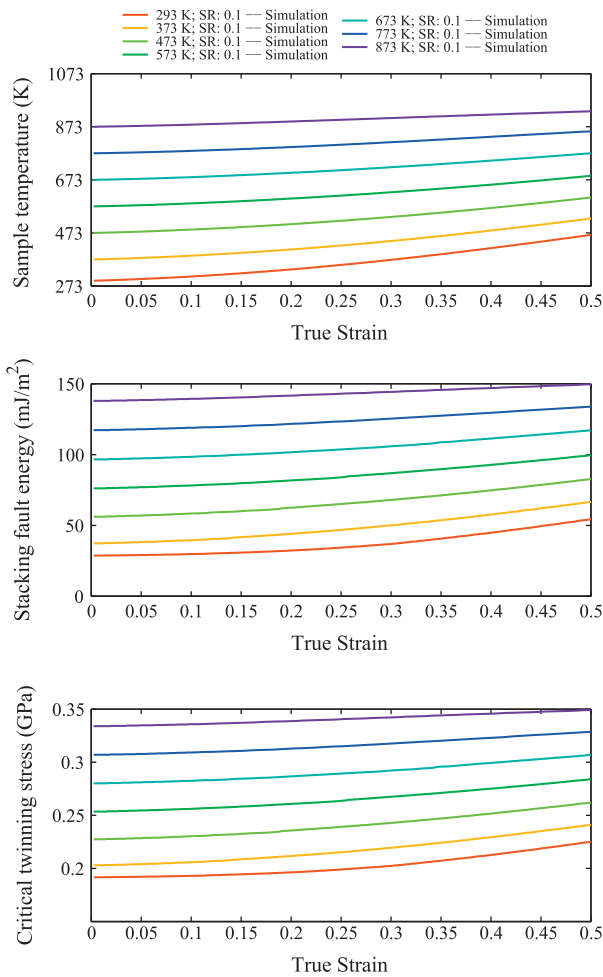


Fig. 9. Evolution of temperature, SFE and critical twinning stress at a strain rate of 0.1 s^{-1} .

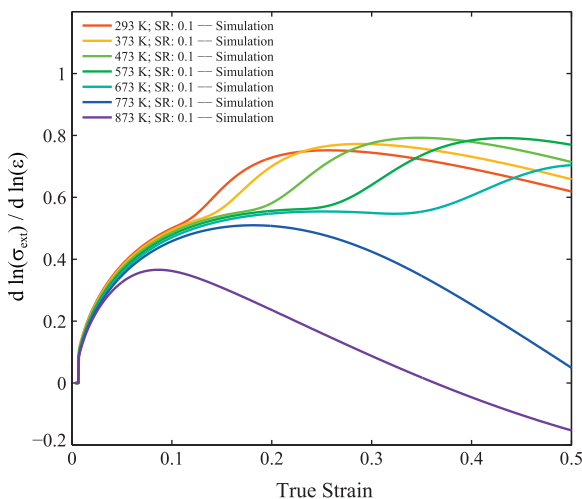


Fig. 10. Predicted strain-hardening rate. σ_{ext} refers to Eq. (15).

will produce accurate results. In simulations where the temperature and/or rate changes, a single coherent parameter set which describes material behavior over a wide range of temperatures is necessary. This is also important in

large-scale engineering and micromechanical finite element modeling [74–76] simulations in which local temperature deviations observed by infrared thermography are considered [73]. They can be in excess of 100 K as shear bands propagate through the material.

It is seen that both a critical amount of dislocation activity and a critical stress must be reached in order for twins to form. Fig. 7 shows that, once twinning is initiated, a sharp burst of twinning activity occurs, elevating the twin volume fraction quickly, after which a decrease in twinning activity occurs and a decaying twin production rate follows. Temperature clearly delays the onset of twinning by simultaneously decreasing the flow stress, increasing the rate of dislocation annihilation through climb and increasing the SFE, which in turn increases the critical stress needed to initiate deformation twinning. Temperature also spreads the burst of twinning over a larger strain range. The resolved shear stress is compared to the critical twinning stress in Fig. 8. At RT, the critical stress is breached by the resolved shear stress quite early in the flow curve, while at elevated temperatures the resolved shear stress never reaches the critical twinning stress.

The twin volume fraction predicted by the model fits well to that measured by experiment (Fig. 7). It is difficult to take measurements at strains higher than 0.3 because of the high level of deformation, so the large misorientation within a single grain prevents easy interpretation of the ECCI images. EBSD has a similar disadvantage at high deformations in that the indexing rate drops precipitously. While both experiments and the model show little twinning activity at 573 K up to 0.3 true strain, the model predicts a large increase after this. It also predicts twinning at 673 K at higher strains, which has been a temperature at which twinning was assumed to not occur. Despite these two inconsistencies, the stress-strain and hardening curves match the experimental ones very well over the whole temperature range.

From the new constitutive model, and particularly from the twin nucleation part of the model, we learn that the proper design of an SFE determines the activation stress for twin nucleation. Properly designing the SFE of the austenite as a “resistance parameter” acting against deformation twinning is essential here because, in conventional steel concepts containing unstable austenite, the resulting twinning (or martensite formation mechanisms) and the associated strain-hardening response via TWIP/TRIP often occurs at low strains, where additional hardening is usually not desired. In contrast to that, our model reveals that the design strategy in the current case should be to optimize austenite stability/SFE in such a way that twinning is activated at higher strains, where the dislocation–dislocation hardening gradually becomes exhausted. The calculated SFE can be seen in the center of Fig. 9. It increases with increasing strain due to the increase in temperature seen at the top of Fig. 9. This design principle has also been pointed out before for the case of austenitic stainless and duplex steels, where the austenite metastability must be adjusted by composition

with the aim of avoiding premature strain-induced martensite formation at too low strains [77,78].

It should be noted in that context that the dissipative heating predicted for a tensile test that starts at RT amounts to about 200 K. This value exceeds the experimental observations of Xiong et al. [72], who reported a value of 55 K for such steels, and Chen et al. [71], who reported a value of 110 K. As discussed above, we attribute this deviation between the theoretical prediction and the experiments to the difficulty in controlling the boundary conditions when taking the infrared measurements [73]. We assume that the increase in temperature during deformation predicted here is realistic since the simulation does not include any complex model assumptions or fitting parameters. This means that the deformation work is translated into dissipative heat minus the loss expressed by the relation between heat conduction and heat capacity times density (see Section 5.4).

Fe–22Mn–0.6C is both a substitutional solid solution of Fe and Mn and an interstitial solid solution of Fe and C. The effect of temperature on solid solution hardening is not explicitly considered in the model formulation, but enters through fitted values of the activation energy of the cutting process in slip and the activation energy for climb (Table 2). Including a tailored solution-hardening component would aid in extending the model to cover other compositions or material systems.

It has been suggested that the source length, L_0 , should be related to the forest dislocation density [79]. Likewise, it could be related to the MFP. In this case, it was chosen to be a constant which does not change with the evolution of the microstructure. Thornton and Mitchell [80] state that, for the Suzuki model [81], L_0 should be between 250 and 500 multiples of the Burgers vector, and for Venables's model [47] it should be between 100 and 250 multiples of the Burgers vector. These are reasonable values, and the bounds of L_0 were set to be 50–1500 multiples of the Burgers vector, with the optimized value at 261 nm, or 1020*b*, slightly more than twice the upper limit of that predicted by Suzuki's model.

The slip strength model parameters p and q describe the slip obstacle profile. by Kocks et al. [66], their bounds should be $0 < p \leq 1$ and $1 \leq q \leq 2$. As was noted: "The possible range of values for p and q is limited by the requirement that the activation area increases continuously as σ decreases". The optimized slip parameters are both equal to 1 (see Table 2), indicating an average box obstacle profile. This may be due to the complex interaction of the differing strengths of forest dislocations, dislocation cell walls, twin boundaries and grain boundaries as obstacles to slip; solution hardening from the substitutional Mn atoms and interstitial C atoms; and the use of singular p and q values to describe the slip behavior in both the dislocation cell walls and the cell interior.

The fitted model parameter s controls the abruptness of the transition from the non-twinning regime to the twinning regime as a function of stress. A small value of s rep-

resents a wide transition and indicates a variation in the effect the resolved shear stress has on the nucleation and growth of new twins as it nears the critical twinning stress. Because this model does not consider individual grains and a single Taylor factor is used instead of a distribution of maximum Schmid factors to convert the external stress into a resolved shear stress, s may be used to create a profile which is consistent with the fraction of grains which have reached the critical twinning stress on a twinning system at differing orientations. This variable could provide a method to tailor the nucleation rate of twins near the transition point if the texture of an experimental sample is known. The optimized value was 13.6, indicating a sharp transition into the twinning regime.

A weight, i_{tw} , is included in the calculation of the MFP. Physically it represents the average of the number of twin spacings that a dislocation travels before being stored. It acts in conjunction with its corresponding dislocation contributions, i_c and i_w , to determine how much of a contribution twinning makes to the MFP. Therefore, it is called the twin contribution factor. The optimized value was 5.52, which is very close to that for i_c and i_w at 5.43. A larger number implies a weaker influence of the twins on the MFP, implying that twins are weaker obstacles to dislocation motion than grain boundaries, which is an idea supported in the literature [4] and by the fact that the grain boundary contribution factor is 1.

The meaningful bounds of the twin parameters have already been discussed above. Now the bounds of the slip parameters will be inspected. In Eqs. (6)–(8), d_a is the maximum slip plane separation that two dislocations of opposite sign must achieve in order to spontaneously annihilate. Its upper bound is 20 times the Burgers vector. Three more parameters in Eq. (9) are D_0 , Q_c and Ω . Q_c is the activation energy of climb. This should be near the activation energy for self-diffusion, which for γ -Fe is 2.8 eV [70]. The bounds were thus set to 2.8 ± 0.5 eV. The optimized value turned out to be slightly less than for γ -Fe at 2.33 eV. Ω is the activation volume for climb, which is $1.5b^3$. In Eq. (11), α is the passing coefficient for shear, which considers the arrangement of dislocations. This has been shown to be a value on the order of unity. The bounds on solution hardening, τ_0 in Eq. (11), as a fitting parameter were 0–150 MPa. While 150 MPa may seem high, it is well known that C interstitials have a very strong hardening effect in Fe. In addition, there is a high content of substitutional Mn, the impact of which can produce further hardening not only on the Fe matrix, but also in forming couples with the interstitial C [19,82,83]. Lastly, $i_{c,w}$ represents the average number of dislocation spacings that dislocations travel before becoming sessile. This value is considered to be between 1 and 100.

8. Conclusions

A new physics-based constitutive model for low-SFE fcc metals that exhibit deformation twinning has been

developed based on a combination and extension of the 3IVM of Roters et al. [64] and the twin nucleation model of Mahajan and Chin [29]. Dislocation cells, grain size and twin volume fraction evolution are included.

Very good agreement with experimental compression data (Fe–22Mn–0.6C TWIP steel) was found between 293 and 873 K using a single set of physically motivated parameters. The model reveals that the intermediate strain-hardening regime that is responsible for the high formability of TWIP steels is due to the dynamic increase of the twin-related interface density and its interaction with the dislocations. In addition, due to the good prediction of hardening behavior over a temperature range spanning almost 600 K, the door is now open to the inclusion of adiabatic heating effects caused by shear banding, the implementation of temperature-sensitive forming simulations and the improvement of failure simulations.

The twin nucleation model introduced follows twinning at the mechanistic level and considers both the dislocation activity necessary to create twin nuclei and the stress state responsible for the expansion of the nuclei into twins. The nucleation rate of twins is linked directly to the dislocation density, the size of the twin nucleus and the SFE through the critical twin stress and the probability of formation of the twin nucleus.

The simulated temperature of the sample evolves during deformation owing to dissipation, a phenomenon that has been ignored in models until now, but is vital to include. The predicted changes in sample temperature during RT compression or tensile testing can exceed 100 K in the case studied here.

The SFE of an alloy, which is the key parameter for twinning, can nowadays be calculated ab initio by density functional theory. In combination with the presented model, it is therefore possible to tailor the SFE (i.e. the alloy composition) to achieve desired macroscopic properties. This is a big step forward in predictive hierarchical materials modeling.

Acknowledgements

The authors gratefully acknowledge the financial support of the Deutsche Forschungsgemeinschaft (DFG) within the Collaborative Research Center (SFB) 761 “Steel–ab initio”. The authors would also like to give special thanks to Luc Hantcherli for his help with some of the figures.

References

- [1] Allain S, Chateau JP, Bouaziz O. *Mat Sci Eng A* 2004;387:143.
- [2] Barbier D, Favier V, Bolle B. *Mat Sci Eng A* 2012;540:212.
- [3] Bouaziz O, Guelton N. *Mat Sci Eng A* 2001;319:246.
- [4] Karaman I, Sehitoglu H, Beaudoin AJ, Chumlyakov YI, Maier HJ, Tome CN. *Acta Mat* 2000;48(9):2031.
- [5] Shiekhelsouk MN, Favier V, Inal K, Cherkaoui M. *Int J Plast* 2009;25(1):105.
- [6] Dancette S, Delannay L, Renard K, Melchior MA, Jacques PJ. *Acta Mat* 2012;60(5):2135.
- [7] Gutierrez-Urrutia I, Zaefferer S, Raabe D. *Scripta Mat* 2009;61(7):737.
- [8] Gutierrez-Urrutia I, Raabe D. *Acta Mat* 2011;59(16):6449.
- [9] Gutierrez-Urrutia I, Raabe D. *Acta Mat* 2012;60:5791.
- [10] Grabowski B, Hickel T, Neugebauer J. *Phys Rev B* 2007;76:024309.
- [11] Friak M, Hickel T, Körmann F, Udyansky FA, Dick A, von Pezold J, et al. *Steel Res* 2011;82:86.
- [12] Reeh S, Music, Gebhardt DT, Kasprzak M, Jäpel T, Zaefferer S, et al. *Acta Mat* 2012;60(17):6025–32.
- [13] Saeed-Akbari A, Schwedt A, Bleck W. *Scripta Mater* 2012;66:1024.
- [14] Ma A, Roters F. *Acta Mat* 2004;52(12):3603.
- [15] Ma A, Roters F, Raabe D. *Acta Mat* 2006;54(8):2169.
- [16] Adler P, Olson G, Owen W. *Met Mat Trans A* 1986;17(10):1725.
- [17] Asgari S, Eldanaf E, Kalidindi SR, Doherty RD. *Met Mat Trans A* 1997;28(9):1781.
- [18] El-Danaf E, Kalidindi SR, Doherty RD. *Int J Plast* 2001;17(9):1245.
- [19] Hutchinson B, Ridley N. *Scripta Mat* 2006;55(4):299.
- [20] Jin JE, Lee YK. *Mat Sci Eng A* 2009;527(1-2):157.
- [21] Kalidindi SR. *Int J Plast* 2001;17(6):837.
- [22] Kocks UF. *Phil Mag* 1966;13(123):541.
- [23] Nes E. *Prog Mat Sci* 1997;41(3):129.
- [24] Sevillano JG. *Scripta Mat* 2009;60(5):336.
- [25] Rémy L. *Met Trans A* 1981;12(3):387.
- [26] Venables JA. *Deformation twinning*. New York: Gordon & Breach; 1964.
- [27] Friedel J. *Dislocations*. Oxford: Pergamon Press; 1965.
- [28] Mahajan S. *Phil Mag* 1971;23(184):781.
- [29] Mahajan S, Chin GY. *Acta Metal* 1973;21(10):1353.
- [30] Gutierrez-Urrutia I, Zaefferer S, Raabe D. *Mat Sci Eng A* 2010;527(15):3552.
- [31] Gutierrez-Urrutia I, Raabe D. *Scripta Mat* 2012;66:992.
- [32] Rémy L. *Acta Metal* 1978;26:443.
- [33] Christian JW, Mahajan S. *Prog Mat Sci* 1995;39(1–2):1.
- [34] Kalidindi SR. *J Mech Phys Sol* 1998;46(2):267.
- [35] Kalidindi SR. *Int J Plast* 1998;14(12):1265.
- [36] Jia N, Roters F, Eisenlohr P, Kords C, Raabe D. *Acta Mat* 2012;60:1099.
- [37] Jia N, Eisenlohr Pand Roters F, Raabe D. *Acta Mat* 2012;60:3415.
- [38] Tomé CN, Lebensohn RA, Kocks UF. *Acta Metal Mat* 1991;39(11):2667.
- [39] Allain S, Chateau JP, Bouaziz O. *Steel Res* 2002;73(6-7):299.
- [40] Cherkaoui M. *Phil Mag* 2003;83(31–34):3945.
- [41] Bouaziz O, Allain S, Scott C. *Scripta Mat* 2008;58(6):484.
- [42] Mingxin H, Bouaziz O, Barbier D, Allain S. *J Mat Sci* 2011;46(23):7410.
- [43] Rémy L. *Acta Metal* 1977;25(2):173.
- [44] Mahajan S, Barry DE, Eyre BL. *Phil Mag* 1970;21(169):43.
- [45] Kim J, Estrin Y, Beladi H, Timokhina I, Chin KG, Kim SK, et al. *Met Mat Trans A* 2012;43A(2):479.
- [46] Cottrell AH, Bilby BA. *Phil Mag* 1951;42(329):573.
- [47] Venables JA. *Phil Mag* 1961;6(63):379.
- [48] Blewitt TH, Coltman RR, Redman JK. *J Appl Phys* 1957;28(6):651.
- [49] Seeger A. *Z Metallkunde* 1956;47(9):653.
- [50] Cohen JB, Weertman J. *Acta Metal* 1963;11(8):996.
- [51] Cohen JB, Weertman J. *Acta Metal* 1963;11(8):1368.
- [52] Fujita H, Mori T. *Scripta Metal* 1975;9(6):631.
- [53] Miura S, Takamura JI, Narita N. *Trans Jpn Inst Metals* 1968;9:555.
- [54] Kibey S, Liu JB, Johnson DD, Sehitoglu H. *Acta Mat* 2007;55(20):6843.
- [55] Kibey SA, Wang LL, Liu JB, Johnson HT, Sehitoglu H, Johnson DD. *Phys Rev B* 2009;79(21):214202.
- [56] Bracke L, Kestens L, Penning J. *Scripta Mat* 2009;61(2):220.
- [57] Idrissi H, Renard K, Ryelandt L, Schryvers D, Jacques PJ. *Acta Mat* 2010;58(7):2464.
- [58] Wietbrock B, Xiong W, Bambach M, Hirt G. *Steel Res Int* 2011;82(1):63.
- [59] Wilkinson AJ, Anstis GR, Czernuszka JT, Long NJ, Hirsch PB. *Phil Mag A* 1993;68(1):59.

- [60] Wilkinson AJ, Hirsch PB. *Micron* 1997;28(4):279.
- [61] Gutierrez-Urrutia I, Raabe D. *Scripta Mat* 2012;66(6):343.
- [62] Barbier D, Gey N, Allain S, Bozzolo N, Humbert M. *Mat Sci Eng A* 2009;500(1–2):196.
- [63] Renard K, Jacques PJ. *Mat Sci Eng A* 2012;542:8.
- [64] Roters F, Raabe D, Gottstein G. *Acta Mat* 2000;48(17):4181.
- [65] Mecking H, Kocks UF. *Acta Metal* 1981;29(11):1865.
- [66] Kocks UF, Argon AS, Ashby MF. *Prog Mat Sci* 1975;19:1.
- [67] Estrin Y, Mecking H. *Acta Metal* 1984;32(1):57.
- [68] Fullman RL. *Trans AIME*. 1953.
- [69] Saeed-Akbari A, Mosecker L, Schwedt A, Bleck W. *Metall Mater Trans A* 2012;43:1688.
- [70] Gottstein G. *Physical Foundations of Materials Science*. Berlin, Heidelberg: Springer; 2004.
- [71] Chen L, Kim HS, Kim SK, De Cooman BC. *ISIJ Int* 2007;47(12):1804.
- [72] Xiong ZP, Ren XP, Bao WP, Li SX, Qu HT. *Mat Sci Eng A* 2011;530(0):426.
- [73] Eisenlohr A, Gutierrez-Urrutia I, Raabe D. *Acta Mat* 2012;60:3994.
- [74] Zhao Z, Roters F, Mao W, Raabe D. *Adv Eng Mater* 2001;3:984.
- [75] Raabe D, Klose P, Engl B. *Adv Engin Mater* 2002;4:169.
- [76] Roters F, Eisenlohr P, Hantcherli L, Tjahjanto DD, Bieler TR, Raabe D. *Acta Mat* 2010;58(4):1152.
- [77] Misra RDK, Zhang Z, Venkatasurya PKC, Somani MC, Karjalainen LP. *Mat Sci Eng A* 2011;528(3):1889.
- [78] Herrera C, Ponge D, Raabe D. *Acta Mat* 2011;59:4653.
- [79] Karaman I, Sehitoglu H, Gall K, Chumlyakov YI, Maier HJ. *Acta Mat* 2000;48(6):1345.
- [80] Thornton PR, Mitchell TE. *Phil Mag* 1962;7(75):361.
- [81] Suzuki H, Barrett CS. *Acta Metal* 1958;6(3):156.
- [82] Dastur YN, Leslie WC. *Met Trans A* 1981;12(5):749.
- [83] Owen WS, Grujicic M. *Acta Mat* 1998;47(1):111.

Dislocation density measurement by electron channeling contrast imaging in a scanning electron microscope

I. Gutierrez-Urrutia* and D. Raabe

Max-Planck-Institut für Eisenforschung, Max-Planck Str. 1, D-40237 Düsseldorf, Germany

Received 12 October 2011; revised 18 November 2011; accepted 19 November 2011
Available online 30 November 2011

We have measured the average dislocation density by electron channeling contrast imaging (ECCI) in a scanning electron microscope under controlled diffraction conditions in a Fe–3 wt.% Si alloy tensile deformed to a macroscopic stress of 500 MPa. Under optimal diffraction conditions, ECCI provides an average dislocation density close to that obtained by bright-field transmission electron microscopy. This result confirms that ECCI is a powerful technique for determining dislocation densities in deformed bulk metals.

© 2011 Acta Materialia Inc. Published by Elsevier Ltd. All rights reserved.

Keywords: Dislocations; Low-temperature deformation; Electron diffraction; Scanning electron microscopy (SEM); Ferritic steels

The storage of dislocations during deformation of metals plays a key role in most metallurgical phenomena such as strain hardening, damage, creep, fatigue, athermal phase transformations, recrystallization and strain-induced grain boundary migration. In the former cases, it determines the mechanical properties such as strength and ductility. In the latter cases, it plays an important role in the mechanisms acting during annealing and transformation of deformed microstructures. In many cases, the average dislocation density is even linearly related to characteristic phenomena such as strengthening, creep rate, recovery and primary recrystallization. For this reason, the determination of the average dislocation density is important to better understand such phenomena. Dislocation density is commonly measured by direct methods such as transmission electron microscopy (TEM) [1–3] and indirect methods such as X-ray diffraction (XRD) [4,5]. TEM provides a highly accurate determination of the dislocation density provided that the dislocations can be clearly distinguished, i.e. it can be applied with high accuracy below a certain dislocation density ($\sim 5\text{--}10 \times 10^{-14} \text{ m}^{-2}$). However, the determination of average dislocation density values in heterogeneous microstructures by TEM is time consuming owing to the demanding sample preparation technique involved. On the other hand, XRD provides an average

dislocation density of the bulk deformed material in a shorter time but with a limited spatial resolution. In addition, XRD analysis of defect structures requires the use of a well-justified underlying model that connects a certain dislocation density and distribution with a total displacement gradient field.

An alternative microscopy technique for characterizing deformed microstructures is electron channeling contrast imaging (ECCI) [6–9]. ECCI is a scanning electron microscopy (SEM) technique that makes use of the fact that the backscattered electron intensity is strongly dependent on the orientation of the crystal lattice planes with respect to the incident electron beam due to the electron channeling mechanism. Slight local distortions in the crystal lattice due to dislocations cause a modulation of the backscattered electron intensity, allowing the defect to be imaged. The ECCI technique has been used to image dislocation structures in metals deformed during fatigue loading [10] or in the vicinity of cracks [11], and even stacking faults [12]. In particular, we have recently characterized complex mixed dislocation and twin substructures, as well as their individual contributions to strain hardening, on a highly deformed Fe–22 wt.% Mn–0.6 wt.% C alloy [13,14] by ECCI. For this purpose we used a novel ECCI set-up [9] which makes use of combined electron backscatter diffraction (EBSD) to image dislocations at enhanced contrast. In this paper, we demonstrate that the ECCI technique allows the determination of the average dislocation density of a deformed metal. The aim of the work is to establish ECCI

* Corresponding author. Tel.: +49 2116792 407; e-mail: i.gutierrez@mpie.de

as a very powerful, versatile, fast and experimentally robust method for determining dislocation defects densities and arrangements that involves a relatively simple preparation process. For this reason we used ECCI to measure the average dislocation density in a Fe–3 wt.% Si alloy tensile deformed to a macroscopic stress of 500 MPa. Under optimal diffraction conditions, the ECCI technique provides an average dislocation density close to that obtained by bright-field TEM.

The material selected was a Fe–3 wt.% Si alloy sheet 260 μm thick supplied by ThyssenKrupp Electrical Steel GmbH. The material has a large grain size in the centimeter range and a strong Goss texture $\{110\}\langle 001\rangle$. This microstructure makes the sample suited for the measurement of the dislocation density. Tensile tests were performed at room temperature at a strain rate of $2 \times 10^{-3} \text{ s}^{-1}$ to a macroscopic stress of 500 MPa. The mechanical tests were carried out using test instrument of Kammrath & Weiss GmbH (44141 Dortmund, Germany) equipped with a digital image correlation (DIC) system (ARAMIS system, GOM-Gesellschaft für Optische Messtechnik mbH, 38106 Braunschweig, Germany) for measuring the local strain. Details of this set-up are described in Ref. [15]. The surface pattern required for DIC was obtained as explained in Ref. [13]. Dislocation densities were measured in areas with a local strain of 0.05 by means of ECCI. A new recently reported set-up for ECCI [9] was used in this study to obtain ECCI images under controlled diffraction conditions which produced an enhanced dislocation contrast. This ECCI set-up has been successfully used in the imaging of dislocation substructures in Fe-based alloys [13,14]. The set-up uses EBSD patterns for calculating the optimal orientation of the crystal inspected through a specific combination of tilts and rotations. These are determined from the corresponding calculated diffraction pattern using the algorithm developed in Ref. [16]. ECCI observations were carried out in a Zeiss Crossbeam instrument (XB 1540, Carl Zeiss SMT AG, Germany) consisting of a Gemini-type field emission gun (FEG) electron column and a focused ion beam (FIB) device (Orsay Physics). ECCI was performed at 10 kV acceleration voltage and a working distance of 6 mm, using a solid-state four-quadrant backscattered electron detector. ECCI images were obtained with the sample normal aligned parallel to the incident electron beam.

It is well known that optimum dislocation contrast in ECCI is obtained by orienting the crystal to the exact Bragg angle, i.e. $s = 0$ where s is the deviation vector, in a two-beam condition [8,17]. Dislocation contrast becomes weaker under diffraction conditions deviating from the optimal, i.e. when $s \neq 0$. However, the latter, although not optimal, can be useful in the determination of the average dislocation density, as we show below. In the present work, we have evaluated the influence of diffraction condition in the determination of the average dislocation density. Dislocation densities were determined from ECC images that were taken under two different diffraction conditions, namely two-beam conditions with one set of hkl planes at the Bragg angle, and, alternatively, three-beam cases with two sets of hkl planes in an out-of-Bragg condition. For the first diffraction condition, dislocations appear as sharp bright lines

over a dark background, whereas in the second diffraction condition, dislocations are visible as bright and dark sharp lines over a brighter background.

Figure 1 shows examples of ECC images of dislocation arrangements at the same area under different diffraction conditions with the corresponding calculated diffraction patterns. The ECC image of Figure 1a was obtained after orienting the crystal into Bragg condition using a high-intensity reflection of (110)-type. The calculated diffraction pattern is shown in Figure 1b. Under this diffraction condition, the crystal matrix appears dark and dislocations appear as sharp bright lines. The ECC image presented in Figure 1c was obtained after orienting the crystal out of the Bragg condition with $s < 0$. The calculated diffraction pattern is shown in Figure 1d. In this orientation, the crystal matrix appears brighter than in Bragg condition due to electron channeling mechanism [8]. In the first case, electrons are more effectively channeled into the lattice and the backscattering yield is low, leading to a dark appearance of the crystal. In the second case, the backscattering yield is enhanced and the crystal appears bright. In Figure 1c, we can identify dislocations appearing as white and black lines with uniform and sharp contrast. According to the dislocation contrast theory developed for TEM, the dislocation contrast exhibits an oscillatory black–white color with a periodicity of ξ_g , where ξ_g is the extinction distance [3]. Spencer et al. [17] showed that in ECCI, similar to TEM, the oscillatory behavior disappears for a dislocation that is located deeper than $2\xi_g$ from the sample surface, due to anomalous absorption phenomena related with inelastic scattering processes. According to the dislocation contrast profiles calculated by the authors [11], in a two-beam condition with one set of hkl planes at or close to Bragg orientation, dislocations exhibit a uniform white contrast. As in ECCI the $g \cdot b = 0$ invisibility criterion holds [8,18,19], we can ascribe the bright sharp dislocations to those fulfilling $g \cdot b \neq 0$ with g : 110, where b is the Burgers vector and g the diffraction vector. The origin of the

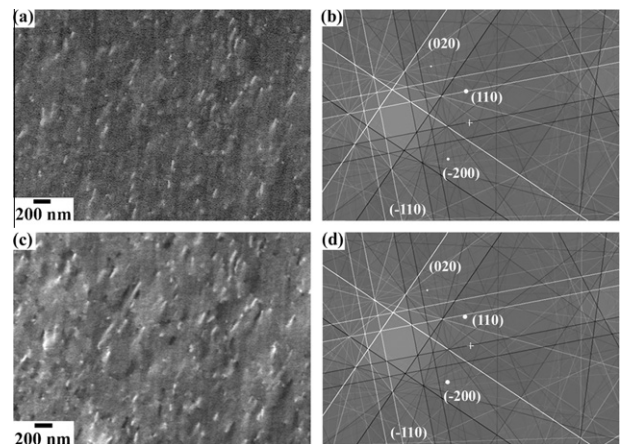


Figure 1. ECC images of dislocation arrangements of the same area in a Fe–3 wt.% Si alloy tensile deformed to a macroscopic stress of 500 MPa under two different diffraction conditions with the corresponding calculated diffraction pattern: (a and b) two-beam condition with g : 110 at Bragg orientation; (c and d) three-beam condition with g : 110 and g : -200 out-of-Bragg (g is the diffraction vector).

sharp black dislocation contrast observed in Figure 1c can be attributed to the deviation from the two-beam condition. As the calculated diffraction pattern of Figure 1d reveals, the (-200) reflector, which is out of Bragg condition with $s \ll 0$, is excited as well, although it is less strong than $g: 110$, i.e. it corresponds to a three-beam condition. Accordingly, these dislocations fulfill $g \cdot b \neq 0$ with $g: -200$ and, due to $s \ll 0$, exhibit a black contrast. In fact, this is the origin of the diffuse black dislocation contrast in the ECC image revealed in Figure 1a, as the calculated diffraction pattern of Figure 1b shows. Under the present microscope conditions with an acceleration voltage of 10 kV, anomalous absorption occurs at depths higher than about $2\xi_{200} \approx 26$ nm for the diffraction conditions used here. As most of the visible dislocations exhibit a uniform contrast, this indicates that dislocations visible by ECCI in the present study are placed deeper than 26 nm from the sample surface.

Average dislocation densities, ρ , were estimated using the relationship: $\rho = 2N/Lt$, where N is the number of dislocation lines intersecting a grid of total line length L on the corresponding ECC image and t is the probe depth. This is a standard relationship used in TEM when the individual dislocations can be clearly distinguished, like in the present study [1,20]. Dislocations were measured from ECC images similar to those shown in Figure 1. As example, Figure 2 depicts a drawing of the dislocations (black lines) imaged under the diffraction conditions of Figure 1a and c. Dislocations are identified according to the dislocation contrast of the corresponding diffraction condition, namely bright lines in Figure 1a and bright and dark lines in Figure 1c. Only dislocations with a well-defined and sharp contrast are considered. Figure 1c reveals that some dislocations with black contrast exhibit a blurred contrast, which is mainly ascribed to the multi-beam diffraction condition with $s < 0$. However, these dislocations can also be clearly identified. It can be seen

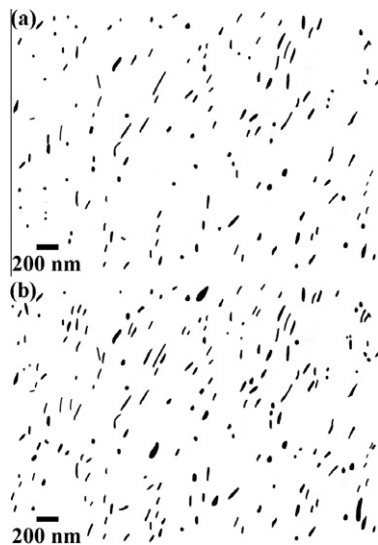


Figure 2. Schematic drawings of the dislocations (black lines) imaged by ECCI as shown in Figure 1: (a) corresponds to Figure 1a, (b) corresponds to Figure 1c. See the text for details of the identification procedure.

that the number of dislocations identified in Figure 2b is higher than in Figure 2a. This is ascribed to the higher number of excited reflectors which provides two types of dislocation contrast, i.e. black and white. The probe depth for imaging dislocations in ECCI is a difficult parameter to calculate due to the complexity of modeling the backscattering of electrons from a thick crystalline material. However, Wilkinson et al. [7] have calculated ECC image profiles of dislocations based on the theoretical approach of channeling contrast formation suggested by Spencer et al. [17], and estimated the limiting probe depth for imaging dislocations in ECCI, which is about $5\xi_g$. Assuming this probe depth and under the present ECCI conditions (acceleration voltage of 10 kV, and corresponding values of ξ_g for Fe [21]), the probe depth ranges from 45 to 65 nm for the diffraction vectors g used in the present study ((110) and (200) -type). The estimated average dislocation densities are plotted in Figure 3. Under three-beam conditions, the largest probe depth was used. Average dislocation densities of $10 \pm 4 \times 10^{-13}$ and $17 \pm 6 \times 10^{-13} \text{ m}^{-2}$ were obtained from the ECC images under two-beam conditions with one set of hkl planes at Bragg orientation and three-beam conditions with two sets of hkl planes out-of-Bragg, respectively. We should emphasize here that the multi-beam conditions used to estimate the average dislocation density are similar to those shown in Figure 1c and d. As Figure 1 reveals, the higher average density obtained by the second diffraction condition is ascribed to the higher number of excited reflectors, which provides, due to channeling mechanism, a higher amount of visible dislocations.

To compare the present estimations of the average dislocation density measured by ECCI to that determined by a standard characterization technique such as TEM, we have included in Figure 3 the average dislocation density measured in a Fe–3 wt.% Si sample deformed to the same macroscopic stress level (500 MPa) by bright-field TEM. The average dislocation density was measured from TEM micrographs using the same method as in the present work [22]. It can be seen that the average dislocation density estimated from ECCI is in the same range than that determined from bright-field

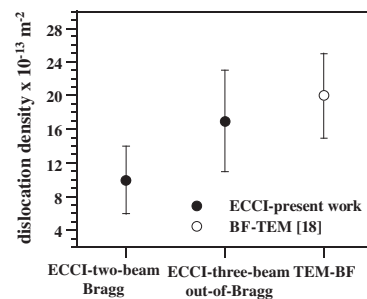


Figure 3. Average dislocation densities determined in a Fe–3 wt.% Si alloy tensile deformed to a macroscopic stress of 500 MPa by two different electron microscopy techniques: ECCI and TEM. Average dislocation densities were measured by ECCI under two different diffraction conditions: two-beam conditions with one set of hkl planes in the Bragg orientation (Fig. 1a and b) and three-beam diffraction conditions with two sets of hkl planes out-of-Bragg (Fig. 1c and d) (BF: bright field).

TEM. In particular, the average dislocation density measured by ECCI in two-beam conditions with one set of hkl planes at the Bragg orientation represents a lower-bound value for the dislocation density. This result is well-known from corresponding TEM-based estimates [1]. The present work shows that three-beam diffraction conditions with two sets of hkl planes out-of-Bragg provide a better estimation of the average dislocation density by ECCI, close to that obtained by bright-field TEM. Further, this study confirms ECCI as a powerful technique to determine dislocation densities in deformed bulk metals at a wide field of view. This is a significant advance in microstructural characterization of deformed materials where dislocation densities are typically determined by TEM or XRD. As ECCI is a SEM-based technique it has the advantage over TEM that much larger areas can be observed and samples are easier to prepare. However, due to the small size of the features imaged in this study, namely dislocation lines, the determination of dislocation densities is here performed on areas comparable to those used in TEM. Furthermore, in TEM, the wedge-shape geometry of the foil also makes it necessary to measure the sample thickness in each analyzed material portion. In ECCI, the probe depth only depends on the acceleration voltage and diffraction vector through the extinction distance. In particular, in an oxide-free surface and operating at constant acceleration voltage, the probe depth is only determined by the diffraction vector. It is worth mentioning that in the present ECCI–EBSD approach dislocations are imaged in the scanning electron microscope directly from the collected electron backscattered signal. Accordingly, the estimated dislocation density comprises both types of dislocations, namely geometrically necessary dislocations (GND) and statistically stored dislocations (SSD). Recently, there is an increasing interest in the determination of the GND density via EBSD-based approaches. These methods are based on the measurement of orientation gradients by electron backscatter diffraction patterns and the subsequent dislocation density tensor calculation [23–25]. Considering the current experimental limitations in the determination of orientation gradients via EBSD [26], these methods can provide microstructurally based insights into the mechanisms of strain hardening and size-dependent plasticity. However, the calculated dislocation density is a lower bound of the total dislocation density because only GNDs are considered. In this regard, the present ECCI–EBSD approach provides a better estimate of the total dislocation density, which is similar to that obtained by conventional TEM, as confirmed by the present results.

In summary, the average dislocation density in a Fe–3 wt.% Si alloy tensile deformed to a macroscopic stress of 500 MPa has been determined by ECCI using a novel SEM-EBSD-based set-up. We have studied the influence of the diffraction conditions on the measure-

ment of the dislocation density in ECCI. Under optimum diffraction conditions, ECCI provides an average dislocation density close to that obtained by standard bright-field TEM. This result confirms that ECCI is a powerful and versatile wide-field-of-view technique to determine dislocation densities in deformed metals.

The authors would like to acknowledge the financial support by the German Research Foundation in the framework of the SFB 761 “steel ab initio”.

- [1] P. Hirsch, A. Howie, R.B. Nicholson, D.W. Pashley, M.J. Whelan, *Electron Microscopy of Thin Crystals*, Robert E. Krieger, Huntington, NY, 1977.
- [2] G. Thomas, M.J. Goringe, *Transmission Electron Microscopy of Materials*, John Wiley & Sons, New York, 1979.
- [3] D.B. Williams, C.B. Carter, *Transmission Electron Microscopy. A Textbook for Materials Science*, Springer Verlag, Berlin, 2009.
- [4] T. Ungár, H. Mughrabi, M. Wilkens, *Acta Metall.* 30 (1982) 1861.
- [5] T. Ungár, S. Ott, P.G. Sanders, A. Borbély, J.R. Weertman, *Acta Mater.* 46 (1998) 3693.
- [6] D.C. Joy, D.E. Newbury, D.L. Davidson, *Rev. Phys. Appl.* 53 (1982) 81.
- [7] A.J. Wilkinson, G.R. Anstis, J.T. Czernuszka, N.J. Long, P.B. Hirsch, *Philos. Mag. A* 68 (1993) 59.
- [8] A.J. Wilkinson, P.B. Hirsch, *Micron* 28 (1997) 279.
- [9] I. Gutierrez-Urrutia, S. Zaefferer, D. Raabe, *Scr. Mater.* 61 (2009) 737.
- [10] Z.F. Zhang, Z.G. Wang, Z.M. Sun, *Acta Mater.* 49 (2001) 2875.
- [11] B.C. Ng, B.A. Simkin, M.A. Crimp, *Ultramicroscopy* 75 (1998) 137.
- [12] A. Weidner, S. Martin, V. Klemm, U. Martin, H. Biermann, *Scr. Mater.* 64 (2011) 513.
- [13] I. Gutierrez-Urrutia, S. Zaefferer, D. Raabe, *Mater. Sci. Eng. A* 527 (2010) 3552.
- [14] I. Gutierrez-Urrutia, D. Raabe, *Acta Mater.* 59 (2011) 6449.
- [15] D. Raabe, M. Sachtleber, Z. Zhao, F. Roters, S. Zaefferer, *Acta Mater.* 49 (2001) 3433.
- [16] S. Zaefferer, *J. Appl. Crystallogr.* 33 (2000) 10.
- [17] J.P. Spencer, C.J. Humphreys, P.B. Hirsch, *Philos. Mag.* 26 (1972) 193.
- [18] A.J. Wilkinson, P.B. Hirsch, *Philos. Mag. A* 72 (1995) 81.
- [19] M.A. Crimp, B.A. Simkin, B.C. Ng, *Philos. Mag. Lett.* 81 (2001) 833.
- [20] R.K. Ham, *Philos. Mag.* 69 (1961) 1183.
- [21] L. Reimer, H. Kohl, *Transmission Electron Microscopy. Physics of Image Formation*, Springer Verlag, Berlin, 2008.
- [22] D. Griffiths, J.N. Riley, *Acta Metall.* 14 (1966) 755.
- [23] E. Demir, D. Raabe, N. Zaafarani, S. Zaefferer, *Acta Mater.* 57 (2009) 559.
- [24] S. Sun, B.L. Adams, W.E. King, *Philos. Mag. A* 80 (2000) 9.
- [25] L.P. Kubin, A. Mortensen, *Scr. Mater.* 48 (2003) 119.
- [26] T.B. Britton, C. Maurice, R. Fortunier, J.H. Driver, A.P. Day, G. Meaden, D.J. Dingley, K. Mingard, A.J. Wilkinson, *Ultramicroscopy* 110 (2010) 1443.

Dislocation and twin substructure evolution during strain hardening of an Fe–22 wt.% Mn–0.6 wt.% C TWIP steel observed by electron channeling contrast imaging

I. Gutierrez-Urrutia*, D. Raabe

Max-Planck-Institut für Eisenforschung, Max-Planck Str. 1, D-40237 Düsseldorf, Germany

Received 11 March 2011; received in revised form 3 July 2011; accepted 4 July 2011

Available online 29 July 2011

Abstract

We study the kinetics of the substructure evolution and its correspondence to the strain hardening evolution of an Fe–22 wt.% Mn–0.6 wt.% C TWIP steel during tensile deformation by means of electron channeling contrast imaging (ECCI) combined with electron backscatter diffraction (EBSD). The contribution of twin and dislocation substructures to strain hardening is evaluated in terms of a dislocation mean free path approach involving several microstructure parameters, such as the characteristic average twin spacing and the dislocation substructure size. The analysis reveals that at the early stages of deformation (strain below 0.1 true strain) the dislocation substructure provides a high strain hardening rate with hardening coefficients of about $G/40$ (G is the shear modulus). At intermediate strains (below 0.3 true strain), the dislocation mean free path refinement due to deformation twinning results in a high strain rate with a hardening coefficient of about $G/30$. Finally, at high strains (above 0.4 true strain), the limited further refinement of the dislocation and twin substructures reduces the capability for trapping more dislocations inside the microstructure and, hence, the strain hardening decreases. Grains forming dislocation cells develop a self-organized and dynamically refined dislocation cell structure which follows the similitude principle but with a smaller similitude constant than that found in medium to high stacking fault energy alloys. We attribute this difference to the influence of the stacking fault energy on the mechanism of cell formation.

© 2011 Acta Materialia Inc. Published by Elsevier Ltd. All rights reserved.

Keywords: Strain hardening; Electron channeling contrast imaging; Austenitic steel; Dislocation structures; Deformation twinning

1. Introduction

High-manganese steels have received much interest in recent years due to their outstanding mechanical properties combining high strength and ductility. This property profile is attributed to their high strain hardening capacity. High-manganese steels are typically austenitic steels, i.e. face-centered cubic (fcc) alloys, with a high Mn content (above 20% wt.%) and additions of elements such as carbon (<1 wt.%), silicon (<3 wt.%) and aluminum (<10 wt.%). This steel grade exhibit different hardening mechanisms, such as transformation-induced plasticity

(TRIP) [1,2], twinning-induced plasticity (TWIP) [1,3–8] or microband-induced plasticity (MBIP) [9,10]. The activation of these mechanisms is strongly dependent on the stacking fault energy. TRIP is observed in very low stacking fault steels (below 20 mJ m^{-2}) and is associated with the transformation of austenite (fcc phase) into ϵ -martensite (hexagonal close-packed phase), which in turn further acts as nucleus of α' -martensite (body-centered cubic or tetragonal phase) [11,12]. TWIP is observed in medium stacking fault energy steels ($20\text{--}40 \text{ mJ m}^{-2}$) and is characterized by the formation of deformation twins with nanometer thickness. MBIP has been recently reported in steel grades with high stacking fault energy ($\sim 90 \text{ mJ m}^{-2}$) and is attributed to the formation of microbands, which are in-grain shear zones that are confined by geometrically nec-

* Corresponding author. Tel.: +49 2116792 211; fax: +49 2115792333.

E-mail address: i.gutierrez@mpie.de (I. Gutierrez-Urrutia).

essary boundaries or conventional grain boundaries. These microstructure features (ϵ -martensite plates, deformation twins and microbands) lead to a remarkable variety of strain hardening phenomena as they all act as effective obstacles for dislocation glide. High-manganese TWIP steels are characterized by a hierarchical microstructure refinement that includes complex dislocation and twin substructures, and their interactions. Although there are some previous studies on the strain hardening behavior in TWIP steels, the details of the underlying kinetics of the substructure evolution and its correspondence to the stress–strain and strain hardening evolution is not yet fully understood. Most of these works analyze strain hardening in terms of a dislocation mean free path (MFP) approach, focusing essentially on a single microstructure parameter, namely, the twin spacing [3,13–17]. These works attribute the high strain hardening rate at intermediate strains (0.1–0.2 true strain) to twin spacing refinement. The increasing density of deformation twin boundaries and the strong effect they have on dislocation glide leads to the so-called “dynamic Hall–Petch effect”. However, our analysis reveals that the deformed microstructure of these alloys is too complicated to be reduced to a single microstructure parameter and, therefore, a detailed analysis of the contribution of dislocation and twin substructures, as well as their interactions, to strain hardening is required.

One important limitation in the characterization of TWIP steels is the complexity of the microstructure, which involves features of different length scales: deformation twins with thicknesses of some tens of nanometers [3,16,18] and dislocation substructures extending over several micrometers. As a consequence of this scale discrepancy, quantitative microstructure characterization by conventional electron microscopy techniques such as electron backscatter diffraction (EBSD) or transmission electron microscopy (TEM) is limited due to the angular resolution (EBSD) and the small field of view (TEM), respectively. In this study, therefore, we make use of electron channeling contrast imaging (ECCI), which is conducted in a scanning electron microscope (SEM), to perform a quantitative characterization of the deformation microstructure of TWIP steel. The ECCI technique has been established as an excellent tool for examining complex deformation microstructures of metallic materials, revealing microstructure features such as deformation twins, stacking faults and complex dislocation arrangements from a wide field of view directly in the SEM [6,19–25]. The reason for the recent improvement in the ECCI technique lies in its combination with EBSD. This allows us to efficiently identify optimum contrast conditions and, therefore, produce ECCI images of crystal defects under controlled diffraction conditions [24].

The present study aims at understanding the strain hardening behavior of an Fe22 wt.% Mn–0.6 wt.% C TWIP steel through a complete quantitative characterization of the dislocation and twin substructure evolution via an EBSD-optimized ECCI approach. The contribution of

the so-characterized substructure to the strain hardening is analyzed in terms of the dislocation mean free path approach involving several microstructure parameters, such as the characteristic average twin spacing and the dislocation substructure length scale.

2. Experimental

The TWIP steel used in this study had the chemical composition Fe–22 wt.% Mn–0.6 wt.% C. The material was melted in an induction furnace under an Ar atmosphere and cast into round bars of 25 mm diameter. To avoid Mn segregation [26], samples were swaged to 20% area reduction at 1000 °C and subsequently solution-treated for 4 h at 1100 °C under Ar. Thereafter, samples were hot-rolled to 75% engineering thickness at 1000 °C followed by air cooling. The hot-rolled material showed a fully austenitic structure with an average grain size of 50 μm , which remained stable during deformation at room temperature.

Tensile tests were carried out at room temperature at an initial strain rate of $5 \times 10^{-4} \text{ s}^{-1}$. In addition to tensile testing to failure, interrupted tensile tests to true strains of $\epsilon = 0.05, 0.10, 0.30$ and 0.40 were performed to study the microstructural evolution as a function of strain. The tensile bone-shaped samples had an 8 mm gage length, 2 mm gage width and 1 mm gage thickness. The monotonic tensile deformation experiments were carried out on a tensile test instrument (Kammrath & Weiss GmbH, Dortmund, Germany) equipped with a digital image correlation (DIC) system (ARAMIS system, GOM-Gesellschaft für Optische Messtechnik mbH, 38106 Braunschweig, Germany) to measure the local and macroscopic strain distribution. Details of this set-up are described in Ref. [27]. The surface pattern required for DIC was obtained as explained in Ref. [6]. Averaged engineering strain values were retrieved from the corresponding strain maps and used to calculate the true stress–strain values.

Microstructures of the tensile deformed TWIP steel were examined by two types of scanning electron microscopy techniques, namely, electron back scatter diffraction (EBSD) and electron channeling contrast imaging (ECCI). The EBSD technique was used to analyze the local crystallographic texture together with the dislocation and twin substructure. Orientation maps were taken in a 6500 F JEOL field emission gun-scanning electron microscope equipped with a TSL OIM EBSD system at 15 kV acceleration voltage and with a working distance of 15 mm. EBSD maps are displayed as inverse pole figure (IPF) maps in the direction of the tensile axis (TA). The ECCI technique was used to image deformation twins and dislocation substructures, as introduced in a previous work on TWIP steels [6]. A recently reported new set-up for ECCI [24] was used in this study to obtain ECCI images under controlled diffraction conditions, enabling an enhanced dislocation and interface contrast. The set-up makes use of the EBSD technique for orienting the crystal into optimal diffraction con-

ditions. ECCI images were obtained with optimum contrast by orienting the matrix crystal exactly in the Bragg condition for a high-intensity reflection and exciting the corresponding diffraction vector in a “two-beam” condition. ECCI observations were carried out in a Zeiss Cross-beam instrument (XB 1540; Carl Zeiss SMT AG, Germany) consisting of a Gemini-type field emission gun electron column and a focused ion beam device (Orsay Physics). ECCI was performed at 10 kV acceleration voltage and a working distance of 6 mm, using a solid-state four-quadrant BSE detector. The microscope was run in the “high current” mode and an objective lens aperture of 120 μm was used.

3. Results

3.1. Strain hardening

Fig. 1 shows a set of true stress–strain curves of the Fe–22 wt.% Mn–0.6 wt.% C TWIP steel tensile deformed at a strain rate of $5 \times 10^{-4} \text{ s}^{-1}$. We include here both the complete and interrupted tensile tests. The TWIP steel exhibits excellent mechanical properties, combining high strength (ultimate tensile strength of 1.1 GPa) and ductility (elongation to failure of 50%). It is important to note that between 0.1 and 0.2 true strain the stress–strain curve assumes a slightly concave shape, i.e. at this strain level secondary strain hardening effects seem to occur.

Fig. 2 shows the normalized strain hardening rate (normalized by the shear modulus) vs. flow stress (a) and true strain (b) of the tensile deformed material. Arrows indicate the different deformation stages described in the subsequent section. The main features revealed in Fig. 2 are, first, the remarkably high overall strain hardening rate and, second, the fact that the curve reveals a minimum at intermediate strains (0.06–0.1 true strain). This hardening

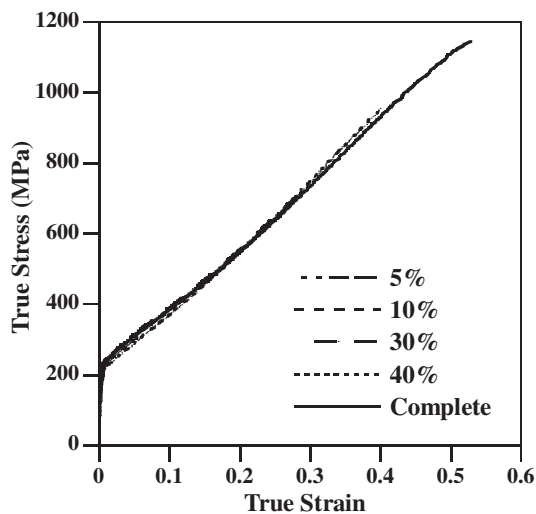


Fig. 1. True stress–true strain curves of Fe–22 wt.% Mn–0.6 wt.% C TWIP steel corresponding to interrupted and complete (i.e. until rupture) tensile tests. Initial strain rate: $5 \times 10^{-4} \text{ s}^{-1}$.

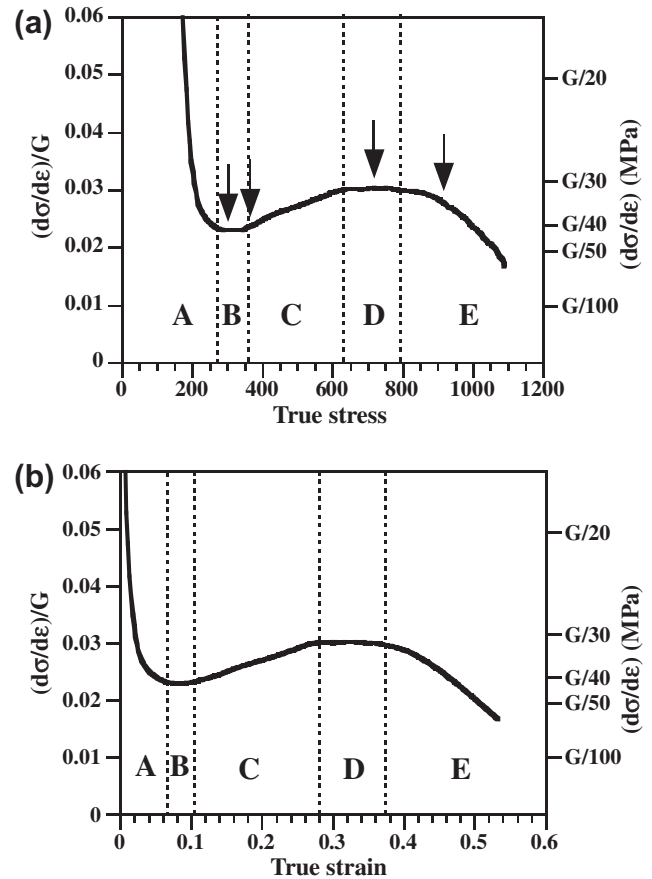


Fig. 2. Normalized strain hardening rate (normalized by the shear modulus) vs. true stress (a) and true strain (b) of tensile deformed Fe–22 wt.% Mn–0.6 wt.% C TWIP steel.

stage is followed by a high strain hardening rate at higher deformations. Typically, structural metallic alloys reveal a monotonous decay of the strain hardening rate as a function of strain. More specifically, in the current study five different deformation stages can be clearly distinguished in the evolution of the strain hardening rate with the true stress. The first stage, referred to as stage A, is characterized by a continuous decrease in the strain hardening rate until 270 MPa. This stage is similar to the stage III hardening regime of fcc metals with high stacking fault energy, such as copper and aluminum [28]. At this stress level, the strain hardening coefficient is about $G/40$, where G is the shear modulus. The hardening rate remains almost constant with a strain hardening coefficient of about $G/40$ during a small stress increment until 360 MPa (stage B). With increasing stress, the strain hardening rate increases gradually, reaching a strain hardening coefficient of about $G/30$ at 630 MPa (stage C). With further stress, the strain hardening rate is nearly constant, with a strain hardening coefficient of about $G/30$ up to a stress level of 800 MPa (stage D). Finally, the strain hardening rate decreases until rupture (stage E). It should be pointed out that the labeling of the hardening stages used in this work must not be confused with the classical hardening stage analysis used for

single crystals and polycrystals, which does not reveal a minimum in strain hardening after the classical stage III hardening regime.

3.2. Texture evolution

In its initial hot-rolled and homogenized state the material showed a fully austenitic structure, which remained stable during deformation at room temperature. No evidence of ϵ -martensite was detected by EBSD on the tensile deformed samples. Fig. 3 shows the texture evolution of the TWIP steel during tensile deformation. Fig. 3a shows the IPF for the crystal direction along the TA of the initial material, revealing a weak texture before the tensile test. Fig. 3b–e shows the textures in terms of TA-IPFs of the steel deformed to 0.05, 0.10, 0.30 and 0.40 true strain, respectively. We observe that the texture sharpens slightly during tensile deformation. At 0.3 true strain, the texture is characterized by two strong components, namely $\langle 111 \rangle // \text{TA}$ and $\langle 001 \rangle // \text{TA}$, which both remain stable

and sharpen slightly further during the ongoing deformation. Similar textures have been previously observed in tensile deformed TWIP steels at room temperature [16,29].

3.3. Evolution of the dislocation and twin substructure

At the early stage of deformation (strain below a true strain of 0.1), the microstructure mainly consists of dislocation substructures, with very few deformation twins. In this regime, the twinned area fraction is about 0.001 (Fig. 4a and b). Parts (a) and (b) of the figure show ECCI images of deformed microstructures of TWIP steels at 0.05 true strain/310 MPa and 0.1 true strain/380 MPa, respectively. These stress levels fall into stage B of strain hardening. The micrographs reveal that less than 20% of all grains contain deformation twins, which are mainly distributed along a single active twinning system (the primary twin system). At this stage of deformation, planar arrangements of dislocations consisting of dense dislocation layers forming on planes corresponding to the most active slip systems

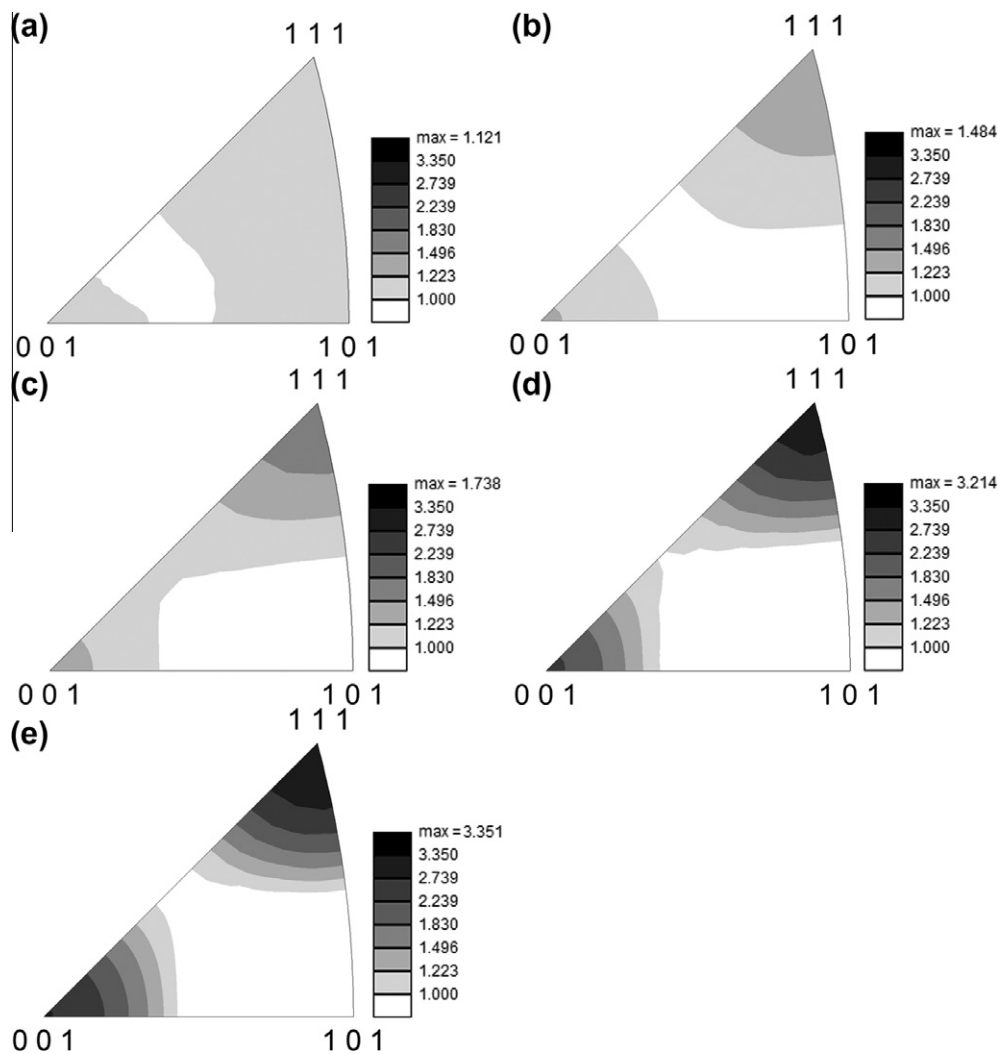


Fig. 3. IPFs along the TA direction of Fe–22 wt.% Mn–0.6 wt.% C TWIP steel in different states: as hot-rolled (a); tensile deformed to 0.05 true strain (b); 0.1 true strain (c); 0.3 true strain (d); 0.4 true strain (e).

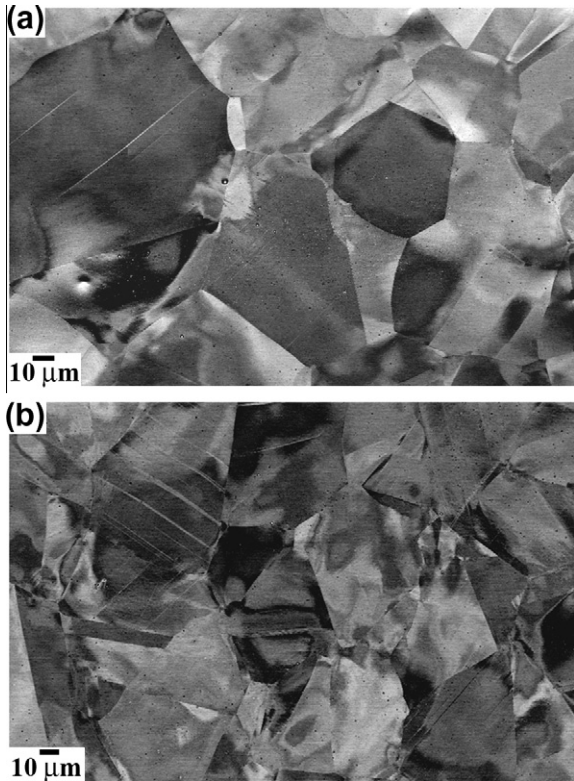


Fig. 4. ECCI images of deformed microstructures at 0.05 true strain (a) and 0.1 true strain (b), respectively.

are visible, as illustrated in the ECCI image in Fig. 5a. These dislocation substructures are referred to as highly dense dislocation walls (HDDWs) [30–32]. HDDWs are dislocation boundaries with a high dislocation density and a rotational component separating regions with different combinations of simultaneously operating glide systems. HDDWs appear in the ECCI images under the corresponding Bragg condition as bright straight compact layers penetrating the whole grain. This dislocation pattern is similar to that obtained in bright-field TEM images of HDDWs in medium-to-high stacking fault energy metals [30,31]. However, the contrast in ECCI imaging is reverted compared to that obtained in bright-field TEM due to the electron channeling mechanism and the diffraction conditions used to image dislocation substructures. In particular, Fig. 5a shows an example of HDDWs formed along the $(-1\ 1\ -1)$ slip plane on a sample that was tensile deformed to 0.05 true strain. The ECCI-based slip trace analysis was conducted by an accompanying EBSD map in the same area. HDDWs have been observed in medium-to-high stacking fault energy metals [30,31] as well as in low stacking fault energy alloys [33,34].

With further straining (to 0.1 true strain), a heterogeneous dislocation substructure is formed due to the multiple character of slip (planar and wavy), as illustrated in Fig. 5b. Planar slip promotes the formation of structures created by the intersection of HDDWs on two different slip planes, referred to as HDDW structures. These intersec-

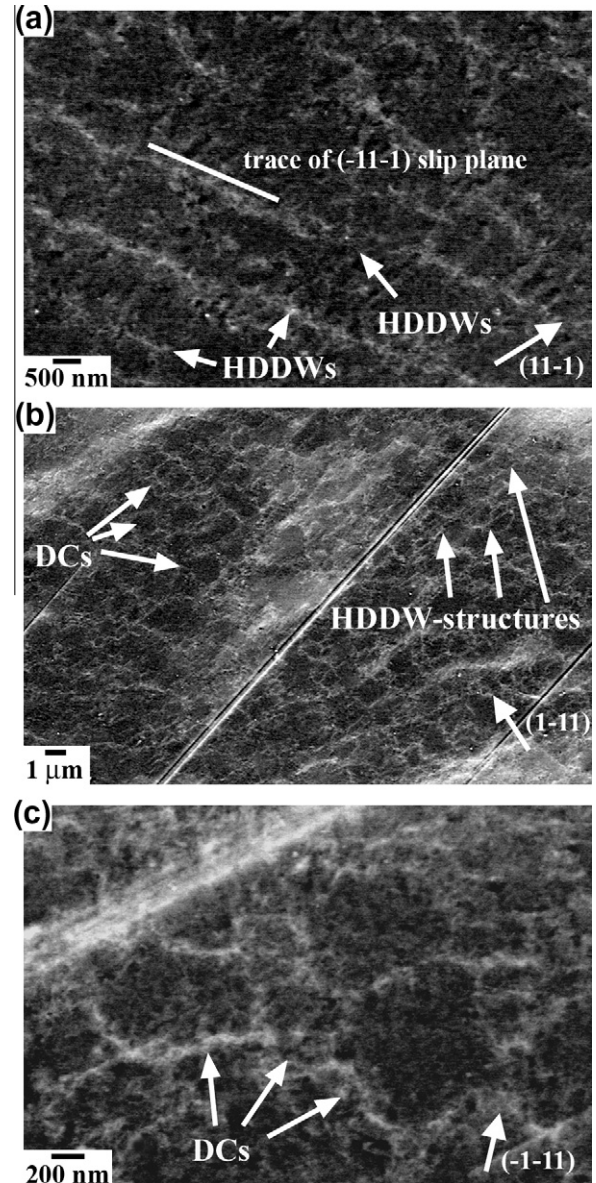


Fig. 5. ECCI images of deformed microstructure at the early stages of deformation (strain below 0.1 true strain). (a) HDDWs along the $(-1\ 1\ -1)$ slip plane on a sample tensile deformed to 0.05 true strain. The ECCI image was obtained by orienting the grain into Bragg condition using the $(1\ 1\ -1)g$ vector (arrow). (b) DCs and HDDW structures in a sample tensile deformed to 0.1 true strain. The ECCI image was obtained by orienting the grain into Bragg condition using the $(1\ -1\ 1)g$ vector (arrow). (c) Details of the DC structure on a sample tensile deformed to 0.05 true strain. The ECCI image was obtained by orienting the grain into Bragg condition using the $(-1\ -1\ 1)g$ vector (arrow).

tions lead to a checkerboard-type pattern, which is commonly observed in low stacking fault energy metals [33,34]. Wavy slip promotes the formation of equiaxed dislocation cells (DCs) similar to those observed in medium-to-high stacking fault energy metals [30,32]. These dislocation substructures appear in ECCI images under the current diffraction conditions as bright globular structures with a sharp boundary contrast. This dislocation pattern is similar to that obtained in bright-field TEM, as shown

in a previous work [24]. As discussed before, the contrast in ECCI is reverted to that in bright-field TEM due to the electron channeling mechanism and the diffraction conditions used to image dislocation substructures. The ECCI image shown in Fig. 5c reveals in detail dislocation cells with sizes ranging between 500 and 1000 nm formed at 0.05 true strain. At this strain, the average size of the dislocation substructure (both HDDW structures and DCs) is 750 nm. With further strain (0.1 true strain), the dislocation substructure is refined to an average size of 650 nm.

At a true strain of 0.3, the twinning activity increases remarkably, leading to the development of a well-defined twin substructure. At this stage, most of the grains contain deformation twins that are active in several systems (up to three twinning systems in the same grain are observed), and only around 10% of the grains are free of deformation twins. With further straining, the twin activity increases slightly. Fig. 6a and b shows ECCI images of the twin substructure formed at 0.3 true strain/720 MPa (stage D of strain hardening) and 0.4 true strain/920 MPa (stage E of strain hardening), respectively. These images show the formation of a well-defined twin substructure that penetrates the grains and subgrains. These crystals have sizes in the range between 10 and 40 μm . It can be also seen that even at high strains some grain regions remain free of deformation twins. At this stage (0.3–0.4 true strain), we can systematically distinguish three types of grains/subgrains according to the twin substructure occurring in them: type

I grains, which are characterized by a low deformation twinning activity; type II grains, which contain a well-developed twin substructure along one active twinning system (the primary twin system according to the highest Schmid factor); and type III grains, which build up a well-developed twin substructure along more than one active twinning system (primary and secondary twin systems). We define primary twin systems as those systems with the highest Schmid factor. The other twin systems are referred to as secondary twin systems. The evolution of the grain area fraction, the average size of dislocation substructures and the average twin spacing of each type of grain are shown in Table 1.

3.4. Orientation dependence of the dislocation and twin substructure

The grain orientation dependence of the twin substructure was analyzed via EBSD mapping in 150 individual grains/subgrains of a sample tensile deformed to 0.3 true strain. About 10 regions were characterized for each grain/subgrain. The average orientation is plotted in the TA-IPF of Fig. 7, with red, green and blue dots corresponding to type I, II and III grains, respectively. The data reveal that the different types of twin substructures observed are characteristic of specific orientation components: type I grains (low twinning activity) are oriented close to $\langle 001 \rangle // \text{TA}$ directions within an angular range of approximately 15° ; type II grains (primary twin system active) are oriented along the line between $\langle 001 \rangle // \text{TA}$ and $\langle 111 \rangle // \text{TA}$ directions; and type III grains (primary and secondary twin systems active) are oriented close to $\langle 111 \rangle // \text{TA}$ directions within an angular range of approximately 15° .

Figs. 8–10 show ECCI images of type I, II and III grains, respectively. Type I grains occur less frequently with an area fraction of about 10%. These grains/subgrains are oriented close to $\langle 001 \rangle // \text{TA}$ directions and exhibit low deformation twinning activity, as is evident from the small amount of twin bundles (Fig. 8a). These bundles are nucleated at grain boundaries and do not extend further up to the opposite grain boundary, but they only grow a few microns into the grain interior without impinging on other interfaces. Type I grains contain a fine equiaxed dislocation cell structure, with an average cell size of 220 nm at 0.3 true strain (Fig. 8b). Further straining (0.4 true strain) leads to a slight refinement of the cell size to an average value of 180 nm. Type II grains, with an area fraction of about 30%, exhibit significant deformation twinning activity. These grains/subgrains are oriented along the line between the $\langle 001 \rangle // \text{TA}$ and $\langle 111 \rangle // \text{TA}$ crystallographic directions. They contain a lamellar twin structure along a primary twinning system, as shown in Fig. 9a. At 0.3 true strain, the average twin spacing is 320 ± 50 nm, which is slightly reduced to 280 ± 50 nm with increasing deformation to 0.4 true strain. Fig. 9b shows that the lamellar twin structure is formed by single deformation twins, with a

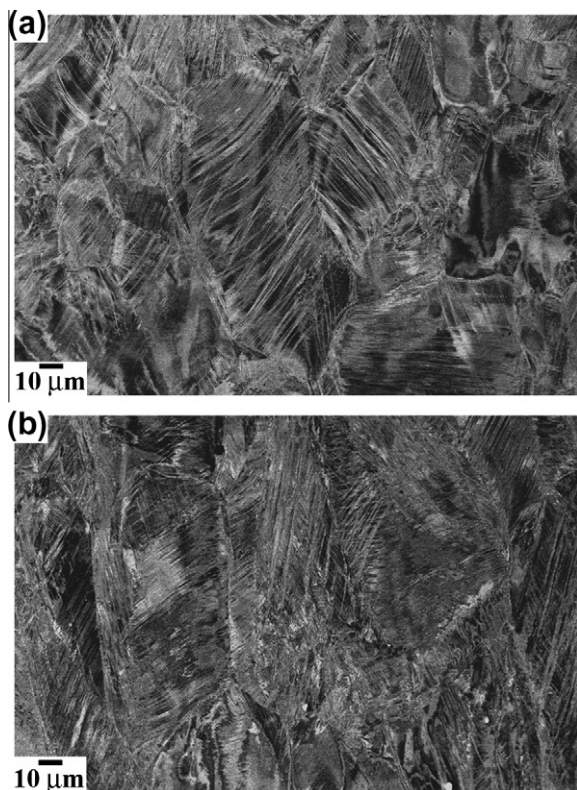


Fig. 6. ECCI images of deformation microstructures at 0.3 true strain (a) and 0.4 true strain (b), respectively.

Table 1

Evolution of the grain area fraction, the average size of dislocation substructures, and the average twin spacing with true strain/stress in type I, II and III grains. Type I grains: equiaxed cell structure with a low deformation twinning activity; type II grains: well-developed twin substructure along one active twinning system (primary twin system); type III grains: dislocation cells and highly-dense dislocation walls-structures with a well-developed twin substructure along more than one active twinning system (primary and secondary twin systems) (see also Figs. 7 and 15).

True strain	True stress (MPa)	Type I		Type II		Type III		
		Area fraction (%)	Dislocation substructure size (nm)	Area fraction (%)	Twin spacing (nm)	Area fraction (%)	Twin spacing (nm)	Dislocation substructure size (nm)
0.05	310	100	750 ± 150	0	–	0	–	–
0.1	380	~100	650 ± 100	0	–	0	–	–
0.3	720	10	220 ± 50	30	320 ± 50	60	430 ± 100	550 ± 100
0.4	920	10	180 ± 50	30	280 ± 50	60	260 ± 50	450 ± 100

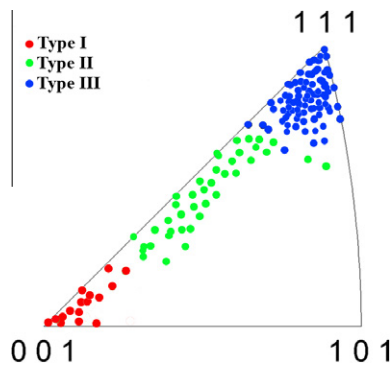


Fig. 7. IPFs along the TA direction showing experimental grain orientations of a sample deformed to 0.3 true strain with red, green and blue dots corresponding to type I, II and III grains, respectively. The classification indicates basic differences in the dislocation cell and twinning substructures developed in the different grains: type I grains: equiaxed cell structure with a low deformation twinning activity; type II grains: well-developed twin substructure mainly along one active twinning system (primary twin system: system with highest Schmid factor); type III grains: DCs and HDDW structures with a well-developed twin substructure along more than one active twinning system (primary and secondary twin systems) (see also Fig. 15 and Table 1).

thickness distribution ranging from 30 to 100 nm. At 0.3–0.4 true strain, the average twin thickness is 80 ± 20 nm. True twin thicknesses and spacings were determined by ECCI observations at high magnification for a set of about 500 deformation twins under diffraction conditions with a $\{111\}$ plane reflector parallel to the twin interface, i.e. the twins were monitored in edge-on position. Fig. 9a and b reveals that twin boundaries cut through the existing dislocation substructure developed during the early stages of deformation (HDDW structures and DCs) without experiencing strong resistance. As a consequence, a new block-shaped nanostructure is formed, as revealed in Fig. 9b. This nanostructure consists of twin boundaries along the active twin system and dislocation walls (HDDWs or cell walls) formed along the most active slip systems. The average size of the blocky nanostructure can be roughly estimated as the twin spacing times the cell size,

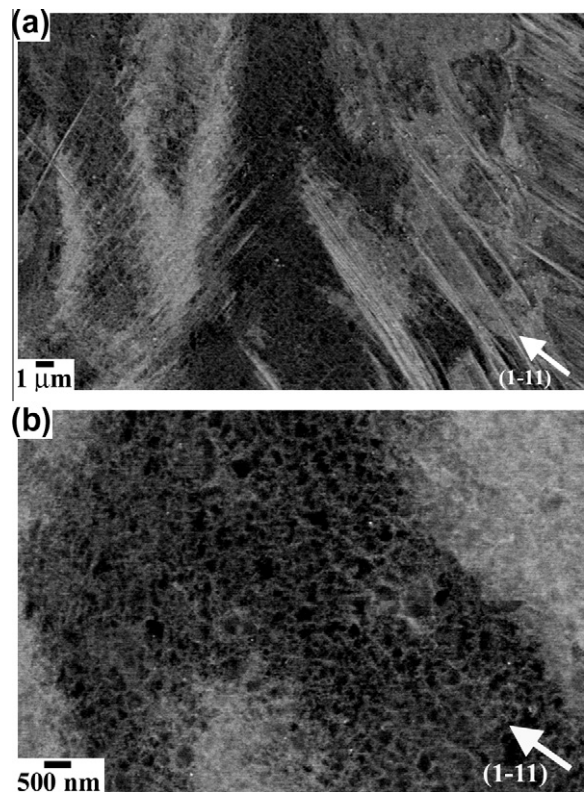


Fig. 8. ECCI images of deformation microstructure of a type I grain at 0.3 true strain. ECCI images were obtained by orienting the grain into Bragg condition using the $(1-11)g$ vector (arrow). (a) Large field of view image showing dislocation cells and bundles of twins. (b) Details of the dislocation cell structure.

which is about $300 \text{ nm} \times 500 \text{ nm}$ in the 0.3–0.4 true strain regime. Type III grains are the most frequently occurring grains, with an area fraction of 60%. These grains are oriented close to $\langle 111 \rangle // \text{TA}$ directions and exhibit a significant deformation twinning and dislocation activity. The twinning activity results in a well-defined twin substructure consisting of a primary twin system and one or two secondary twin systems (Fig. 10a). Deformation twins are typically arranged in bundles with thicknesses between 80 and 450 nm. Thin deformation twins with a thickness

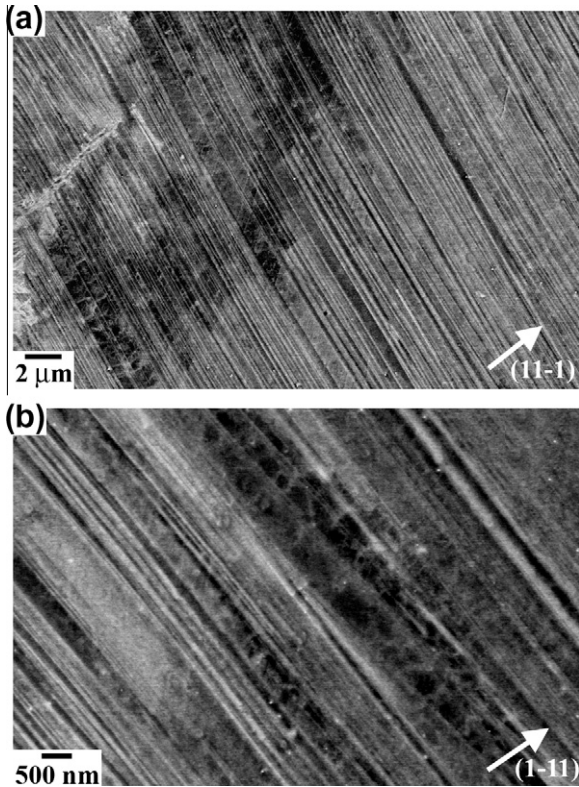


Fig. 9. ECCI images of deformation microstructure of a type II grain at 0.3 true strain. (a) Large field of view image showing a lamellar twin structure. The ECCI image was obtained by orienting the grain into Bragg condition using the $(1\ 1\ -1)g$ vector (arrow). (b) Details of the lamellar twin structure. Dislocation boundaries are visible in areas with large twin spacing. The ECCI image was obtained by orienting the grain into Bragg condition using the $(1\ -1\ 1)g$ vector (arrow).

between 20 and 60 nm are only observed on secondary twin systems, as illustrated in Fig. 10b. Apparent twin thicknesses were measured from ECCI images and corrected values were then determined by means of a stereological correction considering the corresponding tilting conditions. Fig. 10a and b reveals that these crystals contain a refined dislocation substructure, consisting of HDDW structures and DCs with an average size of 550 nm at 0.3 true strain. With further deformation (0.4 true strain), the structure is refined to an average value of 450 nm. Fig. 10 also reveals that the dislocation–twin interaction is similar to that occurring in type II grains. As a consequence, a rhomboid-shaped nanostructure of twin boundaries and dislocation walls (HDDWs or cell walls) is formed. The evolution of this nanostructure is further favored by twin–twin intersections due to the activation of multiple twin systems.

4. Discussion

4.1. Evolution of the dislocation and twin substructure

Two important aspects of the substructure evolution during tensile testing are quantitatively examined in this study, namely the dislocation and twin substructures. As

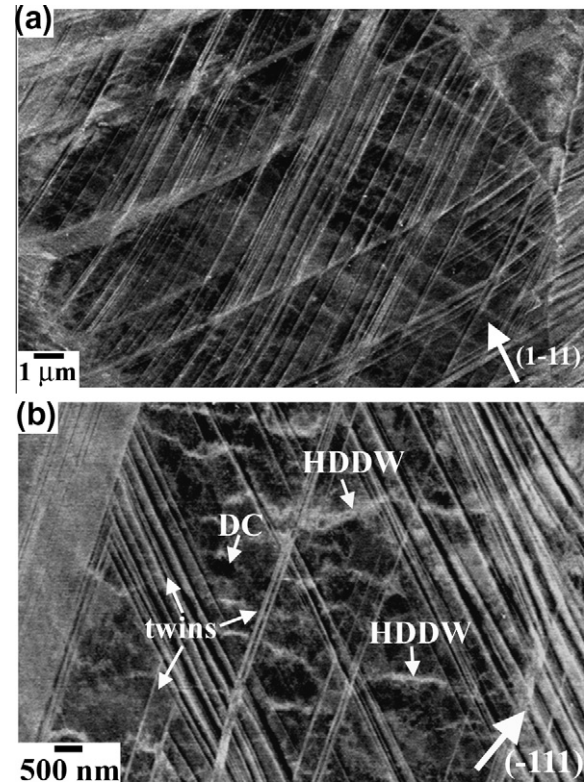


Fig. 10. ECCI images of deformation microstructure of a type III grain at 0.3 true strain. (a) Large field of view image showing a multiple twin structure with dislocation substructures. The ECCI image was obtained by orienting the grain into Bragg condition using the $(1\ -1\ 1)g$ vector (arrow). (b) Details of the dislocation substructure consisting of HDDWs and DCs. The ECCI image was obtained by orienting the grain into Bragg condition using the $(-1\ 1\ 1)g$ vector (arrow).

the ECCI images quantitatively reveal, during the early stages of deformation (strain below 0.1 true strain) the deformed microstructure is formed by DCs and highly dense dislocation arrangements (HDDWs and HDDW structures). ECCI images reveal dislocation patterns that are similar to those found in TEM observations on dislocation substructures in low-to-medium stacking fault energy metals [30–33]. In particular, the characteristic dislocation cell pattern observed by ECCI in the present FeMn alloy was confirmed by TEM in a previous work [24]. The dislocation substructures can be classified according to the character of the observed slip patterns, namely wavy or planar. The planar slip character in fcc metals is known to be mainly promoted by decreasing stacking fault energy, increasing friction stress and the occurrence of short-range ordering [35,36]. In the present TWIP steel, where ordering has not been observed, the two parameters that can promote planar slip are predominantly the friction stress ($\sigma_0 = 157$ MPa [17], which is higher than for materials exhibiting planar slip such as stainless steels [37,38]) and the stacking fault energy (22 mJ m^{-2} [39]). The latter effect promotes slip via Shockley partial dislocations. These can only cross-slip after stress- and thermally assisted local recombination, hence the planar slip prevalence in

materials with low stacking fault energy. With increasing strain (strain above 0.3 true strain), planar dislocation structures are further developed in grains that are characterized by a limited number of active slip systems, i.e. type II and III grains. Wavy dislocation structures are promoted in grains when a high number of slip planes are activated and dislocation cross-slip is enabled [30,40], such as in type I grains. Interestingly, in high stacking fault energy metals, such as pure aluminum, a similar crystallographic orientation dependence of the dislocation substructure was observed, as in the present Fe–Mn alloy [41]. This finding suggests that dislocation cell formation is promoted in similar crystal orientations in both low and high stacking fault energy metals, although the characteristic mechanism of cell formation may well be different, as discussed below. Regarding the formation of HDDWs in type III grains, the slip trace analysis conducted in 10 grains through combined ECCI and EBSD analysis reveals that most of the HDDWs are boundaries with a specific crystallographic orientation. Fig. 11a shows an example of HDDWs lying along two slip systems. The simulated diffraction pattern of the crystallographic orientation obtained from EBSD is shown in Fig. 11b. The grain is oriented close to the $(3 -1 -2)$ direction. Trace analysis reveals that the two sets

of HDDWs are formed with a specific crystallographic orientation. One set of HDDWs is formed along the $(1 -1 1)$ slip plane. The other set is formed along the $(1 -1 -1)$ slip plane within a range of 10° . The present observations on HDDWs agree with previous results obtained in low stacking fault energy alloys, such as Hadfield steel [33,34]. Our result suggests that in type III grains there are two active slip systems in the same slip plane that account for a large fraction of the total slip in the respective crystal [42].

In a previous work [6], we have shown that in the present alloy, when tensile deformed to a high true strain of 0.3, only grains with either a highly favorable or unfavorable orientation for twinning follow the Schmid behavior. These grains correspond to crystals oriented close to the $\langle 1 1 1 \rangle // TA$ and $\langle 0 0 1 \rangle // TA$ directions, respectively. This result indicates that in the present twin substructure only type III and I grains follow the Schmid behavior. The rest of the crystals, viz. type II grains with a lamellar twin structure, do not fulfill Schmid's law when considering the macroscopic load. We also observe that local stress concentrations at grain boundaries (e.g. those caused by the impingement of deformation twins formed in a neighboring grain on a grain boundary) can promote twinning in unfavorably oriented grains. These stresses can be high enough to activate the twin system with the highest Schmid factor (primary twin system). The developed twin substructure may hinder the growth of deformation twins on secondary twin systems because the stress required to build up a secondary twin substructure is probably too high to be attained during tensile deformation. As a consequence, only primary deformation twin is activated, resulting in a lamellar twin structure. This effect is similar to the well-known effect of overshooting in slip due to latent hardening.

It is worth noting the relatively small mechanical resistance that dislocation boundaries (cell walls and HDDWs) have against twin boundaries that cut through them. If we consider that the interaction is stress controlled, this observation indicates that dislocation boundaries have a small influence on the stress required for twin dislocations to pass through them. This is supported by the fact that mechanical twins, once nucleated, practically always penetrate grains to the opposite grain boundary. This behavior can be discussed in terms of the self-stresses that characterize the leading twin edge. Mechanical twins in fcc metals are formed by the passage of edge-type Shockley partial dislocations on successive twinning planes. These partials form inclined arrays at the twin–matrix interface. Therefore, a twin can be described by a field of discrete partial dislocations where the long-range field resembles that of a pile-up configuration of partials [43–45]. Kamat et al. [44] have shown that under usual deformation conditions a twin resembles a discontinuous tilt wall formed by inclined pile-ups. This means that a growing twin can be considered as a coordinated movement of partial dislocations that preserve their characteristic arrangement. The partial dislocations in this array are spaced by a value of h (Fig. 12a). The

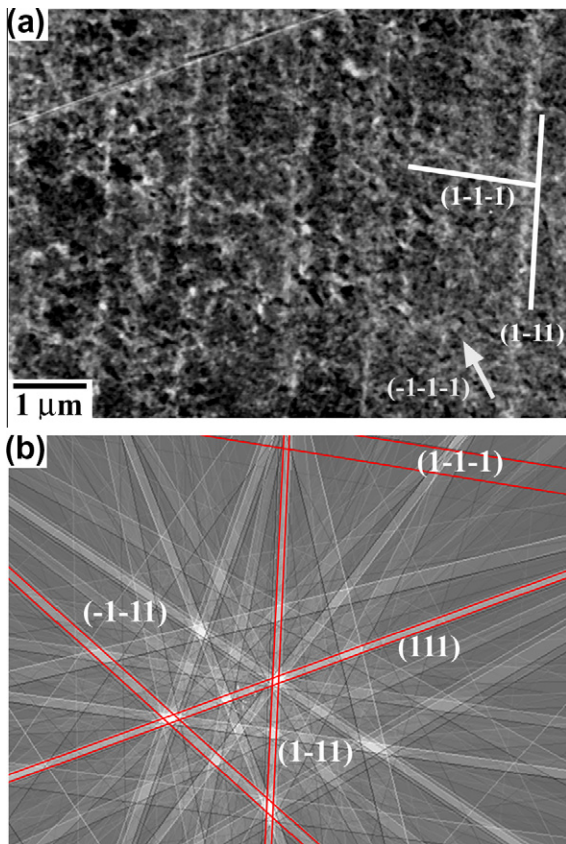


Fig. 11. Trace analysis of the crystallographic orientation of the alignment of HDDWs by using a combination of ECCI and EBSD. (a) ECCI image of HDDWs. (b) Simulated diffraction pattern of the corresponding crystal orientation. The crystal orientation is close to the $(3 -1 -2)$ direction//TA.

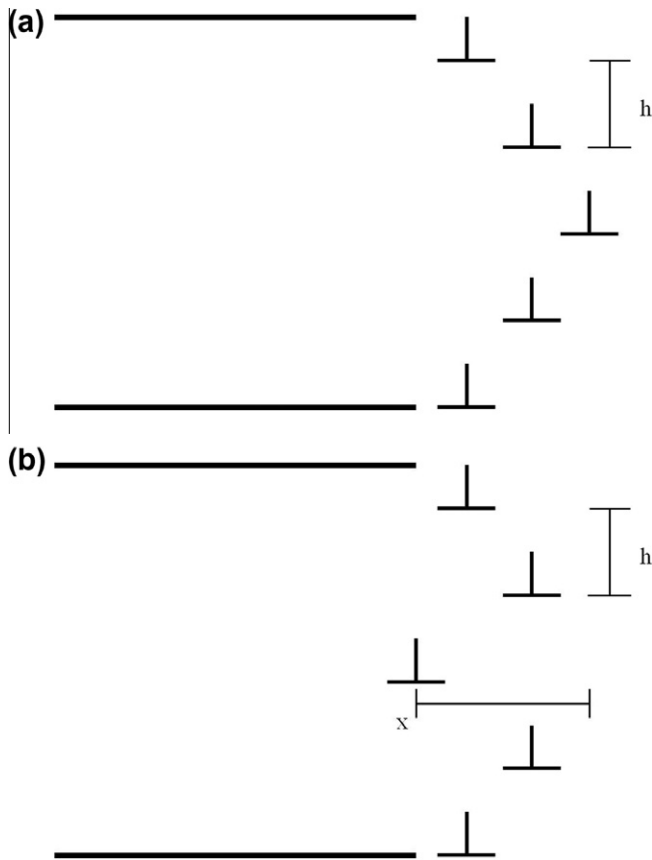


Fig. 12. Schematic representation of the leading edge of a deformation twin formed by a set of Shockley partials separated by distance h . (a) Twin tip in local mechanical equilibrium. (b) Twin tip out of local mechanical equilibrium with the leading partial dislocation being retarded and displaced by x . The local Peach–Koehler forces on this dislocation are in the GPa range, so the local mechanical equilibrium will push such a retarded dislocation back into the array against the obstacle force (such as from a forest interaction).

collective and highly coordinate movement of partial dislocations can be driven, for example, by screw dislocation poles [46,47]. We suggest that the required highly coordinate slip of partials is the reason for the relatively unimpeded penetration of deformation twins through existing dislocation arrangements compared to an equivalent set of partial dislocations in non-coordinated motion. When one of the partials is retarded due to a forest dislocation interaction between the twin tip and the dislocation substructure in front of it, and thus deviates from its ideal position within the twin tip, the local Peach–Koehler force by the other partials assembled in the twin tip array becomes very high and pushes it back into the required dislocation configuration. For example, the force, F , on the displaced partial dislocation (displacement, x) of the twin tip depicted in Fig. 12b due to partials of the twin tip array can be considered as the force provided by two superdislocations having a magnitude Nb , where N is the number of dislocations in the twin tip array and b is the Burgers vector. Accordingly, the force F can be written as: $F/b \sim GbN/x\pi(1 - \nu) + \gamma$, where G is the shear modulus, ν is the

Poisson ratio, N is the number of dislocations in the twin tip array and γ is the stacking fault energy. Assuming a displacement x of the Burgers vector b , the force is: $F/b \sim GN/\pi(1 - \nu) + \gamma$. This force is much higher than the self-stress field of a dislocation boundary or the back-driving force created by a forest reaction product [48], and consequently the trailing partial is pushed back to its position within the twin tip.

4.2. Scaling law for dislocation cell sizes

Fig. 13 shows the variation in average size of dislocation substructures with true stress in type I and type III grains. The figure reveals that the refinement in the dislocation substructure in type III grains (HDDW structures and DCs) is less significant than that observed in type I grains (DCs). This is attributed to the activation of twinning in type III grains. As slip and twinning are two competing deformation mechanisms, the strain accommodated by slip is remarkably reduced and therefore the dislocation substructure is less refined. The figure also reveals that the variation in average size of the DCs in type I grains follows the relationship $\sigma = k/D$, where σ is the true stress, k is a constant and D is the cell size. This is a widely observed empirical relationship that has been established in the framework of the mesh-length theory of work hardening [40]. According to this theory, dislocations tend to arrange into structures which minimize the elastic energy per unit length of the dislocation line (low energy dislocation configurations). One characteristic substructure type of arrangement, viz. dislocation cell formation, minimizes the elastic energy per unit length of dislocation line through this relationship. In particular, the following relationship between the flow stress and the cell size has been proposed for cell-forming metals [40], and is known as the “similitude principle”:

$$\tau = \tau_0 + KGb/D \quad (1)$$

where τ is the flow stress, τ_0 is the friction shear stress, K is the similitude constant, G is the shear modulus, b is the Burgers vector and D is the cell size. Fig. 14 shows relation

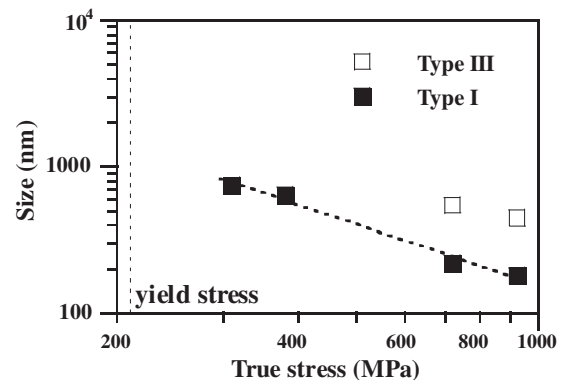


Fig. 13. Variation of the average size of the dislocation substructure with the true stress in type I grains (DCs, black symbols) and type III grains (dislocation cells plus HDDW structures, open symbols).

(1) for the present TWIP steel using $\sigma_0 = 157$ MPa [17], $b = 2.5 \times 10^{-10}$ m [15] and $G = 65$ GPa [15]. τ was obtained from σ assuming a Schmid factor m of 0.41, which corresponds to $\langle 001 \rangle // \text{TA}$ orientations. From this diagram a value for the constant K of 3.7 is obtained. This value is smaller than the commonly reported value for fcc metals (medium-to-high stacking fault energy metals), which ranges between 7 and 8 [49]. Although there are few studies on dislocation cell kinetics in low stacking fault energy alloys, a small value of the constant K between 2.0 and 2.9 has been reported for 316 L austenitic stainless steel [49,50], which is close to that obtained in the present study.

According to the mesh-length theory of work hardening, any fcc metal should develop a dislocation cell structure, according to the criterion:

$$10^2 \leq G/(\tau - \tau_0) \leq 10^5 \quad (2)$$

where G is the shear modulus, τ is the resolved shear stress and τ_0 is the friction stress. For the present steel, the term $G/(\tau - \tau_0)$ ranges between 1.7×10^2 and 1×10^3 , hence a dislocation cell structure is formed. However, it must be noted that this theory only accounts for dislocation cell formation on the basis of a low energy configuration criterion; it does not provide any detail on the kinetic mechanism of cell formation. Several observations revealed that dislocation cell formation is closely connected with the cross-slip ability of screw dislocations [48,51]. Cross-slip plays an important role in this process through the rearrangement of screw dislocations in terms of the activation of secondary slip and annihilation of screw dislocations of opposite sign. The localized maneuvers of partial dislocations to transfer dislocation screw segments from one plane to a cross-slip plane depends on the stacking fault energy [48,51]. Consequently, the stacking fault energy has an important influence on the characteristic mechanism of dislocation cell formation. For this reason, the mechanism of cell formation in the present TWIP steel may be different to that occurring in medium-to-high stacking fault energy

metals and therefore a different similitude constant K is obtained. Similar observations were recently reported in copper [49]. The material had been strained by cyclic deformation and a similar constant to that in the present study was found [49]. In their work, the authors attributed the low value of the similitude constant K to a higher storage rate of dislocations when compared to monotonic deformation. Although this aspect, viz. the high dislocation density, must also be taken into account in low stacking fault energy alloys due to the reduced activity of dislocation cross-slip, its effect on the mechanism of dislocation cell formation is not clear.

4.3. Strain hardening

Strain hardening of the Fe–22 wt.% Mn–0.6 wt.% C TWIP steel is characterized by a remarkably high strain hardening above a true stress of 270 MPa. Microstructure observations conducted by ECCI confirm that this is attributed to both dislocation accumulation and twin substructure formation.

Stage A hardening in the present alloy is characterized by a decrease in the strain hardening rate. It reveals similar features to the conventional stage III hardening regime observed in high stacking fault energy metals [28], and also agrees with previous studies on strain hardening of low stacking fault energy metals [52]. This observation suggests that this stage can be attributed to the prevalence of dynamic recovery processes, such as cross-slip and annihilation of screw dislocations of opposite signs. The microstructure observations indicate that stage B hardening, which is characterized by a constant strain hardening rate with a hardening coefficient of about $G/40$, can be attributed to the evolution of the dislocation substructure consisting of DCs and HDDW structures. The value of the strain hardening coefficient observed in this regime is much higher than the typical value of $G/200$ observed for multiple slip in common fcc metals [28] but is similar to that reported for Hadfield steels ($G/20$ – $G/30$ [33,34]). These alloys contain dislocation arrangements organized in HDDWs that act as effective obstacles against dislocation motion. Some portion of the blocked dislocations can become trapped by the boundaries, thereby increasing their dislocation density (i.e. the wall thickness). In the present alloy the presence of weaker obstacles (DCs) may result in less strain hardening. The present study hence shows for the first time the important effect of dislocation substructures on the strain hardening behavior in a TWIP steel.

The development of a dense twin substructure upon ongoing straining results in a further drastic decrease in the MFP. Consequently, strain hardening increases up to a hardening coefficient of about $G/30$, leading to stage C hardening. The microstructure observations reveal that twin boundaries cut through the existing dislocation substructure, resulting in further microstructure refinement. Twin boundaries act as strong obstacles to dislocation

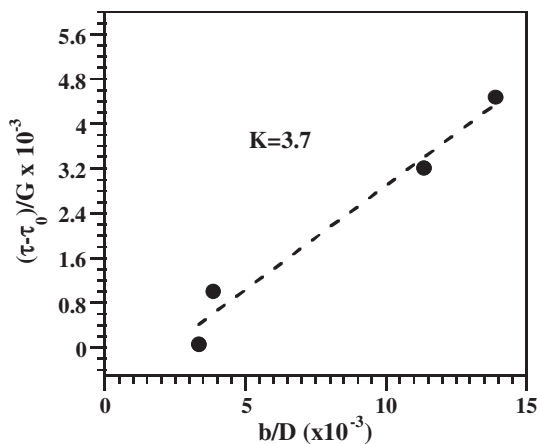


Fig. 14. Plot of the relation $(\tau - \tau_0)/G = Kb/D$ for average dislocation cell sizes in type I grains.

motion, serving as efficient sites for dislocation accumulation similar to grain boundaries. This effect is referred to as a “dynamic Hall–Petch effect”, and has been reported in many fcc metals containing deformation twins [3,15,16,52,53].

To obtain a better understanding of the influence of both dislocation and twin substructures to stage C hardening, we evaluate the contribution of the different types of grains (types I, II and III) to the flow stress at 0.3 true strain using an MFP approach. This strain level corresponds to the onset of stage D, where the highest strain hardening is obtained. The contribution of type I grains (cell forming grains) to the flow stress is provided by relation (1). Type II grains develop a block structure formed by twin boundaries and dislocation boundaries. As the average twin spacing is around half the average spacing between dislocation boundaries, we consider the average twin spacing to be the dominant microstructural correlation length in the overall MFP for mobile dislocations. Accordingly, we assume that the contribution of type II grains to the flow stress can be described in terms of a Hall–Petch-type relation [52]:

$$\sigma = \sigma_0 + K_{H-P}/(\lambda_{\text{twin}})^{1/2} \quad (3)$$

where σ_0 is the friction stress, K_{H-P} is the Hall–Petch constant for twinning and λ_{twin} is the average twin spacing. Type III grains develop a block structure formed by twin and dislocation boundaries (HDDWs and cell walls). As a first approximation, we consider only the smallest obstacle spacing, which is the average twin spacing of one of the active twinning system. We therefore assume that the contribution of type III grains to the flow stress is also provided by relation (3), with λ_{twin} being the smallest average twin spacing of the active twin system. Considering these three contributions, the expression for the flow stress can be written as:

$$\sigma = \sigma_0 + f_I G K b M / D + f_{II} K_{H-P} / (\lambda_{\text{twin}}^{II})^{1/2} + f_{III} K_{H-P} / (\lambda_{\text{twin}}^{III})^{1/2} \quad (4)$$

where σ_0 is the friction stress, f_I , f_{II} and f_{III} are the area fractions of type I, II and III grains, respectively, G is the shear modulus, b is the Burgers vector, K is a constant, M is the Taylor factor, D is the average cell size, K_{H-P} is the Hall–Petch constant for twinning, $\lambda_{\text{twin}}^{II}$ is the average twin spacing in type II grains, and $\lambda_{\text{twin}}^{III}$ is the smallest average twin spacing of an active twin system in type III grains. The area fraction, average size of dislocation substructures and average twin spacing of each type of grain are shown in Table 1. Assuming $\sigma_0 = 157$ MPa [17], $b = 2.5 \times 10^{-10}$ m [15], $G = 65$ GPa [15], $K = 3.7$ (calculated in the previous section), $M = 2.44$ (Taylor factor for type I grains) and $K_{H-P} = 357$ MPa $\mu\text{m}^{1/2}$ [17] (a previous work has shown that in the present TWIP steel the Hall–Petch constant for twinning is similar to that for slip [6]), and taking the microstructure parameters shown in Table 1, yields a flow

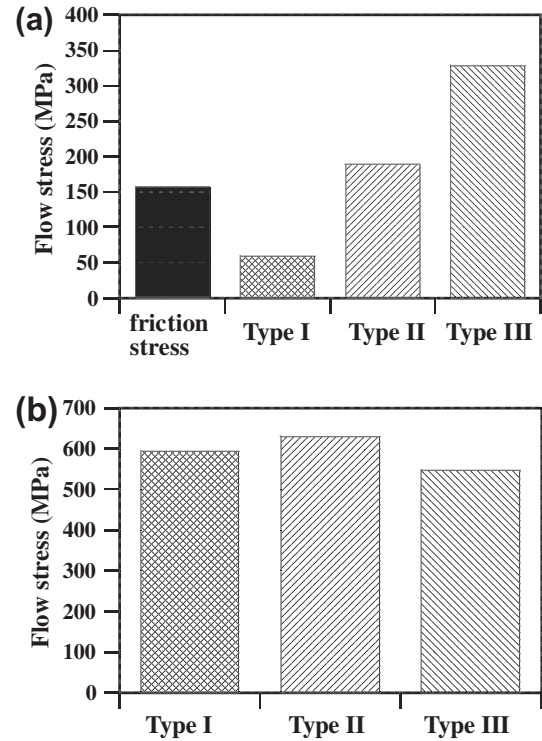


Fig. 15. (a) Contribution of the friction stress and type I, II and III grains to the flow stress at 0.3 true strain. (b) Intrinsic strength of type I, II and type III grains at 0.3 true strain. Type I grains: equiaxed cell structure with a low deformation twinning activity; type II grains: well-developed twin substructure along one active twinning system (primary twin system); type III grains: DCs and HDDW structures with a well-developed twin substructure along more than one active twinning system (primary and secondary twin systems) (see also Fig. 7 and Table 1).

stress of 735 MPa at 0.3 true strain. This value is close to the experimentally observed flow stress value of 720 MPa.

Two important findings can be drawn from this estimate. First, the strain hardening of a TWIP steel can be analyzed in terms of the MFP approach. This result agrees with published models on the hardening behavior of TWIP steels [13,14,17]. Second, we have identified the different microstructure parameters controlling strain hardening in this material, namely, the average dislocation cell size in type I grains, the average twin spacing in type II grains and the smallest average twin spacing of the active twin system in type III grains. Fig. 15a shows the contribution to the flow stress of each term occurring in relation (4). The figure reveals that the most significant contribution to the flow stress is provided by the twin substructure (type II and III grains) with about 70% contribution to the overall flow stress. In particular, type III crystals, which are the most frequently occurring grains, provide the highest contribution. Interestingly, the contribution of the dislocation substructure, which is mainly provided by type I grains, is still noticeable, with about 8% of the flow stress. This analysis clarifies the influence of the main microstructure features, namely dislocation and twin substructures, on the high strain hardening rate of TWIP steels. It shows that the high strain hardening rate observed in stage C is mainly attributed to the MFP refinement due to deformation

twinning in type II and III grains. If we only consider the intrinsic strength of each type of grain, we find that type II crystals (with a lamellar twin structure) are the hardest grains (Fig. 15b). Interestingly, this figure reveals that at this deformation stage type I grains (cell forming grains) exhibit an even higher strength than type III grains (multiple twin structure). This result supports the previous finding of the significant contribution of dislocation substructures on strain hardening in the present TWIP steel.

With further straining, the refinement of the twin spacing proceeds, leading to a further reduction in the dislocation MFP and a gradual decrease in the strain hardening rate. The hardening coefficient of stage D is still high ($G/30$), indicating the gradual refinement of the MFP, as also revealed by Table 1. Above a true stress of 800 MPa, in stage E, strain hardening steadily decreases, indicating the reduced capability for trapping more dislocations inside the refined microstructure. The work hardening capability is determined not only by the MFP but also by the specific strengthening effect of the deformation twins when they act as obstacles against dislocation motion. In the present FeMn alloy, deformation twins are arranged in bundles. Microstructure observations reveal that the bundle density and thickness increase gradually with strain. This indicates that the number of deformation twins arranged in bundles increases with the strain as well. These bundles are even stronger obstacles to dislocation glide than single twins because the critical stress required to carry plastic deformation across the twin bundle is much higher than that required to penetrate a single twin due to the small interface spacing. Another result supporting the increasing twin strength with deformation is the high density of sessile dislocations found within twin lamellae in an Fe–20 wt.% Mn–1.2 wt.% C TWIP steel [7,18]. The accumulation of sessile dislocations within the twin is attributed to dislocation reactions between Shockley partials and twin dislocations. These sessile dislocations are potential obstacles to dislocation motion and can provide not only a hardening mechanism within deformation twins but also an increase in the critical stress required to induce plastic deformation across the twin as well. Furthermore, in the present TWIP steel, Shockley partial-twin dislocation interactions can be enhanced by the interaction between HDDWs and cell boundaries with twin boundaries. Accordingly, we suggest that, in the present TWIP steel, deformation twins contain a high dislocation density as well. As the dislocation density is increased by dislocation storage through interactions, the dislocation density will increase with further deformation. These two aspects associated with the role of deformation twins, namely the arrangement in twin bundles and the high dislocation density within them, increase the stress required to transfer plastic deformation across deformation twins and therefore limit the further work hardening capacity at high strains in this material.

5. Conclusions

We have investigated the underlying defect topology and kinetics of substructure evolution and its correspondence to the strain hardening evolution of an Fe–22 wt.% Mn–0.6 wt.% C TWIP steel during tensile deformation by means of ECCI and EBSD. We draw the following conclusions:

- At the early stages of plastic deformation (below 0.1 true strain), the microstructure consists of dislocation cells and highly dense dislocation arrangements. These dislocation substructures are strong barriers to dislocation glide and result in a high strain hardening with a hardening coefficient of about $G/40$. This result underlines the importance of dislocation substructures at the early stages of strain hardening in TWIP steels.
- At intermediate strains (0.1–0.3 true strain), a well-defined deformation twin substructure is developed. Twinning depends on the crystallographic grain orientation. We classify the microstructure in this regime according to its twin substructure into three groups, referred to as types I, II and III. We quantify strain hardening in terms of a dislocation mean free path approach. The different microstructure parameters controlling strain hardening in this regime are: the average dislocation cell size in type I grains; the average twin spacing in type II grains; and the smallest average twin spacing of an active twin system in type III grains. The analysis shows that the refinement in the dislocation mean free path due to deformation twinning in type II and III grains results in a high strain rate with a hardening coefficient of about $G/30$.
- At high strains (above 0.4 true strain), the reduced further refinement of the dislocation and twin substructure together with the increasing strengthening effect of the individual deformation twins as obstacles to dislocation glide reduce the capability for trapping more dislocations, hence the strain hardening decreases.
- The cell structure formed in type I grains follows the similitude principle $\tau = \tau_0 + KGb/D$ with a similitude constant of $K = 3.7$. This value is smaller than the value of 7–8 that is typically observed in medium-to-high stacking fault alloys. We attribute this difference to the influence of the stacking fault energy on the mechanism of cell formation.

Acknowledgements

The authors would like to acknowledge the financial support by the German Research Foundation (Deutsche Forschungsgemeinschaft DFG) within the framework of the SFB 761 “steel ab initio”.

References

- [1] Grässel O, Krüger L, Frommeyer G, Meyer LW. *Int J Plast* 2000;16:1391.
- [2] Lü Y, Hutchinson B, Molodov DA, Gottstein G. *Acta Mater* 2010;58:3079.
- [3] Jin JE, Lee YK. *Mater Sci Eng A* 2009;527:157.
- [4] Kim JK, Chen L, Kim HS, Kim SK, Estrin Y, Cooman BCD. *Metall Mater Trans A* 2009;40:3147.
- [5] Curtze S, Kuokkala VT. *Acta Mater* 2010;58:5129.
- [6] Gutierrez-Urrutia I, Zaeferrer S, Raabe D. *Mater Sci Eng A* 2010;527:3552.
- [7] Idrissi H, Renard K, Schryvers D, Jacques PJ. *Scripta Mater* 2010;63:961.
- [8] Lü Y, Molodov DA, Gottstein G. *Acta Mater* 2011;59:3229.
- [9] Yoo JD, Park KT. *Mater Sci Eng A* 2008;496:417.
- [10] Yoo JD, Hwang SW, Park KT. *Metall Mater Trans A* 2009;40:1520.
- [11] Olson GB, Cohen M. *Metall Trans A* 1976;7:1897.
- [12] Olson GB, Cohen M. *Metall Trans A* 1976;7:1905.
- [13] Allain S, Chateau JP, Bouaziz O. *Mater Sci Eng A* 2004;387–389:143.
- [14] Shiekhelesouk MN, Favier V, Inal K, Cherkaoui M. *Int J Plast* 2009;25:105.
- [15] Bouaziz O, Allain S, Scott C. *Scripta Mater* 2008;58:484.
- [16] Barbier D, Gey N, Allain S, Bozzolo N, Humbert M. *Mater Sci Eng A* 2009;500:196.
- [17] Sevillano JG. *Scripta Mater* 2009;60:336.
- [18] Idrissi H, Renard K, Ryelandt L, Schryvers D, Jacques PJ. *Acta Mater* 2010;58:2464.
- [19] Ng BC, Simkin BA, Crimp MA. *Mater Sci Eng A* 1997;239–240:150.
- [20] Wilkinson AJ, Hirsch PB. *Micron* 1997;28:279.
- [21] Ng BC, Simkin BA, Crimp MA. *Ultramicroscopy* 1998;75:137.
- [22] Ahmed J, Roberts SG, Wilkinson AJ. *Philos Mag* 2006;86:4965.
- [23] Crimp MA. *Microsc Res Tech* 2006;69:374.
- [24] Gutierrez-Urrutia I, Zaeferrer S, Raabe D. *Scripta Mater* 2009;61:737.
- [25] Weidner A, Martin S, Klemm V, Martin U, Biermann H. *Scripta Mater* 2011;64:513.
- [26] Senk D, Emmerich H, Rezende J, Siquieri R. *Adv Eng Mater* 2007;9:695.
- [27] Raabe D, Sachtleber M, Zhao Z, Roters F, Zaeferrer S. *Acta Mater* 2001;49:3433.
- [28] Kocks UF, Mecking H. *Prog Mater Sci* 2003;48:171.
- [29] Ueji R, Tsuchida N, Terada D, Tsuji N, Tanaka Y, Takemura A, et al. *Scripta Mater* 2008;59:963.
- [30] Bay B, Hansen N, Hughes DA, Kuhlmann-Wilsdorf D. *Acta Metall Mater* 1992;40:205.
- [31] Hansen N. *Scripta Metall Mater* 1992;27:1447.
- [32] Hansen N, Jensen DJ. *Philos Trans Roy Soc* 1999;357:1447.
- [33] Canadinc D, Sehitoglu H, Maier HJ, Chumlyakov YI. *Acta Mater* 2005;53:1831.
- [34] Canadinc D, Sehitoglu H, Maier HJ. *Mater Sci Eng A* 2007;454–455:662.
- [35] Gerold V, Karnthaler HP. *Acta Metall* 1989;37:2177.
- [36] Hong SI, Laird C. *Acta Metall Mater* 1990;38:1581.
- [37] Kassner ME, Miller AK, Sherby OD. *Metall Trans A* 1982;13:1977.
- [38] Lo KH, Shek CH, Lai JKL. *Mater Sci Eng R* 2009;65:39.
- [39] Bracke L, Kestens L, Penning J. *Scripta Mater* 2009;61:220.
- [40] Kuhlmann-Wilsdorf D. *Mater Sci Eng A* 1989;113:1.
- [41] Hansen N, Huang X. *Acta Mater* 1998;46:1827.
- [42] Winther G, Jensen DJ, Hansen N. *Acta Mater* 1997;45:5059.
- [43] Mitchell TE, Hirth JP. *Acta Metall Mater* 1991;39:1711.
- [44] Kamat SV, Hirth JP, Müllner P. *Philos Mag A* 1996;73:669.
- [45] Müllner P, Solenthaler C, Speidel MO. *Acta Metall Mater* 1994;42:1727.
- [46] Christian JW, Mahajan S. *Prog Mater Sci* 1995;39:1.
- [47] Niewczas M. In: Nabarro FRN, Hirth JP, editors. *Dislocations in solids*, vol. 13. Amsterdam: Elsevier B.V.; 2007.
- [48] Hirth JP, Lothe J. *Theory of dislocations*. 2nd ed. New York: John Wiley and Sons; 1982.
- [49] Sauzay M, Kubin LP. *Prog Mater Sci* 2011;56:725.
- [50] Feaugas X. *Acta Mater* 1999;47:3617.
- [51] Jackson PJ. *Prog Mater Sci* 1985;29:139.
- [52] Asgari S, El-Danaf E, Kalidindi SR, Doherty RD. *Metall Mater Trans A* 1997;28:1781.
- [53] Karaman I, Sehitoglu H, Maier HJ, Chumlyakov YI. *Acta Mater* 2001;49:3919.

Viewpoint Paper

Grain size effect on strain hardening in twinning-induced plasticity steels

I. Gutierrez-Urrutia* and D. Raabe

Max-Planck-Institut für Eisenforschung, Max-Planck Str. 1, D-40237 Düsseldorf, Germany

Available online 28 January 2012

Abstract—We investigate the influence of grain size on the strain hardening of two Fe–22Mn–0.6C (wt.%) twinning-induced plasticity steels with average grain sizes of 3 and 50 μm , respectively. The grain size has a significant influence on the strain hardening through the underlying microstructure. The dislocation substructure formed in the early deformation stages determines the density of nucleation sites for twins per unit grain boundary area which controls the developing twin substructure.

© 2012 Acta Materialia Inc. Published by Elsevier Ltd. All rights reserved.

Keywords: TWIP steels; Plastic deformation; Dislocation structure; Twinning; Scanning electron microscopy (SEM)

TWIP (twinning-induced plasticity) steels have been the object of much interest in recent years due to their outstanding mechanical properties at room temperature combining high strength (ultimate tensile strength up to 800 MPa) and ductility (elongation to failure up to 100%) based on a high work-hardening capacity [1–5]. TWIP steels are typically austenitic steels, i.e. face-centered cubic (fcc) alloys, with a high Mn content (above 20 wt.%) and additions of elements such as carbon (<1 wt.%), silicon (<3 wt.%) or aluminum (<10 wt.%). The TWIP mechanism is observed in medium stacking fault energy steels (20–40 mJ m^{-2}) and is characterized by the formation of nanometer-thick deformation twins. The strain hardening is commonly analyzed in terms of the dislocation mean free path (MFP) approach, focusing essentially on a single microstructure parameter, namely the twin spacing [3,6,7]. These works attribute the high strain-hardening rate at intermediate strains (0.1–0.2 true strain) to twin spacing refinement. As twin boundaries are major obstacles to dislocation glide, the increasing density of deformation twin boundaries with further deformation leads to the so-called “dynamic Hall–Petch effect”. However, as we have recently shown in Ref. [4], this concept conveys an overly simplistic picture of the strain-hardening behavior. High-manganese TWIP steels are characterized by a hierarchical microstructure refinement involving different dislocation substructure sizes and twin spacings, which are determined by the stress level. At

the early stages of deformation (below 0.1 true strain), the microstructure consists of dislocation cells and cell blocks containing highly dense dislocation walls. These dislocation substructures are major barriers to dislocation glide resulting in an early high strain hardening. At intermediate strains (0.1–0.3 true strain), a well-defined twin substructure is developed. As twinning depends strongly on the crystallographic grain orientation, the resulting deformed microstructure is a complex mixture of dislocation and twin substructures. At this strain level, different microstructure parameters control strain hardening, such as the average dislocation cell size and twin spacing.

However, it is not only crystallographic orientation that has a strong influence on deformation twinning; grain size also plays a part. Only a few studies have addressed the influence of grain size on deformation twinning in TWIP steels [8–10]. For instance, we recently observed [9] that the influence of grain size on the twinning stress within the micrometer grain size range in a Fe–22Mn–0.6C (wt.%) TWIP steel can be explained in terms of a Hall–Petch relation. It is thus clear that there are still some details that remain unclear regarding the influence of grain size on the strain-hardening behavior in TWIP steels, in particular its role on the twin substructure. The present study aims at elucidating the influence of grain size on the strain-hardening behavior of a Fe–22Mn–0.6C TWIP steel. We analyze the role of grain size on the corresponding dislocation and twin substructures. Detailed microstructural observations by electron channeling contrast imaging (ECCI) were performed on two

* Corresponding author. Tel.: +49 2116792 407; e-mail: i.gutierrez@mpie.de

types of tensile samples deformed to different strain levels at room temperature. The specimens had average grain sizes of 3 and 50 μm , respectively.

The TWIP steels used in this study had the chemical composition Fe–22Mn–0.6C (wt.%). The material was melted in an induction furnace under Ar atmosphere and cast into round bars of 25 mm in diameter. Samples were swaged to 20% area reduction at 1000 °C and subsequently solution treated for 4 h at 1100 °C under Ar. Thereafter, samples were hot-rolled to 75% thickness reduction at 1000 °C, followed by air cooling. To obtain samples with different grain sizes, the hot-rolled steel was then cold rolled to 70% thickness reduction and annealed at 700 °C for different times. We obtained fully recrystallized steels with average grain sizes of 3 μm (referred to as FG-steel) and 50 μm (referred to as LG-steel) after annealing times of 5 and 15 min, respectively. The steels showed a fully austenitic structure which remained stable during deformation at room temperature. No evidence of ϵ -martensite was detected by electron back-scatter diffraction (EBSD) on the tensile deformed samples. Tensile tests were performed at room temperature at an initial strain rate of 10^{-4} s^{-1} to different strain levels. The mechanical tests were carried out on a tensile test instrument (Kammrath & Weiss GmbH, Dortmund, Germany) equipped with a digital image correlation (DIC) system (ARAMIS system, GOM-Gesellschaft für Optische Messtechnik mbH, Braunschweig, Germany) to measure the local and macroscopic strain distribution. Details of this set-up are described in Ref. [11]. The surface pattern required for DIC was obtained as explained in Ref. [9]. Averaged engineering strain values were retrieved from the corresponding strain maps and used to calculate the true stress–strain values. Dislocation and twin substructures were characterized by ECCI after orienting the crystal into the Bragg condition using a high-intensity reflection. We used a new recently reported EBSD-based ECCI set-up [12] that allows ECCI images to be obtained under controlled diffraction conditions with enhanced dislocation contrast. This ECCI set-up has been successfully used in the imaging and quantification of dislocation substructures in Fe-based alloys [4,9,13]. ECCI observations were carried out in a dual-beam Zeiss-Crossbeam instrument (Carl Zeiss SMT AG, Germany) consisting of a Gemini-type field emission gun (FEG) electron column and a focused ion beam device (Orsay Physics FIB). This instrument is equipped with an EBSD system (EDAX/TSL, Draper, UT, USA). ECCI was performed at 10 kV acceleration voltage and a working distance of 6 mm, using a solid-state four-quadrant BSE detector.

Figure 1a shows the true stress–strain curves of the Fe–22Mn–0.6C (wt.%) TWIP steels with average grain sizes of 50 μm (LG-steel) and 3 μm (FG-steel) tensile deformed at an initial strain rate of 10^{-4} s^{-1} . Figure 1a shows that the grain size has a significant influence on the yield stress. This can be explained by the Hall–Petch relation: $\sigma_y = \sigma_0 + K_{tw}^{H-P} / \sqrt{D}$, where σ_y is the yield stress, σ_0 is the friction stress, K_{tw}^{H-P} is a constant, and D is the initial grain size. Using appropriate values of the constants [9], we obtain yield stresses of 207 and 360 MPa for the LG-steel and FG-steel, respectively. These stresses are close to the experimental values of 210 and 330 MPa.

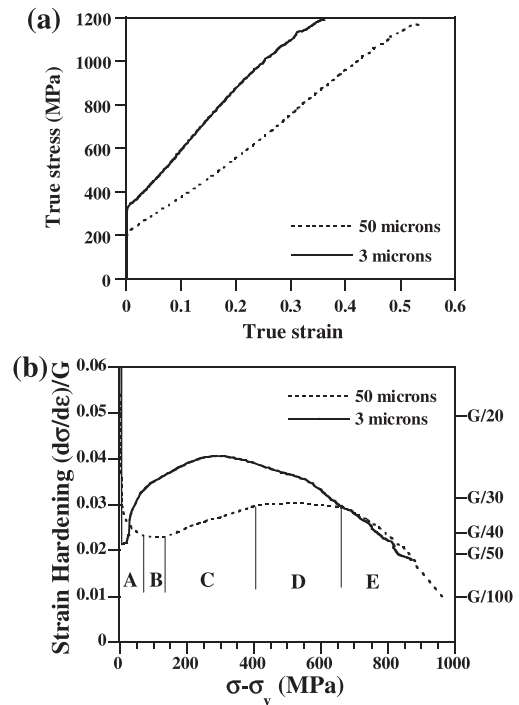


Figure 1. (a) True stress–true strain curves of the Fe–22Mn–0.6C (wt.%) TWIP steels with average grain sizes of 50 μm (referred to as LG-steel) and 3 μm (referred to as FG-steel) tensile deformed at an initial strain rate of 10^{-4} s^{-1} . (b) Normalized strain-hardening rate (normalized by the shear modulus) vs. flow stress subtracted by the yield stress of the tensile deformed TWIP steels.

Figure 1b shows the normalized strain-hardening rate (normalized by the shear modulus) vs. flow stress subtracted by the yield stress, $\sigma - \sigma_y$, of the tensile deformed TWIP steels. The strain hardening of the LG-steel has been analyzed in detail in Ref. [4], and accordingly only the main aspects will be discussed here. The LG-steel exhibits five different deformation stages. The first stage, stage A hardening, is characterized by a continuous decrease in the strain-hardening rate. This stage is ascribed to the prevalence of dynamic recovery processes such as cross-slip and annihilation of screw dislocations of opposite signs. The second stage, Stage B hardening, which is characterized by a constant strain-hardening rate with a hardening coefficient of about $G/40$ (where G is the shear modulus), is attributed to dislocation substructure hardening. The development of a dense twin substructure upon straining results in a further drastic refinement of the dislocation mean free path (MFP). Consequently, strain hardening increases up to a hardening coefficient of about $G/30$, stage C hardening. With further straining, the reduced additional refinement of the dislocation and twin substructures, together with the increasing strengthening effect of the individual deformation twins as obstacles to dislocation glide, reduce the capability for trapping more dislocations and, hence, the strain hardening decreases (stages D and E). It is interesting to note that the onset of the high strain-hardening stage of the FG-steel occurs at a value of $\sigma - \sigma_y$ of 20 MPa, which is roughly 120 MPa smaller than the onset of stage C hardening of the LG-steel. As the

yield stress, σ_y , of the FG-steel is about 120 MPa higher than that of the LG-steel, this indicates that both hardening stages occur at the same macroscopic stress level. ECCI images of deformed microstructure of the FG-steel deformed to strain/stress levels ranged between 0.03 true strain/390 MPa and 0.2 true strain/860 MPa (Fig. 2b and c), confirm that the high strain-hardening rate of the FG-steel is due to microstructure refinement by deformation twinning. According to the previous classification of hardening stages in TWIP steels, the FG-steel exhibits only four different deformation stages, namely stages A, C, D and E. It is interesting to note the main features revealed in the strain-hardening curves of the TWIP steels (Fig. 1b). These are, first, the rapid increase in strain hardening in the FG-steel immediately after yielding, i.e. the absence of stage B hardening; and second, the significantly higher stage C hardening of the FG-steel (strain-hardening coefficient of about $G/25$). The absence of stage B hardening in the FG-steel implies that the refinement of the mean free path by deformation

twinning occurs at a strain level just slightly higher than the onset of yielding. However, the higher strain hardening associated with deformation twinning observed in the FG-steel, i.e. stage C hardening, deserves more detailed analysis of the underlying deformation microstructure.

The ECCI image of Figure 2a shows the deformed microstructure of the FG-steel strained to 0.03 true strain, stage C hardening. Under the current diffraction conditions, the crystal matrix appears dark and dislocations appear as sharp bright lines due to the electron channeling mechanism [14]. Figure 2a reveals that the deformed microstructure consists of loose dislocation arrangements. This dislocation substructure is very different from that observed in the LG-steel at the onset of stage C hardening (Fig. 3a and b). These figures show ECCI images of the dislocation substructure at 0.1 true strain in cross section. Figure 3a and b correspond to crystals oriented close to the $\langle 001 \rangle$ //tensile axis and $\langle 112 \rangle$ //tensile axis, respectively. Figure 3a shows that

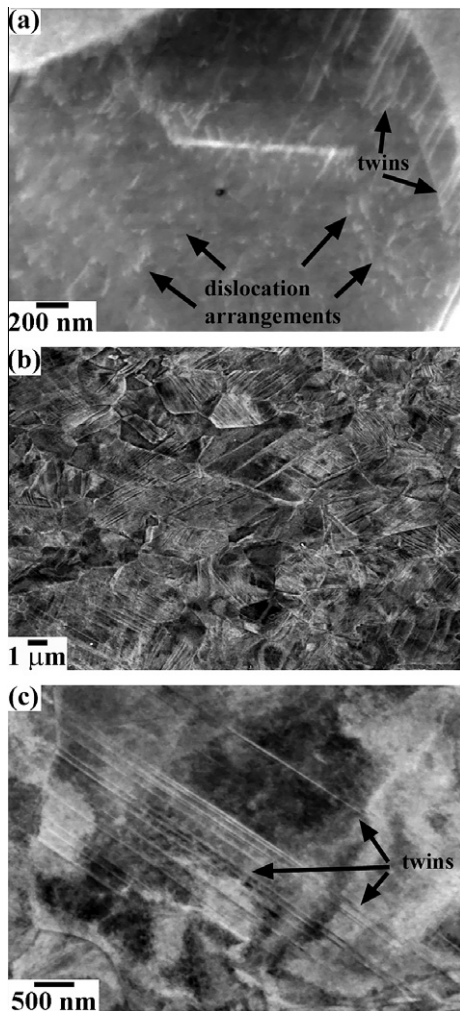


Figure 2. ECCI images of deformed microstructure of the FG-steel. (a) Loose dislocation arrangements and deformation twins nucleated at grain boundaries on a sample tensile deformed to 0.03 true strain. Corresponding features are indicated by arrows. (b) Twin substructure of a sample tensile deformed to 0.2 true strain. (c) Detail of lamellar twin structure in a sample deformed at a true strain of 0.2.

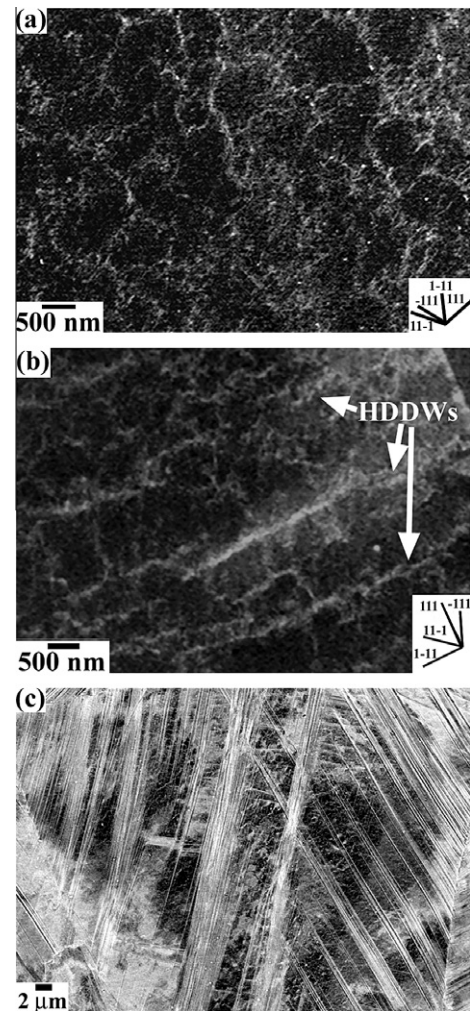


Figure 3. ECCI images of deformed microstructure of the LG-steel. (a) Dislocation cells (DCs) in a sample deformed at a true strain of 0.1, cross-section view. (b) Cell-block structure delimited by highly dense dislocation walls (HDDWs) in a sample deformed at a true strain of 0.1, cross-section view. Corresponding features are indicated by arrows. (c) Detail of multiple twin structure in a sample deformed at a true strain of 0.3.

the dislocation substructure of the first crystal consists of equiaxed dislocation cells (DCs). These structures appear under the current Bragg condition using a high-intensity reflection of $\{111\}$ -type as bright globular structures with a sharp boundary contrast. The second crystal contains cell blocks mainly delimited by highly dense dislocation walls (HDDWs). These boundaries appear as straight and extended bright compact layers (indicated by arrows in the figure). This morphology corresponds to planar dislocation substructures commonly found in low-to-medium stacking fault energy metals [15,16]. In this case, only one set of HDDWs is observed. The dislocation patterns shown in Figure 3a and b are similar to those observed by bright-field TEM in medium-to-high stacking fault energy alloys [15–17]. However, the contrast in ECCI imaging is inverted compared to that obtained in bright-field TEM due to the electron channeling mechanism and the diffraction conditions used to image dislocation substructures. These dislocation substructures are ascribed to the multiple character of slip, namely wavy and planar. Wavy dislocation structures are promoted in grains when a high number of slip planes are activated and dislocation cross-slip is enabled [17]. Planar dislocation substructures in the present TWIP steel are associated with the high friction stress (157 MPa [7], which is higher than for materials exhibiting planar slip such as stainless steels [18]), and low stacking fault energy (22 mJ m^{-2} [19]).

ECCI images further reveal that TWIP steels develop different twin substructures in the C strain-hardening regime (Fig. 1). At 0.2–0.3 true strain, the twin substructure of the FG-steel is formed roughly equally by twin substructures containing either one or two active twin systems (determined from ECCI images of about 200 grains) (Fig. 2b). Figure 2c shows an example of lamellar twin structure in the FG-steel at a true strain of 0.2. However, at the same strain level, the twin substructure of the LG-steel mainly consists of two active twin systems [4] (two twin systems: 60% grain area fraction, one twin system: 30% grain area fraction, no twins: 10% grain area fraction). Figure 3c shows an example of multiple twin structure in the LG-steel at a true strain of 0.3.

These observations suggest that grain size has a significant influence on the deformed microstructure over the entire deformation range. The influence of grain size on the dislocation substructure formed at the early deformation stage, stage B hardening, can be understood in terms of the Hall–Petch relation. Due to the low yield stress, the LG-steel requires a larger strain to achieve the macroscopic stress associated to stage C hardening (0.1 true plastic strain). At this deformation stage, dislocation glide mainly controls plasticity and, accordingly, the dislocation density scales with strain. The high dislocation density in the LG-steel is mainly accumulated in the form of DCs and cell blocks delimited by HDDWs (Fig. 3a and b). However, due to the higher yield stress, the FG-steel stores a lower dislocation density before the onset of stage C hardening. The dislocation density in this deformation regime is accumulated in the form of loose dislocation arrangements (Fig. 2a).

The influence of grain size on the twin substructure is depicted in Figure 4. It can be rationalized as follows. First, the dislocation substructure formed during the

early deformation stages (Fig. 4a and b) determines the density of nucleation sites for twins per unit grain boundary area. Second, the nucleation site density accounts for the evolving twin substructure (Fig. 4c and d). Deformation twinning can be considered as a nucleation and growth process [20]. Nucleation of deformation twins proceeds by specific dislocation reactions which are required for twin growth. There are several proposed dislocation reaction mechanisms in the literature. Basically, they can be divided into two groups: mechanisms which suggest a direct dislocation dissociation process under the action of a certain stress (pole mechanism [21]); and those mechanisms involving specific dislocation interactions with Lomer–Cottrell locks (perfect dislocations [22,23] or pile-ups of extended dislocations [24]). In particular, recent TEM observations in high-Mn steels [25,26] support those models involving dislocation interactions with Lomer–Cottrell locks. We further assume that grain boundaries are the main sites of twin nucleation in the present TWIP steels. High-resolution ECCI reveals that other intragranular interfaces, such as twin boundaries, act as twin nucleation sites only at high macroscopic stress levels. If we consider that twin nucleation is controlled by specific dislocation reactions, the rather homogeneous dislocation distribution of the FG-steel (Fig. 4a) provides a high number of nucleation sites for twins per unit grain boundary. On the other hand, the LG-steel contains a high overall dislocation density mainly distributed along the boundaries of the dislocation substructure, namely dislocation cell walls and HDDWs. As cell-forming crystals do not twin upon deformation [4], we only consider those crystals containing cell block structures mainly delimited by HDDWs (Fig. 4b). This dislocation substructure creates a lower number of nucleation sites

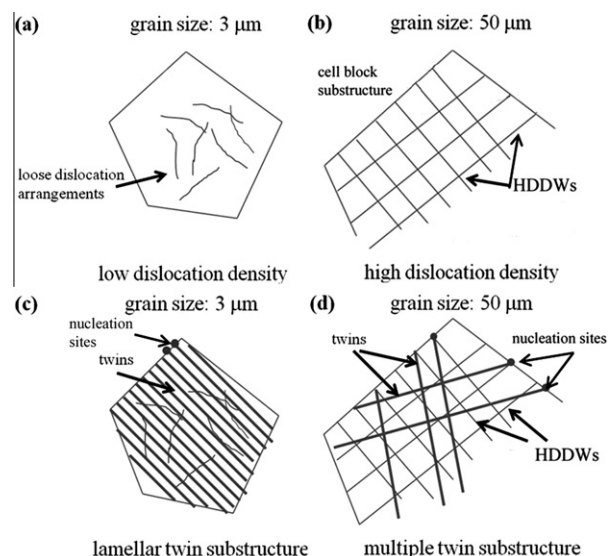


Figure 4. Schematic illustration of the influence of grain size on twin substructure in TWIP steels. (a, b) Effect of grain size on the dislocation substructure formed at the early deformation stages. (c, d) Effect of dislocation substructure on the density of nucleation sites for twins per unit grain boundary area, which controls the developing twin substructure. HDDWs, highly dense dislocation walls.

for twins per unit grain boundary. In other words, grain size has a negative effect on the number of twins per unit grain boundary area. This agrees with recent observations on Mg and Ti [27]. However, if we consider that the grain boundary area per unit volume is equal to $2/D$ (where D is the grain size), and assuming that twins are spheroids, Ghaderi and Barnett [27] have shown that a higher density of twin nucleation events per unit grain boundary area does not result in a higher twin volume fraction due to twin size effects (twin length and thickness are grain size dependent).

Twin growth proceeds by co-operative movement of Shockley partials on subsequent $\{111\}$ planes, i.e. it is a stress-controlled process. A high density of twins per unit grain boundary area promotes the formation of a lamellar twin structure. This is due to the high local stress that would be required to push a second twin system through the existing lamellar twin structure containing an already high density of twin boundaries. If we consider here the crystallographic grain orientation, this effect is expected to be more relevant in crystal orientations where the Schmid factors for twinning on the two most favorable systems are similar. This means that lamellar twin structure is enabled in the FG-steel (Fig. 4c). On the other hand, a low density of twins per unit grain boundary area enables the formation of multiple twin structures due to the lower number of twin–twin interactions. Accordingly, a multiple twin structure is enhanced in the LG-steel (Fig. 4d). As we have shown in Ref. [4], the mean free path refinement by deformation twinning is responsible for the high strain hardening of TWIP steels. In particular, the formation of a lamellar twin structure is the most effective way to increase the strain hardening due to the small twin spacing. As a lamellar twin structure is promoted particularly in the FG-steel, the strain-hardening level in this material increases as well, as Figure 1b shows.

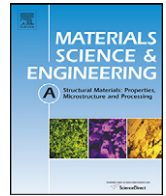
In summary, we have investigated the effect of grain size on the strain-hardening behavior in two Fe–22Mn–0.6C (wt.%) TWIP steels with average grain sizes of 3 μm (FG-steel) and 50 μm (LG-steel) by ECCI. We observe a strong influence of grain size on the strain-hardening behavior. This is ascribed to the microstructure formed upon straining, namely the dislocation substructure formed in the early deformation stages and the evolving twin substructure. The early dislocation substructure determines the density of nucleation sites for twins per unit grain boundary area, which controls the developing twin substructure.

Acknowledgments

The authors would like to acknowledge the financial support by the German Research Foundation in the framework of SFB 761 “steel ab initio”.

References

- [1] O. Grässel, L. Krüger, G. Frommeyer, L.W. Meyer, *Int. J. Plast.* 16 (2000) 1391.
- [2] S. Curtze, V.T. Kuokkala, *Acta Mater.* 58 (2010) 5129.
- [3] O. Bouaziz, S. Allain, C.P. Scott, P. Cugy, D. Barbier, *Curr. Opin. Solid State Mater. Sci.* 15 (2011) 141.
- [4] I. Gutierrez-Urrutia, D. Raabe, *Acta Mater.* 59 (2011) 6449.
- [5] S.J. Lee, J. Kim, S.N. Kane, B.C. De Cooman, *Acta Mater.* 59 (2011) 6809.
- [6] M.N. Shiekhelsouk, V. Favier, K. Inal, M. Cherkaoui, *Int. J. Plast.* 25 (2009) 105.
- [7] J. Gil Sevillano, *Scripta Mater.* 60 (2009) 336.
- [8] R. Ueji, N. Tsuchida, D. Terada, N. Tsuji, Y. Tanaka, A. Takemura, K. Kunishige, *Scripta Mater.* 59 (2008) 963.
- [9] I. Gutierrez-Urrutia, S. Zaefferer, D. Raabe, *Mater. Sci. Eng. A* 527 (2010) 3552.
- [10] G. Dini, A. Najafizadeh, R. Ueji, S.M. Monir-Vaghefi, *Mater. Des.* 31 (2010) 3395.
- [11] D. Raabe, M. Sachtleber, Z. Zhao, F. Roters, S. Zaefferer, *Acta Mater.* 49 (2001) 3433.
- [12] I. Gutierrez-Urrutia, S. Zaefferer, D. Raabe, *Scripta Mater.* 61 (2009) 737.
- [13] I. Gutierrez-Urrutia, D. Raabe, *Scripta Mater.* (2012), doi:10.1016/j.scriptamat.2011.11.027.
- [14] A.J. Wilkinson, P.B. Hirsch, *Micron* 28 (1997) 279.
- [15] X. Huang, *Scripta Mater.* 38 (1998) 1697.
- [16] D. Canadinc, H. Sehitoglu, H.J. Maier, Y.I. Chumlyakov, *Acta Mater.* 53 (2005) 1831.
- [17] B. Bay, N. Hansen, D.A. Hughes, D. Kuhlmann-Wilsdorf, *Acta Metall. Mater.* 40 (1992) 205.
- [18] K.H. Lo, C.H. Shek, J.K.L. Lai, *Mater. Sci. Eng. R* 65 (2009) 39.
- [19] L. Bracke, L. Kestens, J. Penning, *Scripta Mater.* 61 (2009) 220.
- [20] J.W. Christian, S. Mahajan, *Prog. Mater. Sci.* 39 (1995) 1.
- [21] J.A. Venables, *Philos. Mag.* 6 (1961) 379.
- [22] S. Mahajan, G.Y. Chin, *Acta Metall.* 21 (1973) 1353.
- [23] J.B. Cohen, J. Weertman, *Acta Metall.* 11 (1963) 996.
- [24] S. Miura, J. Takamura, N. Narita, *Trans. Jpn. Inst. Met.* 9 (1968) 555.
- [25] I. Karaman, H. Sehitoglu, K. Gall, Y.I. Chumlyakov, H.J. Maier, *Acta Mater.* 48 (2000) 1345.
- [26] H. Idrissi, K. Renard, L. Ryelandt, D. Schryvers, P.J. Jacques, *Acta Mater.* 58 (2010) 2464.
- [27] A. Ghaderi, M.R. Barnett, *Acta Mater.* 59 (2011) 7824.



The effect of grain size and grain orientation on deformation twinning in a Fe–22 wt.% Mn–0.6 wt.% C TWIP steel

I. Gutierrez-Urrutia*, S. Zaefferer, D. Raabe

Max-Planck-Institut für Eisenforschung, Max-Planck Str. 1, D-40237 Düsseldorf, Germany

ARTICLE INFO

Article history:

Received 14 December 2009

Received in revised form 10 February 2010

Accepted 11 February 2010

Keywords:

EBSD

Mechanical characterization

Steel

Twinning

ABSTRACT

We investigate the effect of grain size and grain orientation on deformation twinning in a Fe–22 wt.% Mn–0.6 wt.% C TWIP steel using microstructure observations by electron channeling contrast imaging (ECCI) and electron backscatter diffraction (EBSD). Samples with average grain sizes of 3 μm and 50 μm were deformed in tension at room temperature to different strains. The onset of twinning concurs in both materials with yielding which leads us to propose a Hall–Petch-type relation for the twinning stress using the same Hall–Petch constant for twinning as that for glide. The influence of grain orientation on the twinning stress is more complicated. At low strain, a strong influence of grain orientation on deformation twinning is observed which fully complies with Schmid's law under the assumption that slip and twinning have equal critical resolved shear stresses. Deformation twinning occurs in grains oriented close to $\langle 111 \rangle$ /tensile axis directions where the twinning stress is larger than the slip stress. At high strains (0.3 logarithmic strain), a strong deviation from Schmid's law is observed. Deformation twins are now also observed in grains unfavourably oriented for twinning according to Schmid's law. We explain this deviation in terms of local grain-scale stress variations. The local stress state controlling deformation twinning is modified by local stress concentrations at grain boundaries originating, for instance, from incoming bundles of deformation twins in neighboring grains.

© 2010 Elsevier B.V. All rights reserved.

1. Introduction

TWIP (twinning-induced plasticity) steels have received high interest in recent years due to their outstanding mechanical properties at room temperature combining high strength (ultimate tensile strength of up to 800 MPa) and ductility (elongation to failure up to 100%) based on a high work-hardening capacity [1–3]. TWIP steels are austenitic steels, i.e. face-centered cubic (fcc) metals, with high content in Mn (above 20% in weight %) and small additions of elements such C (<1 wt.%), Si (<3 wt.%), or Al (<3 wt.%). The steels have low stacking fault energy (between 20 and 40 mJ/m² [3–5]) at room temperature. Although the details of the mechanisms controlling strain-hardening in TWIP steels are still unclear, the high strain-hardening is commonly attributed to the reduction of the dislocation mean free path with the increasing fraction of deformation twins as these are considered to be strong obstacles to dislocation glide [3,6–8]. Therefore, a quantitative study of deformation twinning in TWIP steels is critical to understand their strain-hardening mechanisms and mechanical properties. Deformation twinning can be considered as a nucleation and growth process [9]. Twin growth is assumed to proceed by co-operative

movement of Shockley partials on subsequent $\{111\}$ planes. Possible mechanisms for the co-operative movement are the pole mechanism [10], a cross-slip mechanism [11] or the reaction between primary and secondary slip systems [12,13]. Nucleation of deformation twins, on the other hand, consists in the formation of the dislocation structures required for twin growth and a number of experimental observations suggest mechanisms for that [9,14,15]. Dislocation slip is therefore a prerequisite for twin formation. The stress required to produce twins in a microstructure, generally termed as twinning stress, is a mixture of the stress for twin nucleation and that for growth. However, as the experimental determination of the stress needed for twin nucleation is very difficult to accomplish [9], it is commonly assumed that the twin nuclei already exist and, hence, only the stress for twin growth can be experimentally measured which is generally identified as the twinning stress. As the growth of a deformation twin is controlled by the glide of Shockley partials, it is reasonable to assign a critical resolved shear stress on the slip plane to this process that must be reached to move the twinning dislocations leading to the deformation twinning. For the same material in an undeformed state, the main parameters that may influence the twinning stress and, hence, the twinning microstructure, are grain size and grain orientation. Only few studies have addressed the influence of these microstructural parameters on deformation twinning in TWIP steels [5,16,17]. Ueji et al. [5] reported a strong

* Corresponding author. Tel.: +49 2116792 211.

E-mail address: i.gutierrez@mpie.de (I. Gutierrez-Urrutia).

influence of grain size on deformation twinning in a Fe–31 wt.% Mn–3.0 wt.% Al–3.0 wt.% Si TWIP steel. They observed that deformation twinning is strongly inhibited for an average grain size of 1.8 μm suggesting that deformation twinning in TWIP steels becomes difficult as the grain size decreases to a certain scale. Yang et al. [16] and Meng et al. [17] reported a strong influence of grain orientation on twinning behavior in a Fe–33 wt.% Mn–3.0 wt.% Al–3.0 wt.% Si TWIP steel. They found that deformation twinning is favored during tension because the grains rotate towards the $\langle 111 \rangle$ /tensile axis which renders the crystals favorably oriented for twinning (high Schmid factor) whereas deformation twinning is suppressed during compression because the grains rotate towards the $\langle 101 \rangle$ axis which renders them unfavorably oriented for twinning (small Schmid factor). However, there are still some details that remain unclear regarding the influence of grain size and grain orientation on twinning behaviour in TWIP steels, in particular their role on the twinning stress. The aim of this report is to investigate in detail the influence of grain size and grain orientation on the twinning behavior in a Fe–22 wt.% Mn–0.6 wt.% C TWIP steel. Detailed microstructural observations by electron channeling contrast imaging (ECCI) and electron backscatter diffraction (EBSD) were performed on tensile deformed samples at room temperature to different strains with average grain sizes of 3 μm and 50 μm . Further analyses based on stress–strain curves and deformed microstructures were carried out to illustrate the effect of grain size and grain orientation on the twinning stress.

2. Experimental details

The TWIP steel used in this study had the chemical composition Fe–22 wt.% Mn–0.6 wt.% C. The material was melted in an induction furnace under Ar atmosphere and cast to round bars of 25 mm diameter. To avoid Mn segregation [18] samples were swaged to 20% area reduction at 1000 °C and subsequently solution-treated for 4 h at 1100 °C under Ar. Thereafter, samples were hot-rolled to 75% reduction in thickness at 1000 °C followed by air cooling. The hot-rolled material was then cold rolled to 70% thickness reduction. In order to obtain different grain sizes, the material was finally annealed at 700 °C for 5 or 15 min resulting in material with average grain size of 3 μm (referred to as steel FG) and 50 μm (referred to as steel LG), respectively. Tensile tests were carried out at room temperature at a strain rate of $5 \times 10^{-4} \text{ s}^{-1}$ to different strains. The tensile bone-shaped samples had 8 mm gage length, 2 mm gage width and 1 mm gage thickness. The monotonic tensile deformation experiments were carried out on a tensile test instrument Kammrath & Weiss GmbH (44141 Dortmund, Germany) equipped with a digital image correlation (DIC) system (ARAMIS system, GOM-Gesellschaft für Optische Messtechnik mbH, 38106 Braunschweig, Germany) to measure the local and macroscopic strain distribution. Details of this setup are described in [19–22]. The surface pattern required for DIC was obtained by applying two different colour sprays on the sample surface. Firstly, a white spray was used to obtain a homogeneous background and thereafter, a black spray was applied to obtain a spotted pattern. Averaged engineering strain values are obtained from the corresponding maps and utilized to calculate the logarithmic stress–strain values.

Deformation microstructures of the tensile deformed TWIP steels were examined by two scanning electron microscopy techniques: electron back scatter diffraction (EBSD) and electron channeling contrast (ECCI). The EBSD technique was used to analyze the local texture in relation with the microstructure. Orientation maps were performed in a 6500 F JEOL field emission gun-scanning electron microscope (FEG-SEM) equipped with a TSL

OIM EBSD system. EBSD maps were measured at 15 kV acceleration voltage and a working distance of 15 mm. The ECCI technique has been recently proven as a powerful technique to image deformation twins and even dislocation structures in TWIP steels by using a SEM [23]. A new recently reported setup for ECCI [23] was used in this study to obtain ECCI images under controlled diffraction conditions with enhanced dislocation and interface contrast. ECCI observations were carried out in a Zeiss Crossbeam instrument (XB 1540, Carl Zeiss SMT AG, Germany) consisting of a Gemini-type field emission gun (FEG) electron column and an focused ion beam (FIB) device (Orsay Physics). ECCI was performed at 10 kV acceleration voltage and a working distance of 6 mm, using a solid-state 4-quadrant BSE detector. The microscope was run in the “high current” mode and an objective lens aperture of 120 μm was used.

3. Results

3.1. Effect of grain size

The initial hot-rolled state of both materials (LG and FG) showed a fully austenitic structure which remained stable during deformation. No evidence of ϵ -martensite was detected by EBSD. The initial hot-rolled textures on both materials were weak, and during tensile deformation both steels developed similar deformation textures which are shown below. The similarity of deformation textures allows us to analyze the influence of grain size on deformation twinning by examining the deformation microstructures in samples LG and FG at similar strain levels.

The ECCI technique was found to be an excellent tool in examining deformation microstructures of TWIP steels. The onset of deformation twinning in steel LG was observed at a logarithmic strain of 0.03. At this strain level the twin fraction was very small (twin area fraction less than 0.001 determined from ECCI pictures of around 100 grains) and only few grains, less than 20%, contained deformation twins. In most of these grains only one twinning system (primary system) was activated. Fig. 1(a) shows an ECCI image of the microstructure of steel LG tensile deformed to 0.03 logarithmic strain. Grains containing deformation twins up to 50 μm in length and 0.5 μm in thickness, which are nucleated at grain boundaries, are visible. This ECCI image was obtained by orienting the grain in the centre of the image into Bragg condition for the diffraction vector $g: (1\bar{1}1)$. Under this diffraction condition, details of deformed microstructure such as deformation twins, orientation gradients (grey areas), and even dislocation structures can be identified at optimum contrast. At higher magnification it is further observed that deformation twins are not single but bundles consisting of thinner twins, as shown in Fig. 1(b). For this ECCI image optimum contrast was achieved by tilting the sample such as to excite the (002) diffraction vector of the twins in a “two-beams” condition. It is observed that the bundle, around 0.5 μm thick, consists of six thin twins (dark straight lines) with thickness values ranging from 30 nm to 200 nm. Increasing the strain to a logarithmic strain of 0.3 lead to a significant increase in the twin area fraction from zero to around 0.2, Fig. 1(c). Almost all the grains contained deformation twins activated in several systems (up to three activated twinning systems were observed in the same grain) and only less than 10% of the grains contained no twins. The microstructure was very heterogeneous consisting of grains with only the primary twinning system activated, grains with more than one twinning system activated (primary and secondary twinning systems), and grains with no twins.

Deformation twins were also observed by ECCI in steel FG deformed to low strains. Fig. 2(a) shows an ECCI image of the microstructure of steel FG deformed to 0.04 logarithmic strain.

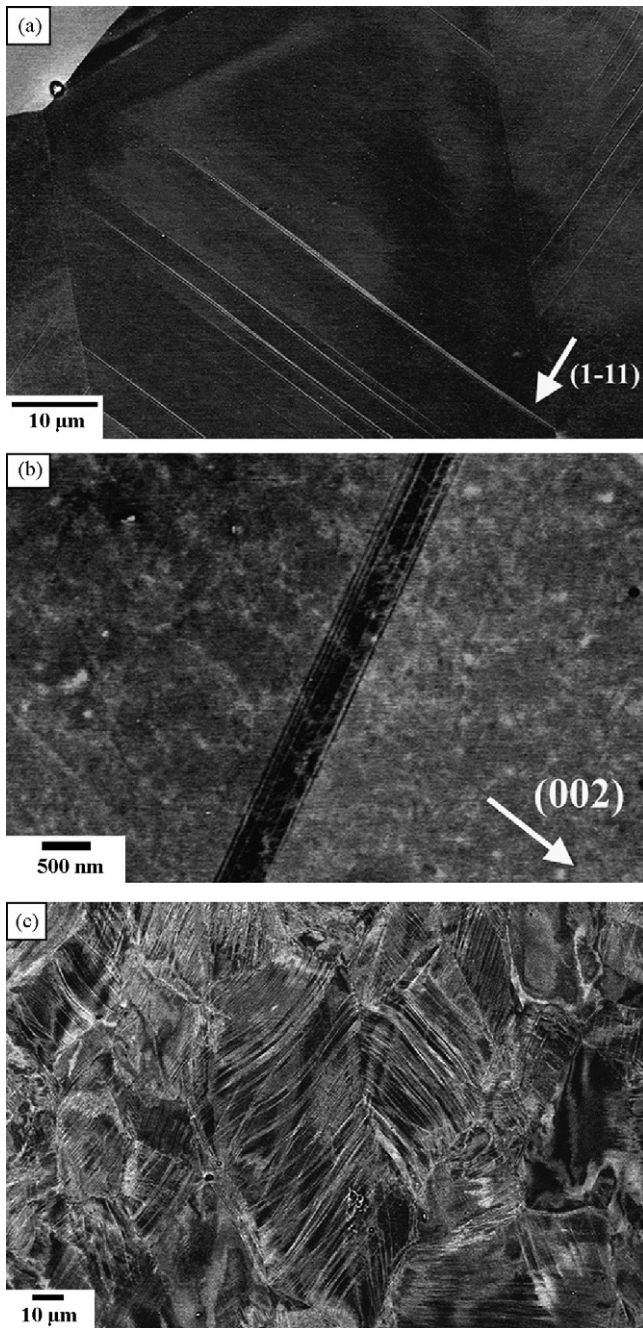


Fig. 1. Microstructures of steel LG (average grain size $50\ \mu\text{m}$) tensile deformed to 0.03 logarithmic strain (a and b) and 0.3 logarithmic strain (c). (a) ECCI image obtained in a SEM of grains containing bundles of deformation twins: diffraction vector $g: (1\ 1\ 1)_{\text{matrix}}$; (b) ECCI image of detail of a bundle containing thin twins (dark lines): diffraction vector $g: (0\ 0\ 2)_{\text{twin}}$.

Grains containing thin deformation twins (thickness 50–100 nm) are clearly observed, some of these twins are indicated with black arrows. Deformation twins were found even in grains smaller than $1\ \mu\text{m}$. Nevertheless, at this strain level the twin area fraction was very small, almost zero. At a higher logarithmic strain of 0.3 there was a significant increase in the twin area fraction, from zero to around 0.1. This increase in the twin area fraction is, however, smaller than in steel LG for the same strain level. Fig. 2(b) shows an ECCI image of the microstructure of steel FG strained to 0.3 logarithmic strain. The microstructure is very heterogeneous, like that observed for steel LG, containing grains with twins and grains with no twins. Most of the grains contained twins (around 80%) with

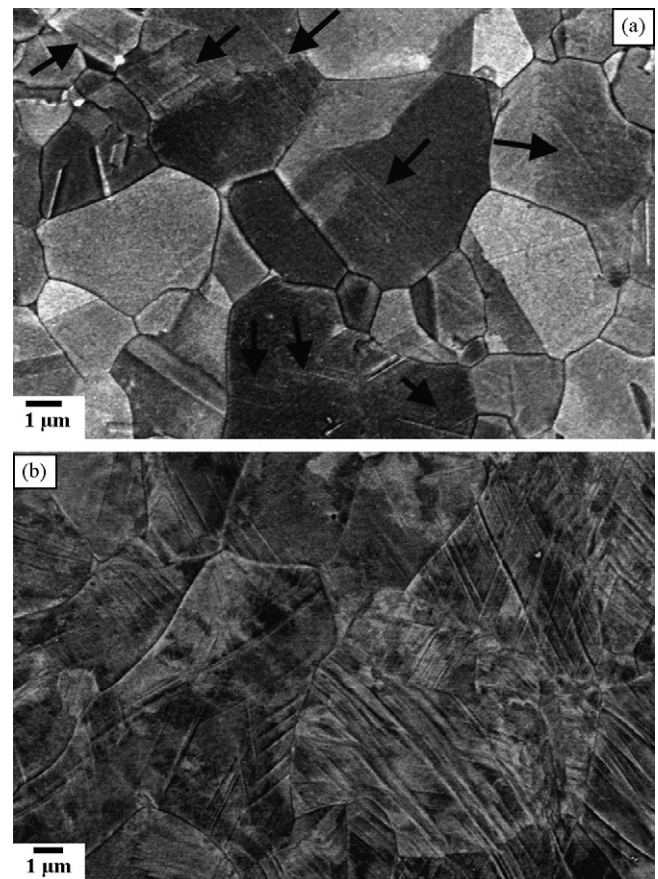


Fig. 2. ECCI images of microstructures containing deformation twins of steel FG (average grain size $3\ \mu\text{m}$), tensile deformed to 0.04 logarithmic strain (a) and 0.3 logarithmic strain (b). Black arrows indicate deformation twins.

different primary and secondary twinning systems activated.

3.2. Effect of grain orientation

We study the influence of grain orientation on deformation twinning during tensile deformation at room temperature on steel LG by means of EBSD. EBSD maps are displayed as image quality (IQ) maps and inverse pole figure (IPF) maps in the direction of tensile axis (TA). For better understanding of the influence of grain orientation on twinning, we analyze two deformation states: one at low strain (0.05 logarithmic strain) and another one at large strain (0.3 logarithmic strain).

Fig. 3(a) shows the inverse pole figure for the crystal direction along the tensile axis (TA-IPF) of the initial hot-rolled state indicating a weak texture of the starting state. Figs. 3(b) and (c) show TA-IPFs of the steel deformed to low and high strains, respectively. We observe that texture sharpens during tensile deformation, leading to texture components characterized by $\langle 111 \rangle // \text{TA}$ and $\langle 001 \rangle // \text{TA}$. Similar textures have been observed before in tensile deformed TWIP steels at room temperature [5,24]. Fig. 4 presents an example of an EBSD map performed on a sample strained to 0.05 logarithmic strain. As some twins are thinner than the resolution limit of the EBSD map, the TA-IPF map of Fig. 4(b) reveals a reduced number of indexed twins. However, in the image quality (IQ) map of Fig. 4(a) a higher number of twins is visible, appearing as straight thin dark lines. At this strain level, around one-third of the grains contained twins, mainly with only the primary twinning system activated. Fig. 5 shows a typical EBSD map performed on a sample strained to 0.3 logarithmic strain. At this strain level, bundles of twins were normally thicker than 100 nm and, therefore, most of

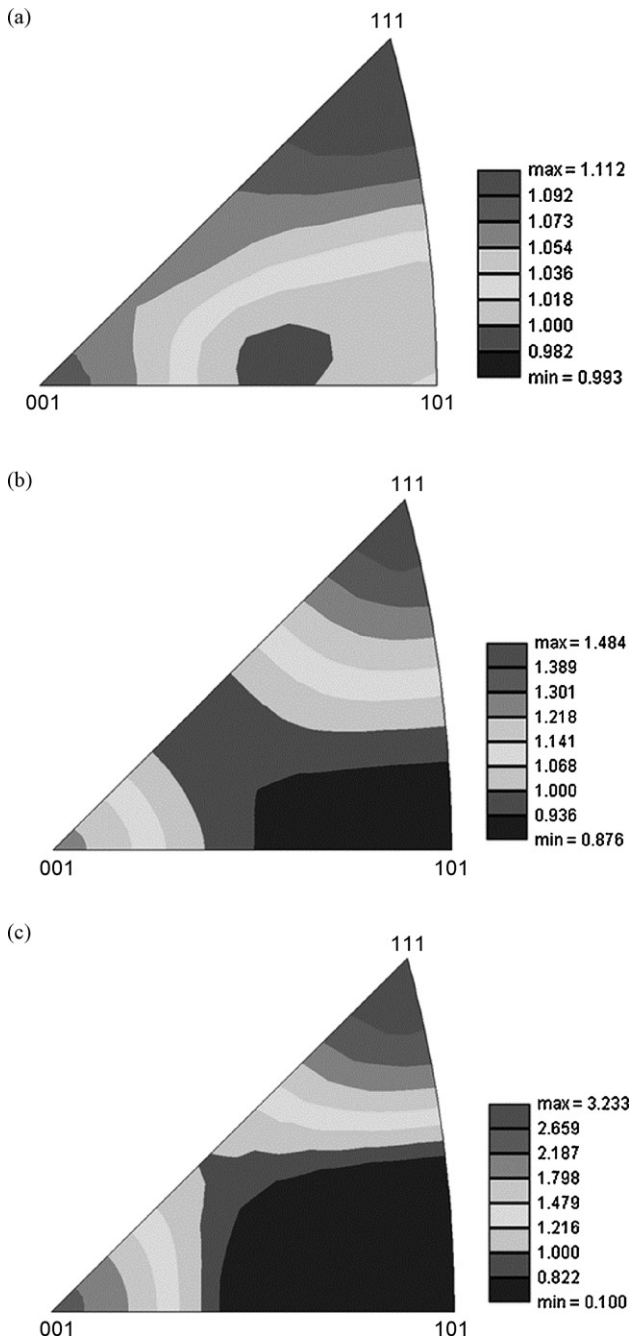


Fig. 3. Inverse pole figures along tensile axis direction of steel LG (average grain size $50\ \mu\text{m}$) at different states: as hot-rolled (a); tensile deformed to 0.03 logarithmic strain (b); tensile deformed to 0.3 logarithmic strain (c).

the twins can be indexed in the TA-IPF map. This figure shows that most of the grains, around 90%, contained deformation twins with several secondary activated twinning systems.

In order to study the influence of grain orientation on deformation twinning around 100 grains were analyzed in each deformation state. The orientation dependence of deformation twinning of steel LG to low strain and high strains is shown in Fig. 6(a) and (b), respectively. These TA-IPFs show orientations of grains containing twins (black dots) and of grains without twins (red dots). The TA-IPF of Fig. 6(a) shows that in the weakly strained LG sample there is a strong influence of the grain orientation on twinning activity. Deformation twinning mainly occurs in grains that are oriented close to the $\langle 111 \rangle // \text{TA}$ directions and only a small

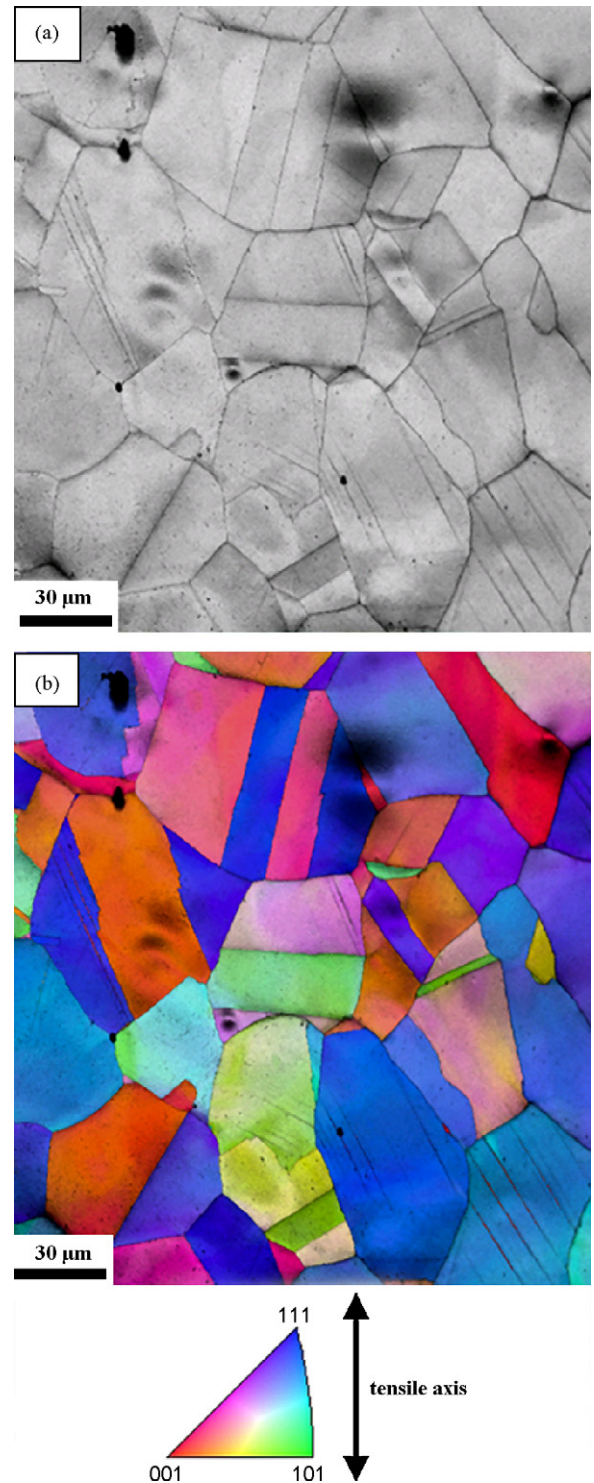


Fig. 4. EBSD map of steel LG (average grain size $50\ \mu\text{m}$) tensile deformed to 0.05 logarithmic strain. Diffraction pattern quality map (a), TA-IPF map (b) (TA: tensile axis; IPF: inverse pole figure).

fraction of grains with other orientations contain twins. Interestingly, at higher strain the influence of grain orientation on twinning activity decreased significantly. The TA-IPF given in Fig. 6(b) shows that in the highly strained LG sample, grains with almost all occurring orientations contained deformation twins and only grains oriented close to $\langle 001 \rangle // \text{TA}$ directions with angular deviation less than 5° contained no twins.

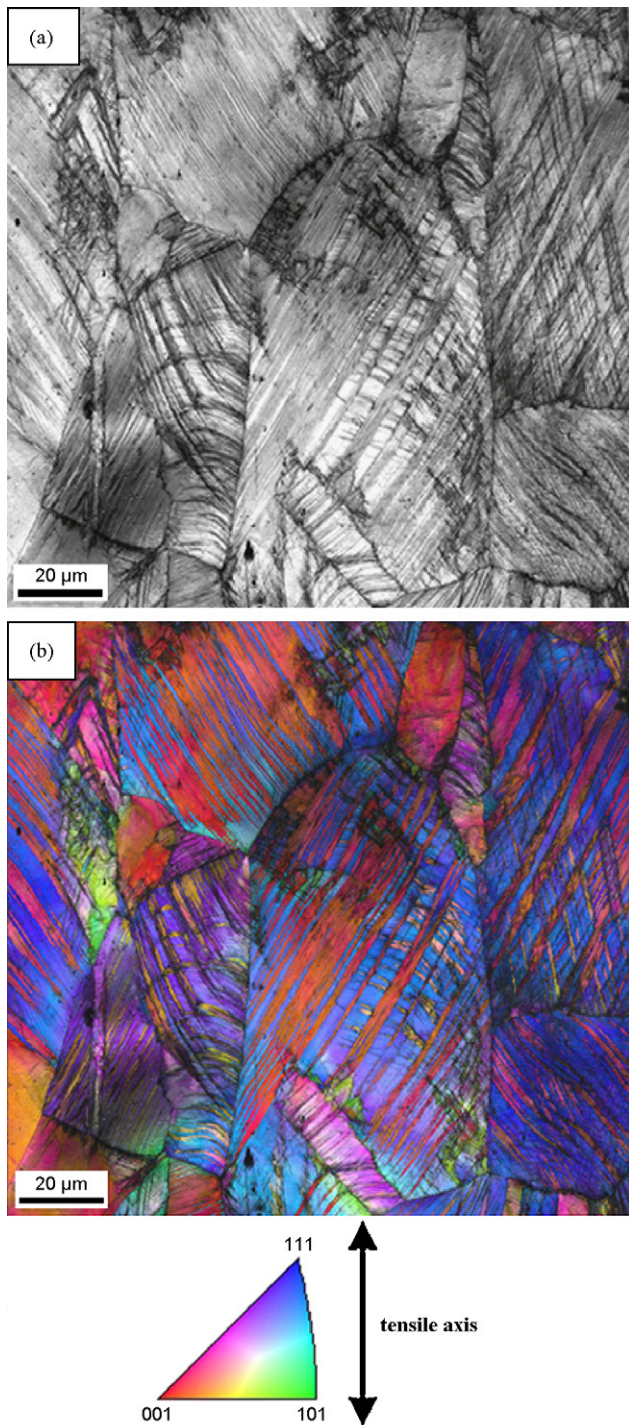


Fig. 5. EBSD map of steel LG (average grain size 50 μm) tensile deformed to 0.3 logarithmic strain. Diffraction pattern quality map (a), TA-IPF map (b) (TA: tensile axis; IPF: inverse pole figure).

4. Discussion

4.1. Effect of grain size

The main finding concerning the influence of grain size on deformation twinning is that grain refinement within the micrometer range does not suppress deformation twinning for the present TWIP steel tensile deformed at room temperature. Deformation twinning becomes more difficult as the average grain size decreases to 3 μm but it is not completely suppressed. Grain refinement pro-

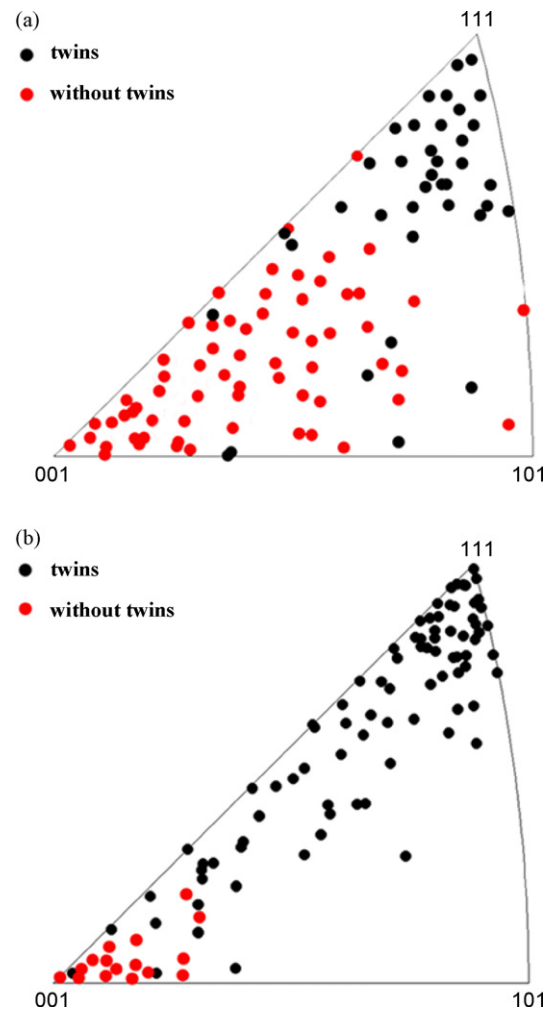


Fig. 6. Inverse pole figures along the tensile axis direction of steel LG (average grain size 50 μm) tensile strained to 0.05 logarithmic strain (a) and 0.3 logarithmic strain (b), respectively, showing grain orientations containing deformation twins (black dots) and without deformation twins (red dots). (For interpretation of the references to color in this figure legend, the reader is referred to the web version of the article.)

duces a strong decrease in the twin area fraction, from 0.2 for an average grain size of 50 μm to 0.1 for an average grain size of 3 μm at 0.3 logarithmic strain, but deformation twinning is still regularly observed in fine grains. As deformation twins are responsible for the outstanding mechanical properties of TWIP steels, this indicates that it is feasible to tailor the mechanical properties of Fe–22 wt.% Mn–0.6 wt.% C TWIP steels with grain refinement within the micrometer range. This is an interesting result regarding the optimization of the mechanical properties of TWIP steels. However, this result can at this stage not be generalized to other TWIP steel systems. For instance, Ueji et al. [5] reported a strong reduction in twinning activity in a Fe–31 wt.% Mn–3.0 wt.% Al–3.0 wt.% Si TWIP steel after similar grain refinement (average grain size of 1.8 μm) using also similar deformation conditions. The only difference is that the stacking fault energy (SFE) in Fe–31 wt.% Mn–3.0 wt.% Al–3.0 wt.% Si TWIP steel is larger than in the present Fe–22 wt.% Mn–0.6 wt.% C TWIP steel (around 40 mJ/m^2 against 22 mJ/m^2 [4,15]). These results indicate that the stacking fault energy, determined by chemical composition, plays a key role for the twinning behaviour in TWIP steels. Therefore, for a better understanding of twinning in TWIP steels both parameters, i.e. stacking fault energy and grain size, must be considered.

The influence of SFE on twinning is commonly considered as follows: Dislocation based models for deformation twinning in fcc

metals [10–13] propose that twinning is controlled by the glide of Shockley partials with Burgers vector $1/6 \langle 112 \rangle$ on $\{111\}$ planes. The critical resolved shear stress, τ_{critical} , to separate the leading Shockley partial from its trailing counterpart and thus create a twin is determined by a balance between the repulsive forces among the two Shockley partials and the attractive force of the SFE, given by

$$\tau_{\text{critical}} = \frac{\gamma}{b} \quad (1)$$

where γ is the SFE and b is the Burgers vector. As mentioned before, these models assume that twin nuclei already exist and therefore, only the stress for twin growth is estimated. Further, these models neither take into account the sources of dislocations nor a possible pile-up of dislocations in or at boundaries, thus the proposed twinning stress, τ_{critical} , can be considered as the twinning stress for a single crystal. The effect of grain size on deformation twinning still remains unclear. However, two approaches have been proposed to include the effect of grain size on twinning stress. In one approach [25] a Hall–Petch-type relation is proposed:

$$\tau_{\text{tw}} = \tau_0 + \frac{K_{\text{tw}}^{\text{H-P}}}{\sqrt{D}} \quad (2)$$

where τ_0 is the twinning stress for a single crystal, i.e. $\tau_0 = \tau_{\text{tw}} (D = \infty)$, and $K_{\text{tw}}^{\text{H-P}}$ is the Hall–Petch constant for twinning and D is the grain size. As explained above τ_0 can be replaced by γ/b leading to

$$\tau_{\text{tw}} = \frac{\gamma}{b} + \frac{K_{\text{tw}}^{\text{H-P}}}{\sqrt{D}} \quad (3)$$

This is a phenomenological relation which applies in many metals with different crystallographic structures such as hexagonal, bcc and fcc. Further, it has been reported that the Hall–Petch constant for twinning $K_{\text{tw}}^{\text{H-P}}$ is higher than that for slip $K_{\text{slip}}^{\text{H-P}}$ (for instance 10 times higher in Zr [26] and 2 times in copper [27]), although the reason for this difference is not well understood [25]. The other approach [28] proposes that the shear stress required to activate a twinning dislocation source is given by the shear stress to activate a Frank–Read source, $\tau_{\text{F-R}}$:

$$\tau_{\text{F-R}} = \frac{Gb}{2R} \quad (4)$$

where G is the shear modulus, b the Burgers vector and R the radius of the dislocation source. As twins are mainly nucleated at grain boundaries and the size of the softest possible dislocation source is proportional to the grain size, the following relation for the critical resolved shear stress for twinning is proposed:

$$\tau_{\text{tw}} = \frac{Gb}{D} \quad (5)$$

where G is the shear modulus, b is the Burgers vector and D is the grain size. This equation only describes the stress for nucleation of twins on boundaries. The growth of a twin in a homogeneous, single crystal matrix, however, is not considered. This growth stress is in principle the stress to drive the partial dislocations away from each other and may therefore be given by γ/b [10–13]. As a first approximation it should be independent of the grain size and can therefore be added to the nucleation stress, resulting in

$$\tau_{\text{tw}} = \frac{\gamma}{b} + \frac{Gb}{D} \quad (6)$$

In more detail, the grain size should have an effect, however, as grain size influences the yield stress which influences the hydrostatic pressure, which finally influences the stacking fault formation.

The examination of tensile strained samples by means of the ECCI technique reveals that deformation twinning occurs in both TWIP steels (steel LG and steel FG) at around 0.03 logarithmic strain.

This observation indicates that in the present TWIP steel deformation twinning initiates already at very low plastic strain, close to yielding. This result is consistent with previous observations by TEM in the same TWIP steel tensile deformed at room temperature where deformation twins were observed at 0.02 logarithmic strain [24]. Further studies on deformation twinning in fcc metals have also reported that deformation twinning is observed at small plastic strains [9,24,29]. However, the logarithmic stress at which deformation twinning was already activated (experimental twin stress) was higher in steel FG than in steel LG (steel FG: 400 MPa, steel LG: 270 MPa). This result indicates a clear effect of grain size on twin stress. However, this influence is not direct but indirect via slip, i.e. grain size mainly has an effect on slip. In fcc metals it has been observed that multiple slip is required for twinning, i.e. slip precedes twinning [9,12,29]. As explained above, in the present TWIP steel once multiple slip is activated deformation twinning occurs directly. These observations indicate a strong correlation between slip and twinning. As slip is influenced by the grain size via Hall–Petch a Hall–Petch-type dependence in twinning can therefore be expected. Table 1 shows the twinning stresses calculated from relations (3) and (6) for the present Fe–22 wt.% Mn–0.6 wt.% C TWIP steel. These stresses were calculated according to $\sigma_{\text{tw}} = \tau_{\text{tw}}/m$ assuming an average Schmid factor m of 0.326 [30], $\gamma = 22 \text{ mJ/m}^2$ [15], $b = 2.5 \times 10^{-10} \text{ m}$ [6], $G = 65 \text{ GPa}$ [6] and $K_{\text{tw}}^{\text{H-P}} = 356 \text{ MPa } \mu\text{m}^{1/2}$ [31]. As $K_{\text{tw}}^{\text{H-P}}$ is unknown $K_{\text{slip}}^{\text{H-P}}$ was used instead. Experimental twinning stresses are shown in the last column of Table 1. It can be seen that relation (3) overestimates the twinning stress but the grain size effect is properly reflected. Relation (6) estimates with high accuracy the twinning stress for an average grain size of $50 \mu\text{m}$ but provides a weak grain size dependence, which is not in agreement with experimental observations. These results suggest that in the micrometer range of the grain sizes studied in this work a Hall–Petch relation provides a good estimation of the influence of the grain size on the twinning stress.

It should be pointed out that the twinning stresses shown in Table 1 are calculated assuming $K_{\text{tw}}^{\text{H-P}} \sim K_{\text{slip}}^{\text{H-P}}$. Remarkably, this assumption provides reasonable twinning stresses suggesting that in the present TWIP steel $K_{\text{tw}}^{\text{H-P}} \leq K_{\text{slip}}^{\text{H-P}}$. This is a surprising result as there are very few studies reporting such behaviour [25]. Two significant conclusions can be obtained from this finding: (i) the effect of grain size on twinning stress is similar than on yield stress. Dislocation based models [10–13] propose that in fcc metals some specific dislocation reactions are needed to form a twin nucleus that subsequently evolves into a twin. It is also reported that in order to form such dislocation reactions multiple slip must be activated [9,12,29]. The experimental observation that deformation twinning occurs at small plastic strain close to yielding indicates that once multiple slip is activated deformation twinning occurs directly. $K_{\text{slip}}^{\text{H-P}}$ provides the resistance to slip propagation associated with the grain boundaries. The relation $K_{\text{tw}}^{\text{H-P}} \leq K_{\text{slip}}^{\text{H-P}}$ therefore indicates that the effect of grain size within the micrometer range on the twinning stress is mainly ascribed to the resistance to slip propagation associated to grain boundaries and, hence, to activate multiple slip inside the grains required to promote deformation twinning. (ii) For the present Fe–22 wt.% Mn–0.6 wt.% C TWIP steel, the effect of grain refinement within the micrometer range on the twinning stress and, hence, on twinning inhibition, is smaller than in other TWIP steels. This is supported by the experimental observation that in the present TWIP steel grain refinement within the micrometer range does not suppress twinning.

The relation (3) allows us to analyze separately the contribution of the stacking fault energy and grain size to the twinning stress. Fig. 7 shows the influence of both contributions, SFE and grain size, to the twinning stress of steel LG (average grain size of $50 \mu\text{m}$) and steel FG (average grain size of $3 \mu\text{m}$). It is seen that in both steels

Table 1

Estimated and experimental twinning stresses in a tensile deformed Fe–22 wt.% Mn–0.6 wt.% C TWIP steel with different average grain sizes.

Average grain size (μm)	$\sigma_{\text{tw}} = (1/m)(\gamma/b) + (K_{\text{tw}}^{\text{H-P}}/\sqrt{D})$ (MPa)	$\sigma_{\text{tw}} = (1/m)(\gamma/b) + (Gb/D)$ (MPa)	Experimental σ_{tw} (MPa)
50	323	274	270
3	478	290	400

the contribution of SFE to the twinning stress is larger than that of the grain size. For large grain sizes (above $50 \mu\text{m}$) the contribution of grain size to the twinning stress is small (50 MPa, less than 15% of the twinning stress), increasing its importance with grain size refinement. For an average grain size of $3 \mu\text{m}$ (steel FG) the contribution of grain size to twinning stress is similar to that of the SFE.

4.2. Effect of grain orientation

The main result concerning the influence of grain orientation on twinning behavior in the present TWIP steel tensile deformed at room temperature is that the grain orientation has a strong influence on deformation twinning at low strains but at high strains the influence decreases significantly.

The influence of grain orientation on deformation twinning is commonly explained in terms of Schmid's law for slip twin dislocations [7,15–17,29]:

$$\tau_{\text{tw}} = \sigma \cos \phi \cos \lambda \quad (7)$$

where $m = \cos \phi \cos \lambda$ is the Schmid factor, σ is the macroscopic stress in MPa, ϕ is the angle between the twinning plane normal and the tensile axis, and λ is the angle between the twinning shear direction and the tensile axis. We assume that Schmid's law is valid in the present study as in previous studies on similar TWIP steels [15], with the difference, of course, that twinning is unidirectional only. It is further assumed that the critical resolved shear stresses for both slip and twinning are approximately equal. This is supported by the strong correlation observed between slip and twinning in fcc metals, i.e. multiple slip is seen to be required for twinning to occur [9,12,29], and the results obtained in the present work showing that once multiple slip is activated twinning occurs readily resulting in similar stresses for both slip and twinning. However, this assumption does not imply that twinning can occur before slip because it is a necessary but not sufficient condition. Therefore, once multiple slip is activated, twinning occurs when the twinning stress τ_{tw} is larger than the slip stress τ_s , i.e. for those grains where the highest Schmid factor for twinning m_{tw} is larger than the highest Schmid factor for slip m_s , this is

$$m_{\text{tw}} > m_s \quad (8)$$

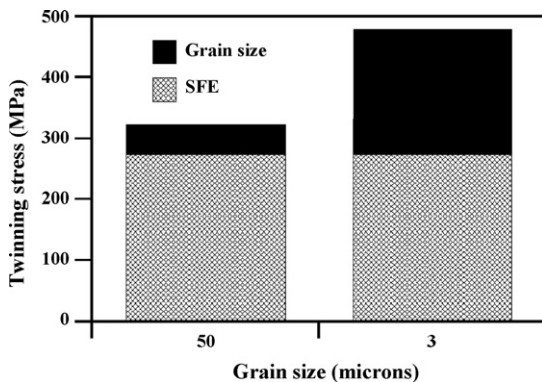


Fig. 7. Graph of the contribution of the stacking fault term (γ/b) and grain size term ($K_{\text{tw}}^{\text{H-P}}/\sqrt{D}$) on the twinning stress for steel LG (average grain $50 \mu\text{m}$) and steel FG (average grain size $3 \mu\text{m}$).

Assuming this twinning criterion, the grain orientations favorable and unfavorable for twinning can be calculated for a particular macroscopic stress. Fig. 8(a) shows the TA-IPF with calculated grain orientations favorable (red lines) and unfavorable for twinning (blue lines) during tensile deformation. The figure reveals two regions of grain orientations where twinning is favorable or not. The predicted regions are in excellent agreement with the observed grain orientations in steel LG tensile deformed to 0.05 logarithmic strain, Fig. 8(b). Almost all observed orientations fall within the corresponding Schmid regime of the TA-IPF. This result indicates first that our assumption that the critical resolved shear stresses for slip and twinning are very similar is correct. Second, Schmid's law fully explains the strong influence of grain orientation on deformation twinning observed in steel LG tensile deformed to low strain. At this strain level deformation twinning mainly occurs in grains oriented close to the $(111)/\text{TA}$ directions. Nevertheless, the Schmid law does not explain the small influence of the grain orientation on deformation twinning observed at higher

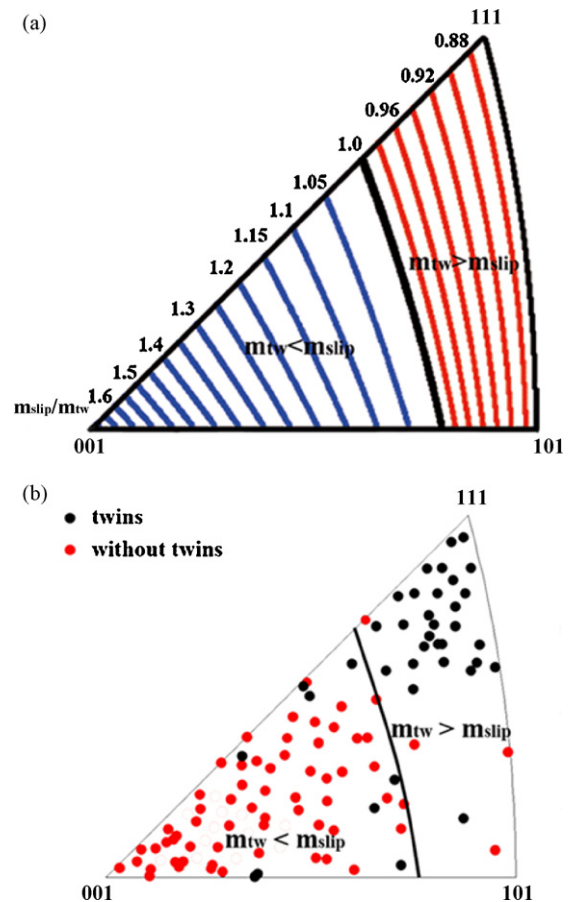


Fig. 8. (a) Inverse pole figure along tensile axis direction showing the grain orientations which are favorably (area with red lines) and unfavorably oriented (area with blue lines) for twinning according to the Schmid law and the assumption of equal critical resolved shear stresses for slip and twinning. (b) Comparison between experimental grain orientations (dots) obtained in steel LG (average grain size $50 \mu\text{m}$) tensile strained to 0.05 logarithmic strain and calculated orientation regions from the Schmid law. (For interpretation of the references to color in this figure legend, the reader is referred to the web version of the article.)

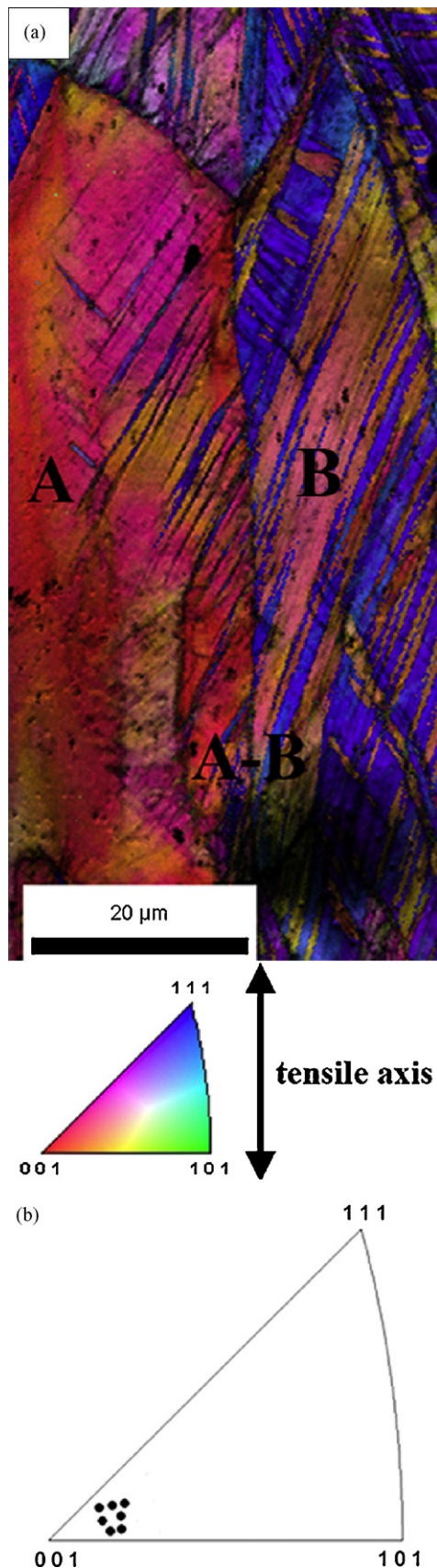


Fig. 9. (a) TA-IPF map of the steel LG (average grain size 50 μm) tensile deformed to 0.3 logarithmic strain showing a grain (grain A) that is unfavorably oriented for twinning with respect to the macroscopic stress which contains deformation twins; (b) TA-IPF of grain A (TA: tensile axis; IPF: inverse pole figure).

strain, as the TA-IPF in Fig. 6(b) shows. At 0.3 logarithmic strain, deformation twinning occurs regularly in grains oriented unfavorably for twinning according to Schmid's law taking into account the current grain orientation. Only grains oriented close to the $\langle 001 \rangle // TA$ directions are free of twins. The deviation from Schmid's law observed at high strain is not unexpected although surprisingly, it has not been reported in previous studies on TWIP steels [16,17]. This deviation can be explained as follows. The predicted orientations from Schmid's law, shown in the TA-IPF of Fig. 8(a), were calculated assuming the macroscopical unidirectional stress state to act in a similar manner everywhere in the material. In the present TWIP steel tensile deformed to high strain, the local stress state controlling deformation twinning may, however, be very different from the macroscopic one [21,32–34]. Figs. 1 and 2 reveal that the present TWIP steel develops during tensile deformation a complex and heterogeneous microstructure with a high amount of deformation twins. Deformation twins formed in one grain may create local shear stress concentrations at loci where they impinge on a grain boundary. This may lead to nucleation of twins in neighbouring grains even if they are – with respect to the macroscopic stress state – unfavorably oriented for twinning. The TA-IPF map in Fig. 9(a) shows an example of a grain unfavorably oriented for twinning with respect to the macroscopic stress which contains deformation twins (grain orientation spread is shown in the TA-IPF of Fig. 9(b)). The grain oriented close to the $\langle 001 \rangle // TA$ direction, referred to as grain A, is highly unfavorably oriented for twinning. Nevertheless, it contains a large amount of deformation twins which have, however, not grown all the way through the grain. These twins are nucleated at the grain boundary A-B where bundles of twins of the adjacent grain (grain B) impinged. A more detailed analysis on the twinning transfer across the grain boundaries would require consideration of the grain boundary character [22,34]. This has, however, not been done here.

5. Conclusions

We investigate the influence of grain size and grain orientation on deformation twinning in a tensile deformed Fe–22 wt.% Mn–0.6 wt.% C TWIP steel at room temperature. The following conclusions are drawn:

- Grain refinement within the micrometer range does not suppress deformation twinning. As deformation twins are responsible for the outstanding mechanical properties of TWIP steels, this indicates that it is feasible to tailor the mechanical properties of Fe–22 wt.% Mn–0.6 wt.% C TWIP steels with grain refinement within the micrometer range. As twinning stress is strongly dependent on the stacking fault energy, this result can not be extended to other TWIP steels as minor modifications in chemical composition may alter the stacking fault energy.
- A Hall–Petch relation $\sigma_{tw} = (\gamma/mb) + (K_{tw}^{H-P}/\sqrt{D})$ provides a good estimate of the effect of grain size within the micrometer range on the twinning stress. It was found that the Hall–Petch constant for twinning, K_{tw}^{H-P} , is about equal to that for slip, K_{slip}^{H-P} . Two significant conclusions can be drawn from this finding: (i) the effect of the grain size on twinning stress is similar to its effect on yield stress. This is ascribed to the resistance to slip propagation associated to grain boundaries. Slip propagation is associated to activation of multiple slip which is a prerequisite to deformation twin nucleation. (ii) For the present TWIP steel, the effect of grain refinement within the micrometer range on the twinning stress and, hence, on twinning inhibition, is smaller than in other TWIP steels.
- The orientation dependence of twinning at small strain shows that the critical resolved shear stress for twinning and slip are very similar as the appearance of twinning fully complies with

the Schmid law under these conditions. Deformation twinning mainly occurs in grains oriented close to $\langle 111 \rangle$ //tensile axis where the maximum resolved shear for twinning, τ_{tw} , is larger than that for slip, τ_s .

- At high strains (above 0.3 logarithmic strain), a strong deviation from the macroscopic Schmid law is observed. Deformation twins are observed in grains that are unfavourably oriented with respect to twinning according to Schmid's law. Local stress concentrations due to the accumulation of shear stresses at grain boundaries coming from incoming bundles of deformation twins, and also probably the grain boundary character, play an important role on the twinning behavior. This may lead to nucleation of twins in neighbouring grains even if they are – with respect to the macroscopic stress state – unfavourably oriented for twinning.

Acknowledgments

The authors would like to acknowledge the financial support by the German Research Foundation within the framework of the SFB 761 “steel ab initio”. The authors also acknowledge the help from Luc Hantcherli in the preparation of Fig. 8(a).

References

- [1] O. Grässel, L. Krüger, G. Frommeyer, L.W. Meyer, *Int. J. Plast.* 16 (2000) 1391–1409.
- [2] G. Frommeyer, U. Brück, P. Neumann, *ISIJ Int.* 43 (2003) 438–446.
- [3] S. Allain, J.P. Chateau, O. Bouaziz, *Mater. Sci. Eng. A* 387–389 (2004) 143–147.
- [4] S. Vercammen, B. Blanpain, B.C. De Cooman, P. Wollants, *Acta Mater.* 52 (2004) 2005–2012.
- [5] R. Ueji, N. Tsuchida, D. Terada, N. Tsuji, Y. Tanaka, A. Takemura, K. Kunishige, *Scr. Mater.* 59 (2008) 963–966.
- [6] O. Bouaziz, S. Allain, C. Scott, *Scr. Mater.* 58 (2008) 484–487.
- [7] M.N. Shiekhelsouk, V. Favier, K. Inal, M. Cherkaoui, *Int. J. Plast.* 25 (2009) 105–133.
- [8] T. Shun, C.M. Wan, J.G. Byrne, *Acta Metall. Mater.* 40 (1992) 3407–3412.
- [9] J.W. Christian, S. Mahajan, *Prog. Mater. Sci.* 39 (1995) 1–157.
- [10] J.A. Venables, *Phil. Mag.* 6 (1961) 379–396.
- [11] H. Fujita, T. Mori, *Scr. Metall.* 9 (1975) 631–636.
- [12] S. Mahajan, G.Y. Chin, *Acta Metall.* 21 (1973) 1353–1363.
- [13] N. Narita, J. Takamura, *Phil. Mag.* 29 (1974) 1001–1028.
- [14] T.H. Lee, C.S. Oh, S.J. Kim, S. Takaki, *Acta Mater.* 55 (2007) 3649–3662.
- [15] L. Bracke, L. Kestens, J. Penning, *Scr. Mater.* 61 (2009) 220–222.
- [16] P. Yang, Q. Xie, L. Meng, H. Ding, Z. Tang, *Scr. Mater.* 55 (2006) 629–631.
- [17] L. Meng, P. Yang, Q. Xie, H. Ding, Z. Tang, *Scr. Mater.* 56 (2007) 931–934.
- [18] D. Senk, H. Emmerich, J. Rezendes, R. Siquieri, *Adv. Eng. Mater.* 9 (2007) 695–702.
- [19] C. Sachs, H. Fabritius, D. Raabe, *J. Struct. Biol.* 155 (2006) 409–425.
- [20] D. Raabe, M. Sachtleber, Z. Zhao, F. Roters, S. Zaefferer, *Acta Mater.* 49 (2001) 3433–3441.
- [21] D. Raabe, M. Sachtleber, H. Weiland, G. Scheele, Z. Zhao, *Acta Mater.* 51 (2003) 1539–1560.
- [22] S. Zaefferer, J.C. Kuo, Z. Zhao, M. Winning, D. Raabe, *Acta Mater.* 51 (2003) 4719–4735.
- [23] I. Gutierrez-Urrutia, S. Zaefferer, D. Raabe, *Scr. Mater.* 61 (2009) 737–740.
- [24] D. Barbier, N. Gey, S. Allain, N. Bozzolo, M. Humbert, *Mater. Sci. Eng. A* 500 (2009) 196–206.
- [25] M.A. Meyers, O. Vöhringer, V.A. Lubarda, *Acta Mater.* 49 (2001) 4025–4039.
- [26] S.G. Song, G.T. Gray III, *Metall. Mater. Trans.* 26A (1995) 2665–2675.
- [27] O. Vöhringer, *Z. Metallkd.* 67 (1976) 51.
- [28] W.Z. Han, Z.F. Zhang, S.D. Wu, S.X. Li, *Phil. Mag.* 88 (2008) 3011–3029.
- [29] I. Karaman, H. Sehitoglu, K. Gall, Y.I. Chumlyakov, H.J. Maier, *Acta Mater.* 48 (2000) 1345–1359.
- [30] G.I. Taylor, *J. Inst. Met.* 62 (1938) 307–324.
- [31] F. de las Cuevas, M. Reis, A. Ferraiuolo, G. Prato Longo, L.P. Karjalainen, J. Alkorta, J. Gil Sevillano, *Key Eng. Mater.* 423 (2010) 147–152.
- [32] Z. Zhao, M. Ramesh, D. Raabe, A. Cuitino, R. Radovitzky, *Int. J. Plast.* 24 (2008) 2278–2297.
- [33] M. Sachtleber, Z. Zhao, D. Raabe, *Mater. Sci. Eng. A* 336 (2002) 81–87.
- [34] T.R. Bieler, P. Eisenlohr, F. Roters, D. Kumar, D.E. Mason, M.A. Crimp, D. Raabe, *Int. J. Plast.* 25 (2009) 1655–1683.